

Development of a Semi-Autonomous Directional and Spectroscopic Radiation Detection Mobile Platform

By

Alexander Luke Miller

A Thesis Submitted in Partial Fulfillment
of the Requirements for the Degree of Masters of Applied Science
in
Nuclear Engineering

Faculty of Energy Systems and Nuclear Science
University of Ontario Institute of Technology

Oshawa, Ontario, Canada

© Alex Miller, March 2014

Abstract

This thesis presents a method for a small, inexpensive mobile robot equipped with a single high resolution scintillation detector to quickly survey an area and convey information about local sources of gamma radiation to a remote human operator. This is achieved by surrounding the detector with a lead sheath that blocks all gamma rays except those incident along the detector's axial direction. A horizontal scan is performed by rotating the detector and a directional profile of gamma radiation is constructed. In addition a visual panorama of the local area is assembled using a camera mounted on the detector. A plot of the detector signal versus angle is then overlaid on top of the visual panorama and visible peaks clearly indicate the direction of local gamma radiation sources. Moreover, measuring the energy spectrum of gamma rays in each direction produces a 2D count frequency histogram where distinct peaks indicate the energy and direction of local gamma ray sources allowing the identification of different radio-isotopes.

Acknowledgements

I would like to thank my supervisors, Dr. Rachid Machrafi and Dr. Atef Mohany, for noticing my potential as a scientist and guiding me through my work. Dr. Mohany has been an important influence throughout the development of my thesis and his contribution from the beginning to the end was always invaluable. Dr. Machrafi's constant encouragement, wisdom and praise have been an important motivation for my success.

I must thank my parents for raising me properly and lovingly supporting me throughout my life. I would not be writing this thesis without excellent parenting as a pre-requisite. I owe thanks to everyone in my whole family, immediate and extended. Nick deserves special attention since he saw all of my work from day one and was always there for me with a helping hand. Thanks for my special Sarah for being there for me day to day when I was engulfed in my work. I really appreciate the support and love I received from all.

Dedication

I dedicate this thesis to my brothers, Nick and Jeff whose positive influence on my life has been immeasurable.

Thesis Contribution to the Field

We have made two notable contributions to the field of automated gamma ray detection systems.

First, we developed an inexpensive method of identifying the direction and energy spectra of local gamma ray sources from a single survey point using a 2D count frequency histogram.

Second, we have also developed an effective method for displaying the directional information of local gamma ray sources in a wide angle panoramic field of view that is easily interpreted by a human observer.

Table of Contents

Abstract.....	2
Acknowledgements	3
List of Figures	8
List of Tables	10
Nomenclature	11
Introduction	13
Chapter 1: Theoretical Background	16
1.1 Radiation Sources	16
1.2 Gamma Ray Interaction with Matter.....	18
1.3 Gamma Ray Energy Spectra	21
1.4 Gamma Ray Detectors.....	22
1.4.1 Overview of Gamma Ray Detectors	22
1.4.2 Scintillation Detectors.....	23
1.5 Lanthanum Bromide Scintillation Detector	27
1.6 Directional Sensitivity of Cylindrical Scintillation Detectors.....	29
1.7 Point Source Triangulation	33
Chapter 2: Methodology	37
Methodology Overview	37
2.1 Directional Gamma Ray Measurement Method.....	38
2.2 Description of the Prototype Design	40
2.3 Gamma Ray Detection System.....	46
2.3.1 LaBr ₃ Scintillator Detector.....	46
2.3.2 Digital Gamma Ray Measurement: Count Rate Measurements.....	47
2.3.3 Energy Spectra Measurements	47
2.4 Sweep Scan Measurements: Count Rate Mode.....	48
2.5 Radiation Data Visual Overlay	49
2.6 Sweep Scan Measurements with MCA for Energy Spectra.....	50
2.6.1 Directional Profiles with Energy Spectra	50
2.6.2 Rapid Scan Directional Profiles with Energy Spectra.....	50
2.7 Autonomous Source Seek Mode Operation	51
2.8 Experimental Setup	56
2.8.1 Equipment and Gamma Ray Sources.....	56

2.8.2 Directional Profile and Visual Panorama – Sweep Scan Mode with Count Rate	58
2.8.3 Directional profile and Visual Panorama – Sweep Scan Mode with Energy Spectra.....	63
2.8.4 Rapid Scan Directional Profile and Visual Panorama with Energy Spectra.....	65
2.8.5 Point Source Triangulation Experiments	67
2.8.6 Autonomous Source Seek Mode.....	70
Chapter 3: Experimental Results and Discussion.....	74
3.1 Directional Profile and Visual Panorama Results: Sweep Scan Mode with Count Rate.....	74
3.1.1 Gamma Ray Directional Profile Results.....	74
3.1.2 Visual Overlay Results	76
3.1.3 Point Source Directional Localization Results	78
3.1.4 Multiple Point Source Results	80
3.1.5 Directional Profile Results with Natural Distributed Mixed Alpha, Beta and Gamma Source .	82
3.2 Directional Profile and Visual Panorama Results: Sweep Scan Mode with Energy Spectra.....	84
3.3 Rapid Scan Directional Profile Results with Energy Spectra	90
3.3.1 Rapid Scan Directional Profile Results with ¹³³ Ba	90
3.3.2 Rapid Scan Directional Profile Results with ⁶⁰ Co	94
3.4 Point Source Triangulation	97
3.5 Autonomous Source Seek Mode Results.....	102
3.5.1 Source Seek Mode Results.....	102
3.5.2 Source Seek Mode Results with Hidden Source	105
3.6 Discussion of Uncertainty and Measurement Error.....	108
3.6.1 Uncertainty in Sweep Scan Mode with Count Rate Measurements.....	108
3.6.2 Uncertainty in Sweep Scan Mode with Energy Spectra.....	112
3.6.3 Uncertainty in Point Source Triangulation	114
Conclusion.....	116
Future Work.....	117
References	118
Appendix A: Properties of LaBr ₃	121
Appendix B: Background Radiation.....	123
Appendix C: Supplementary Data.....	124

List of Figures

Figure 1: Characteristic gamma rays emitted from ^{60}Co and ^{137}Cs [18]	22
Figure 2: Schematic of a scintillation spectrometer.....	24
Figure 3: Schematic of a detector and source [18]	26
Figure 4: 60,000 second background spectra with LaBr_3 detector [1].....	28
Figure 5: Three dimensional configuration of detector and point gamma source model [23]	30
Figure 6: Schematic of point source arc around detector in MATLAB program.	32
Figure 7: Directional sensitivity of cylindrical LaBr_3 detector.....	33
Figure 8: Linear equations determined by robot at four known measurement positions	35
Figure 9: Directional sensitivity of LaBr_3 detector with lead collimator.	40
Figure 10: Four wheeled chassis (left) and Saber-tooth differential drive motor controller (right)	41
Figure 11: Prototype mobile robot	42
Figure 12: Bot Board 2 (left) and 28 pin Basic Atom Pro microcontroller (right)	43
Figure 13: Schematic of robot's control system [26].....	44
Figure 14: Robot's wireless control pad	46
Figure 15: Schematic of robot's 180° sweep scan mode.	49
Figure 16: Schematic of robot's rapid sweep scan mode	51
Figure 17: Rotational stage in source seek mode.....	53
Figure 18: Nine direction sweep scan in source seek mode	54
Figure 19: Forward direction 90° fine sweep in source seek mode.....	54
Figure 20: Final localization of source in source seek mode.....	55
Figure 21: Diagram of sweep scan measurements with a ^{137}Cs source at 90°	59
Figure 22: Photo of sweep scan experiment setup with a $1\text{mCi } ^{137}\text{Cs}$ source at 90°	60
Figure 23: Diagram of sweep scan measurements with two sources of $1\text{mCi } ^{137}\text{Cs}$ at 60° and 120°	61
Figure 24: Diagram of sweep scan measurements with natural rock source.....	62
Figure 25: Experimental setup of natural rock source measurement.....	62
Figure 26: Experimental setup of directional profile with energy spectra measurement with	64
Figure 27: Photo of the Experiment with $28.7\ \mu\text{Ci } ^{137}\text{Cs}$ and $2.2\ \mu\text{Ci } ^{60}\text{Co}$ sources	65
Figure 28: Schematic of a rapid scan experiment	66
Figure 29: Photo of $500\ \mu\text{Ci } ^{133}\text{Ba}$ source used in rapid scan experiment	67
Figure 30: Setup of source position triangulation experiment	69
Figure 31: View of box and internal view of box revealing internal gamma source.....	69
Figure 32: Setup of source seek mode experiment.....	71
Figure 33: Setup of source seek mode experiment with hidden sources.....	72
Figure 34: Source seek mode experiment with hidden sources	73
Figure 35: Source seek mode experiment location of hidden sources	73
Figure 36: Directional profile results for a $1\text{mCi } ^{137}\text{Cs}$ point source at 0° , 30° , 60° and 90°	75
Figure 37: Panorama and directional profile overlay for source at 90°	76
Figure 38: Panorama and directional profile overlay for source at 60°	77
Figure 39: Panorama and directional profile overlay for source at 30°	77
Figure 40: Panorama and directional profile overlay for source at 0°	78
Figure 41: Source locations indicated by mobile robot	79

Figure 42: Directional profile results for two ^{137}Cs sources at 60° and 120°	80
Figure 43: Panorama and directional profile overlay for two sources at 60° and 120°	81
Figure 44: Multiple source locations indicated by mobile robot	81
Figure 45: Directional profile results for natural rock source	82
Figure 46: Panorama and directional profile overlay for natural rock source	83
Figure 47: Natural rock source target location indicated by the mobile robot	84
Figure 48: Gamma Ray Energy Calibration Spectra	85
Figure 49: Raw frequency data for spectra and directional profile	86
Figure 50: Smoothed spectra and directional profile	87
Figure 51: Total energy spectra profile	88
Figure 52: Panorama and directional profile overlay for ^{137}Cs (red) and ^{60}Co (yellow)	89
Figure 53: Location of ^{137}Cs at 90° and ^{60}Co at 48° as indicated directional profile peaks	90
Figure 54: Rapid spectra scan with ^{133}Ba Source	91
Figure 55: Smoothed spectra and directional profile for forward direction sweep of ^{133}Ba	92
Figure 56: Panorama and smoothed directional profile for 356 KeV Channel from ^{133}Ba source	93
Figure 57: Location of the ^{133}Ba source as indicated by mobile robot	94
Figure 58: Rapid spectra scan for ^{60}Co Source	95
Figure 59: Smoothed spectra and directional profile for forward direction sweep of ^{60}Co	96
Figure 60: Smoothed gamma ray directional profile for ^{60}Co rapid scan	97
Figure 61: Source direction indicated by the mobile robot from four known locations	98
Figure 62: Top-down view of triangulation experiment	100
Figure 63: Triangulation experimental results	100
Figure 64: Map of point source triangulation experiment.	102
Figure 65: Source Seek Mode Data	103
Figure 66: Video sequence of first phase in source seek mode with a 1mCi ^{137}Cs source	104
Figure 67: Video sequence of source seek mode with a 1mCi ^{137}Cs source	105
Figure 68: Video sequence of source seek mode with a hidden mixed gamma source	106
Figure 69: Hidden source located by source seek mode	107
Figure 70: Shifted gamma ray directional profiles	109
Figure 71: Gamma ray directional profile peaks with best fit Gaussian functions.	111
Figure 72: ^{137}Cs gamma ray directional profile raw data and smoothed data	113

Appendix Figures

Figure A1: Comparison Spectra for NaI, LaBr ₃ and HPGE [30]	121
Figure A2: Resolution comparison for NaI and LaBr [1]	122
Figure A3: Background Radiation Spectrum for NaI in massive lead shield [18]	123
Figure A4: Gamma ray directional profile results with 1 mCi ^{137}Cs at 0° , 30° , 60° , and 90°	125
Figure A5: Raw frequency data for ^{133}Ba rapid scan gamma ray profile	126
Figure A6: Raw frequency data ^{60}Co rapid scan gamma ray profile	127

List of Tables

Table 1: Source Directions determined from 4 known robot positions	98
Table 2: Comparison of NaI, LaBr ₃ and HPGE.....	121
Table 3: Radiation Source Activities	124

Nomenclature

I : Gamma ray beam intensity

I_0 : Initial gamma ray beam intensity

P : Probability of interaction

dP : Instantaneous probability of interaction

x : Distance traveled through a material

dx : Infinitesimal distance traveled through a material

H_0 : Mean energy of a peak in a gamma spectrum

μ_{total} : Total linear attenuation coefficient

μ_{PE} : Photo-Electric linear attenuation coefficient

μ_{C} : Compton scattering linear attenuation coefficient

μ_{PP} : Pair production linear attenuation coefficient

μ_{lead} : Total linear attenuation coefficient of lead

μ_{detector} : Total linear attenuation coefficient of detector material

x_{detector} : Distance traveled through detector

x_{lead} : Distance traveled through lead

ϵ_{SA} : Solid Angle efficiency

ϵ_i : Intrinsic efficiency

ϵ_T : Total Counting efficiency

θ : Horizontal angle

φ : Azimuthal angle

$(x, y)_{\text{source}}$: Gamma ray source position

$(x, y)_{\text{robot}}$: Robot position

$\theta_{s1,2,\dots}$: Angle of source relative to robot

$m_{1,2,\dots}$: Slope of line determined from robot position 1,2,...

$b_{1,2,\dots}$: y-intercept of line determined from robot position 1,2,...

A: Slope matrix for source triangulation

\bar{b} : y-intercept matrix for source triangulation

\bar{v} : Variable matrix for gamma ray source position $(x, y)_{\text{source}}$

$\Delta\theta$: Uncertainty in angle measurement

Δm : Uncertainty in slope measurement

Δb : Uncertainty in y-intercept measurement

Δx : Uncertainty in x position

Δy : Uncertainty in y position

Abbreviations

FWHM: Full width at half maximum

GIMP: GNU image manipulation program

GPIO: General Purpose Input/output

LET : Lineal Energy Transfer

TCE: Total counting efficiency

PMT: Photomultiplier tube

PE : Photo-Electric Effect

C : Compton Scattering

PP : Pair Production

MCA: Multi Channel Analyzer

DAQ: Data Acquisition System

ADC: Analog-to-digital Convertor

SLAM: simultaneous localizing and mapping

UOIT: University of Ontario Institute of Technology

USB: Universal Serial Bus

Introduction

Identifying and locating sources of radiation is critically important in high risk environments such as nuclear power plants, medical facilities, areas contaminated by nuclear accidents and routes for the transportation of radioactive material. Detecting, identifying, and localizing sources of radiation is also essential in non-proliferation operations and in searching for illicitly smuggled nuclear materials [1]. Robots can be used to remotely locate and map radioactive sources without the need to put people at risk by exposing them to potentially high levels of radiation. In addition, robots may be capable of accessing areas that are otherwise hazardous or completely inaccessible to humans.

High doses of radiation are well known to be hazardous to human health. Unfortunately, harmful forms of radiation are completely imperceptible and cannot be seen or felt by someone who may be exposed. It cannot be detected by traditional sensory equipment such as video cameras or microphones. Thus, a large variety of radiation detectors have been developed and are widely used throughout the nuclear industry. Furthermore, robots can be used to enter areas contaminated by radiation and avoid unnecessary human exposure. The radiation detectors typically used on such robots are capable of detecting alpha, beta, neutron, x-ray or gamma radiation and may be capable of identifying the type of radiation present and measuring dose quantities such as dose rates. However, it is not common for robots to be capable of detecting the direction of incoming radiation and locating local sources of radiation from a single survey point. Gamma ray cameras are capable of accomplishing this for the case of gamma radiation [2][3]. Gamma ray cameras have been effective for imaging radioactive gamma sources and

overlaying data on a visual image in order to display the local gamma ray field in a way that is easily interpreted by a human observer [2][4][5]. However, most gamma ray cameras are exceedingly expensive and typically too large to fit on small mobile robots [6].

There are many mobile robots designed for the purposes of radiation detection and radioactive source localization. One common application of such robots is mapping radiation levels in unknown areas. This is usually accomplished by integrating conventional radiation detectors into the robot and surveying radiation fields in areas of interest. This is typically done with either a tele-operated system [7][8], or by an autonomous robot [9][10]. Some autonomous robots are capable of using simultaneous localizing and mapping (SLAM) algorithms to map sources of radiation using intensity and range measurement as well as mapping the physical geometry of a local area [11][12]. Another common method of measuring and mapping radiation is by using multiple robots or swarms of robots distributed around an area [13][14][15][16]. However, current robots are not capable of locating sources of radiation in a wide field of view from a single survey point. There are no low cost robots that satisfactorily locate radiation sources, discriminate different types of radiation and display the data intuitively to a human operator in real time. In this context, it is desirable for radiation detection robots to be capable of identifying and locating radioactive sources in potentially unknown areas. Therefore, the goal of this thesis is to establish a reliable method for a small inexpensive mobile robot to:

- quickly locate sources of gamma radiation from a single survey point,
- identify radioisotopes with high resolution,
- visually convey the information to a remote human operator,
- display the radiation data in a manner that is easily and intuitively understood by the human operator.

The material in this thesis is presented as follows. Chapter 1 reviews some of most important and relevant theoretical aspects of radiation and radiation detection. Additionally, theory related to the physical design and geometry of the gamma ray detector used in this thesis is presented. Chapter 2 describes the robot's design and presents a prototype that was constructed in order to test the methods developed in this thesis. The methods of the robot's operation are outlined and the experiments designed to test these methods are explained in detail. Chapter 3 presents the experimental results of a series of experiments performed using the University of Ontario Institute of Technology (UOIT) radiation facilities. The main findings are summarized in the conclusion. Some limitations of the prototype are reviewed and a multitude of possible future work is presented. A final summary of the entire thesis is offered. Additional figures, diagrams and tables are included in the Appendices.

Chapter 1: Theoretical Background

1.1 Radiation Sources

Before designing a system to detect radioactive sources, it is important to consider the origin of radiation and the behaviour of both the sources and the radiation itself. There are a vast number of types of radiation with significantly different properties. Indeed radiation is omnipresent throughout the universe. Background radiation refers to the constant level of radiation that exists in an area on earth due to terrestrial sources as well as cosmic radiation. The focus of this review will be radiation that is typically encountered in man-made radioactive hazards from nuclear reactor fission products, medical isotopes and natural terrestrial sources such as uranium.

The specific radioactive particles reviewed will be charged particles (protons, alpha and beta), photons (x-ray and gamma ray), and neutrons. The energy carried by these individual particles varies over a large range. The details of exposure, dose, and damage to human health from these kinds of radiation will not be discussed in this thesis since it is well covered in the literature [17]. However, the assumption is that exposure to high doses of radiation is inherently detrimental to human health and must be avoided.

Charged Particles - Radiation in the form of charged particles is generally considered in two prominent groups. The first is light charged particles (beta radiation) which include electrons and positrons. The second group is heavy charged particles which include protons, alpha particles and other heavier particles such as fission product nuclei. Very heavy nuclei are usually intrinsically unstable and alpha particles may be spontaneously ejected from the nucleus following nuclear deformations. In some cases the nuclei of very heavy isotopes may spontaneously fission and eject fission fragments as well as neutrons. Beta radiation comes from

spontaneous beta decay of unstable isotopes wherein a neutron is converted into a proton and an electron is ejected (beta minus radiation: β^-). Alternatively, in some isotopes a proton may be converted into a neutron and a positron is ejected from the nucleus (beta plus radiation: β^+) [18].

Many fission product nuclei contain too many neutrons for stability and beta minus decay is very common in many of these isotopes. Likewise, neutron capture produces a similar result for many materials present in a nuclear reactor [19].

Heavy charged particles from the sources considered in this review typically interact very strongly with matter and consequently have very short mean free paths through material and air. This means that directly detecting and locating an unknown source of such particles with a mobile robot that may be situated several meters or more away from the source would be difficult. Beta radiation from these sources typically has a larger mean free path than heavy charged particles with similar energies. However, these particles tend to be deflected at large angles very often and produce chaotic paths as they travel through air and other material. Both of these forms of charged particles produce significant amounts of secondary radiation as they travel through material and collide with or interact with atoms. The secondary radiation includes ejected atomic electrons, photons (x-rays) and other high energy bremsstrahlung photons[18].

Photons- Many radioactive sources emit gamma rays and x-rays. Gamma rays originate inside nuclei when constituent particles shift their configuration within the nucleus and de-excite to a less energetic states. The resulting gamma ray leaves the nucleus at the speed of light carrying away the energy loss of the reconfigured nucleus. X-rays are analogous except they are produced by de-excitations of electrons in the electron shell configuration of bound electrons. Beta radiation is ubiquitous in fission products because they generally have too many neutrons for

stability and the secondary particles and x-rays produced by beta decay are consequently omnipresent. Beta decay also frequently leaves the resulting nucleus in an excited state and gamma rays follow this process to bring the nucleus to its ground state. Moreover, bombardment of materials with neutrons inside a nuclear reactor frequently makes neutron activated nuclei which may be in an excited state and subsequently release gamma rays as the nuclei de-excite to a stable state. Indeed, both gamma and x-ray photons are ubiquitous in spent nuclear fuel, nuclear reactor core material, and other components that may be present in a nuclear accident[19].

Neutrons have a complicated behaviour and their interactions with material vary greatly with energy. Neutrons may be difficult to detect and measure due to their lack of charge and complicated interactions with matter. Neutrons can also pose a significant risk in nuclear accident scenarios due to their high lineal energy transfer (LET).

1.2 Gamma Ray Interaction with Matter

Gamma rays may interact with either the nucleus or the electrons of atoms as they pass through matter. The three principal interaction mechanisms of gamma rays in matter are as follows.

Photoelectric effect (PE): In this process an atomic electron absorbs the total energy of the incident gamma photon and is ejected from its electron shell. The electron may remain bound to the nucleus in an excited state or leave the atom as a free charged particle.

Compton scattering (C): In this process some of the energy of the incident gamma photon is transferred to an atomic electron. The gamma ray is scattered and continues in a new trajectory

with a decreased energy proportional to the angle of deflection. The electron recoils with energy proportional to the energy loss of the photon. The electron may remain bound to the nucleus in an excited state or leave the atom as a free charged particle.

Pair production (PP): When gamma rays have energies above the rest mass of an electron and positron pair (1.02 MeV), gamma photons may interact with the coulomb field of a nucleus and spontaneously produce an electron and positron pair [20]. This produces a pair of free charged particles.

The three interaction mechanisms listed above contribute to the attenuation of gamma rays as they pass through matter. Compton scattering does not eliminate the gamma ray, rather it decreases the energy and scatters the resulting photon. Positrons created in PP will undergo annihilation with electrons and produce further gamma radiation. This means that the attenuation of incident gamma radiation does not entirely eliminate photons; however, the energy of the incident gamma photons are generally absorbed by electrons throughout the material and the remaining gamma rays are less energetic and deflected at various angles. The attenuation of an incident gamma ray beam can be described by the total linear attenuation coefficient, μ_{total} . The total linear attenuation coefficient describes the interaction probability, P , of a gamma ray as it travels a distance, x , through a material. dP is the instantaneous interaction probability of a gamma ray as it travels an infinitesimal distance, dx , through the material. μ_{total} is the sum of the linear attenuation coefficients from the three possible interaction mechanisms, μ_{PE} , μ_{C} and μ_{PP} where μ_{PE} is the linear attenuation coefficient for the photo-electric effect, μ_{C} is the linear attenuation coefficient for Compton scattering, and μ_{PP} is the linear attenuation coefficient for pair production.

$$\mu_{\text{total}} = \mu_{\text{PE}} + \mu_{\text{C}} + \mu_{\text{PP}} \quad (1)$$

The instantaneous interaction probability of gamma rays as they pass through a distance dx of material with a total linear attenuation coefficient, μ_{total} , is described by:

$$dP = \mu_{\text{total}} \cdot dx \quad (2)$$

A gamma ray beam entering a material has an initial intensity I_0 . As the beam travels through the material, all three interactions will serve to attenuate the beam. $I(x)$ describes the intensity of the gamma ray beam as a function of the distance traveled through the material, x . So the instantaneous attenuation of the beam dI as it travels a distance dx is given by:

$$dI = -dP \cdot I(x) = -\mu_{\text{total}} dx \cdot I(x) \quad (3)$$

And the instantaneous linear attenuation per unit distance is

$$\frac{dI}{dx} = -\mu_{\text{total}} I(x) \quad (4)$$

This is a first order linear differential equation. Solving with the initial condition that the beam intensity is I_0 as the beam enters the material gives the equation for the beam intensity as a function of distance traveled [20].

$$I = I_0 e^{-\mu_{\text{total}} x} \quad (5)$$

The intensity of the beam is decreased exponentially as the beam passes through the material. The attenuation coefficients μ_{PE} , μ_{C} , and μ_{PP} depend on the gamma photon energy and the properties of the material, most notably the density of electrons in the material. Since the attenuation interactions mostly depend on the gamma rays approaching an atomic electron or atomic nucleus, increasing the density of the material will significantly increase the attenuation.

Thus, heavy elements with a high atomic number and large bulk density will attenuate gamma radiation more than lighter elements. Gamma ray attenuation could be used to determine incident direction in a directionally insensitive detector provided the incident gamma radiation is differentially attenuated according to incident angle.

1.3 Gamma Ray Energy Spectra

Gamma rays originate from de-excitations inside an unstable nucleus. The configuration of particles inside a nucleus is very specific to a particular isotope. The possible excited states of nuclei inside an unstable isotope are also specific to different isotopes. The energy carried away by a gamma ray directly reflects the energy levels of the originating nucleus. Therefore, any instrument that is able to accurately measure the energy of an incoming gamma ray is in fact also measuring the energy of a de-excitation inside the originating nucleus [21]. Consequently, the radioactive isotopes present in a source can be directly observed and positively identified according to the energy spectra of gamma rays that are measured. Figure 1 shows a representation of the nuclear energy levels associated with the de-excitation of two common gamma ray emitting isotopes. The figure shows that the excited state of ^{60}Ni emits two gamma rays following β^- decay of the original ^{60}Co nucleus. The figure also shows that the characteristic 662 keV gamma photon of ^{137}Cs is the result of a de-excitation of ^{137}Ba [18].

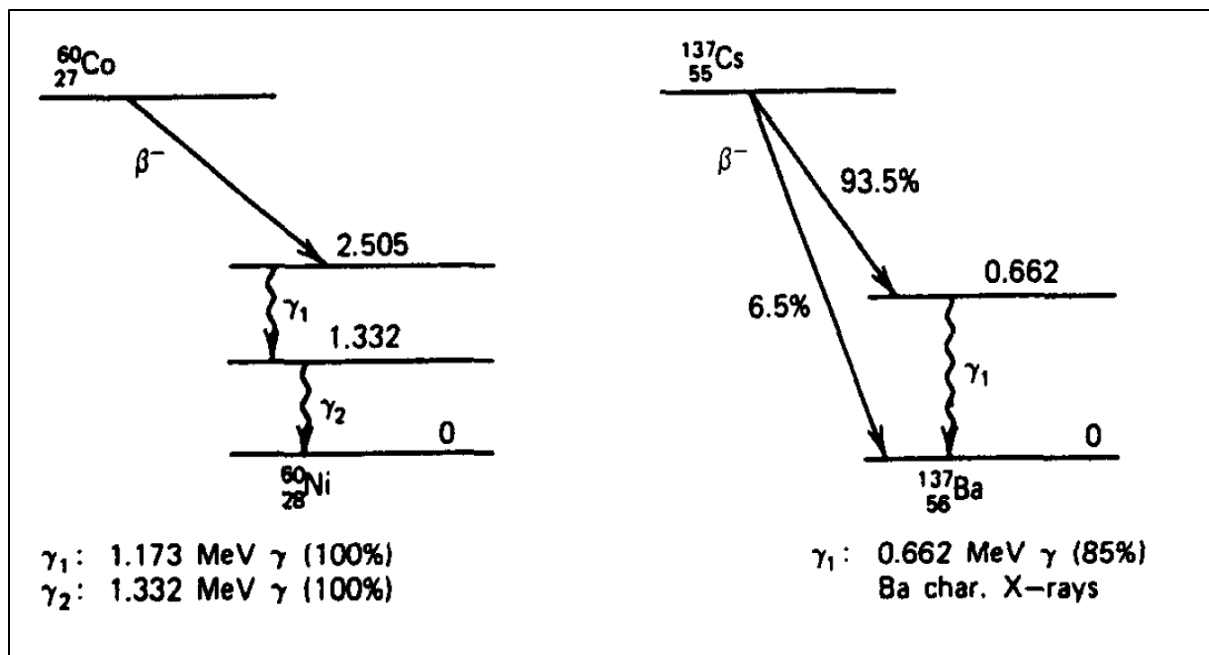


Figure 1: Characteristic gamma rays emitted from ^{60}Co and ^{137}Cs [18]. The horizontal lines represent energy levels in the nucleus. Arrows represent a transition of the nucleus from one energy level to a lower energy level. The wavy arrows represent the gamma rays that are released as the nucleus de-excites from an excited energy state to a lower energy state.

1.4 Gamma Ray Detectors

1.4.1 Overview of Gamma Ray Detectors

Gamma ray detectors generally operate on the principle of converting the energy deposited in the detector volume into a measurable quantity; typically an electric signal. Detectors using gas filled chambers achieve this by holding a strong electric field between an anode and cathode separated by a gas inside the detector volume. When a gamma ray enters the detector, the photoelectric effect, Compton scattering, and pair production will create ionizations within the gas. Electrons and positively charged gas ions are accelerated in opposite directions toward the anode and cathode, respectively. The collection of the electrons along the anode results in a

measurable current pulse. Ionization chambers, proportional counters, and Geiger-Muller tubes all essentially operate on this main principle [18]. Scintillation detectors are another common kind of detectors which also produce an electronic current as a result of a gamma ray interaction. However, there are several important intermediate steps that will be discussed in the next section. Scintillation detectors are generally considered to be excellent tools for detecting gamma rays and performing gamma ray spectrometry (isotope identification).

1.4.2 Scintillation Detectors

Scintillation materials are solids, liquids or gases that produce photons of light as a result of interaction with incident radiation. The radiation interacts and transfers energy to the electrons of the scintillation material within the detector. The excited electrons de-excite to a lower energy state and photons of light are emitted. In a typical scintillation detector the photons of light produced by the radiation will pass through the transparent scintillation material and produce photoelectrons due to photoelectric interactions at the photocathode of the detector's photomultiplier tube (PMT). The PMT serves as an amplifier to amplify the current of the electrons produced at the photocathode. These photoelectrons are multiplied by a factor on the order of 10^6 or more within the photomultiplier tube and are collected at the anode to produce a detectable current pulse. The current is then amplified within an electronic preamplifier and amplifier. The result is a current pulse that has a height and pulse shape which is proportional to the energy transferred to the scintillation material from the original radiation. A multichannel analyzer (MCA) is used to discern the current pulse characteristics and place a count into one of the detector's energy channel bins. Collecting a large number of counts creates a frequency

histogram and spectra of the incoming radiation can be observed [18]. A simplified diagram of this process is shown in Figure 2.

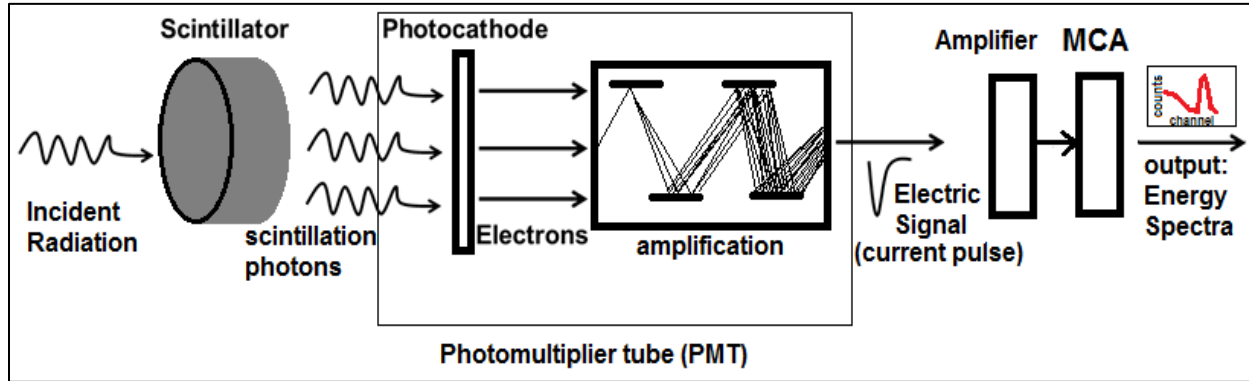


Figure 2: Schematic of a scintillation spectrometer. The incident radiation, shown on the left, causes scintillations producing photons of light when it interacts with the scintillator. The central block represents the PMT where the scintillations of light are converted into an electric current and amplified. The right side of the figure shows the amplifier and MCA used to measure the current pulses and produce an energy spectrum.

Unfortunately, the precise energy of an incoming gamma ray cannot always be perfectly measured by any feasible detector. Gamma ray energy spectra are generated by detecting gamma rays and plotting a frequency histogram with measured gamma ray energies as the bins on the x-axis and the number of counts (or count rate) on the y-axis. If a mono-energetic source of gamma rays is detected with a statistically significant number of photons the spectra will assume the shape of a Gaussian peak with the centre of the peak near the true energy of the incident photons. Other gamma ray energies below the true energy will be counted due to interactions inside the detector that only transfer part of the original gamma ray energy to the detector. This is primarily due to Compton scattering and to the measurement of secondary and scattered radiation. Energies above the true energy of the incident particle can be measured as a result of coincidence where multiple particles reach the detector simultaneously and are measured as a single count. The amount of error in the energy measurement inherent in the detector is indicated by the width

of the Gaussian formed about the peak. This is often characterized by the full width at half maximum (FWHM) which measures the width of the Gaussian shape when the number of counts has reached half of the peak value. The detector resolution is often described by the ratio of the mean energy (H_0) of the gamma peak and the FWHM.

$$\text{resolution} = \frac{\text{FWHM}}{H_0} \cdot 100\% \quad (6)$$

In order to accurately measure the energy of an incoming gamma ray it is desirable to have a detection system that produces the smallest possible FWHM, i.e., high resolution detection.

Figure 3 shows an ideal gamma ray energy spectrum and a typical measured spectrum [18].

The top of Figure 3 shows a gamma ray point source (represented by a star) that is emitting mono-energetic gamma rays. These are measured by the detector (represented as a circle). The gamma ray paths are represented as wavy arrows. The numbers 1-3 represent three common gamma interactions that result in energy measurements less than the energy of the gamma rays leaving the source. The bottom of the figure shows the spectra measured by the detector. The large peak on the right of the spectrum represents the photo-peak which is centered on the energy H_0 . This is the measurement of the energy of gamma rays from the source. 1) Shows a path in which a gamma ray Compton scatters inside the detector volume. Only part of the energy is measured by the detector. This results in a continuum on the spectra. 2) Shows a path in which a gamma ray interacts with material outside the detector and produces electrons in excited states, which de-excite and release x-rays. Characteristic x-rays of the material may reach the detector and be measured as an “x-ray peak” shown in the spectra. 3) Shows a path where gamma rays Compton scatter off of material outside the detector, are reflected by a large angle, and enter the detector where they are measured. This results in the “backscatter peak” shown in the spectrum.

The dashed line on the bottom of the figure represents how the spectra would appear with a “perfect” detector that was subject to no noise, background radiation, coincidence measurements, or any other effects that could disturb the spectra. The solid line in the spectra represents a typical spectrum that represents how spectra typically appear when measuring a mono-energetic gamma source including effects due to background radiation, coincident particles, electronic noise, and other measurement noise.

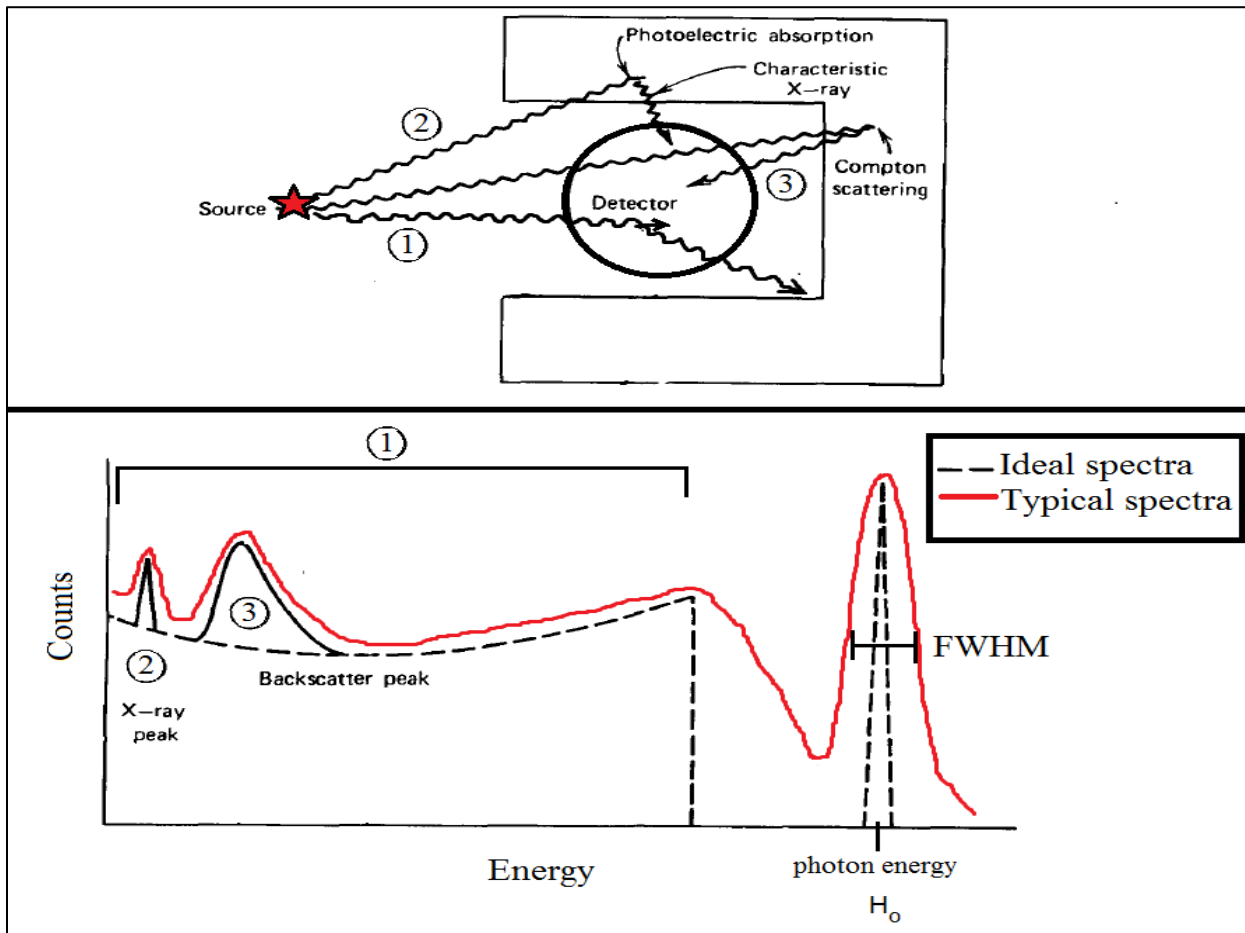


Figure 3: Schematic of a detector and source (top) with typical gamma ray paths that produce spectral peaks below the sources photo-peak (numbers 1-3). The bottom shows the spectra measured by the detector with a “perfect” detector (dashed line) and a typical detector (solid line) [18]

Common scintillation materials include organic scintillators, liquid and gaseous scintillators, and inorganic crystal scintillators. Inorganic crystal scintillators such as sodium iodide (NaI), cesium iodide (CsI), and lanthanum bromide (LaBr_3) are convenient for small handheld detection systems or small detectors on robots since the crystals are dense, compact and do not require cooling.

1.5 Lanthanum Bromide Scintillation Detector

Lanthanum bromide scintillation detectors function similarly to NaI and other conventional inorganic crystal scintillation detectors. The crystal consists of a LaBr_3 lattice doped with a cerium activator. LaBr_3 detectors have better energy resolution than NaI detectors and a greater light yield as well as a much shorter decay time. The bulk density and the total linear attenuation coefficient of LaBr_3 is also larger than NaI and thus the intrinsic efficiency of LaBr_3 detectors is greater than NaI for equivalent geometries (See Appendix A). This makes LaBr_3 ideal for rapid count measurements, spectral analysis, radioisotope identification, and gamma source localization [22]. Unfortunately, LaBr_3 detectors do have some inherent disadvantages such as intrinsic internal radioactivity as a result of the naturally occurring isotopes ^{138}La and ^{227}Ac . ^{138}La may beta-decay to stable ^{138}Ce producing a characteristic 788.7 KeV gamma ray. Alternatively ^{138}La may undergo electron capture and produce a 1435.8keV gamma ray while transitioning to stable ^{138}Ba which may emit Ba K x-rays with energies between 31-38 keV. Due to chemical similarities, ^{227}Ac is an omnipresent impurity in LaBr_3 detectors and exists naturally as part of the ^{235}U decay chain. ^{227}Ac undergoes five alpha decays in a decay chain descending to stable ^{207}Pb and this produces several detectable gamma rays. Since these radioactive isotopes

are present inside the detector volume, a spectra measured by a LaBr_3 detector will always detect radiation with the energies presented above, even if no other radioactive sources are present. Most notably in a radiation background spectra, high energy gamma with energy between 1550 keV and 3000 keV can be observed. This intrinsic natural radiation measured by LaBr_3 detectors contributes significantly to measurements of background radiation [1]. Figure 4 shows a 60,000 second unshielded radiation background measurement with a LaBr_3 detector identical to the one used in this thesis (See Appendix B for comparison with shielded NaI detector background spectra). The gamma peaks from the internal sources listed above are clearly visible and indicated on the figure. This means that spectra measured from weak sources or sources measured from large distances (such that the signal to noise ratio of the source compared to the radiation background is poor) may need to consider these effects.

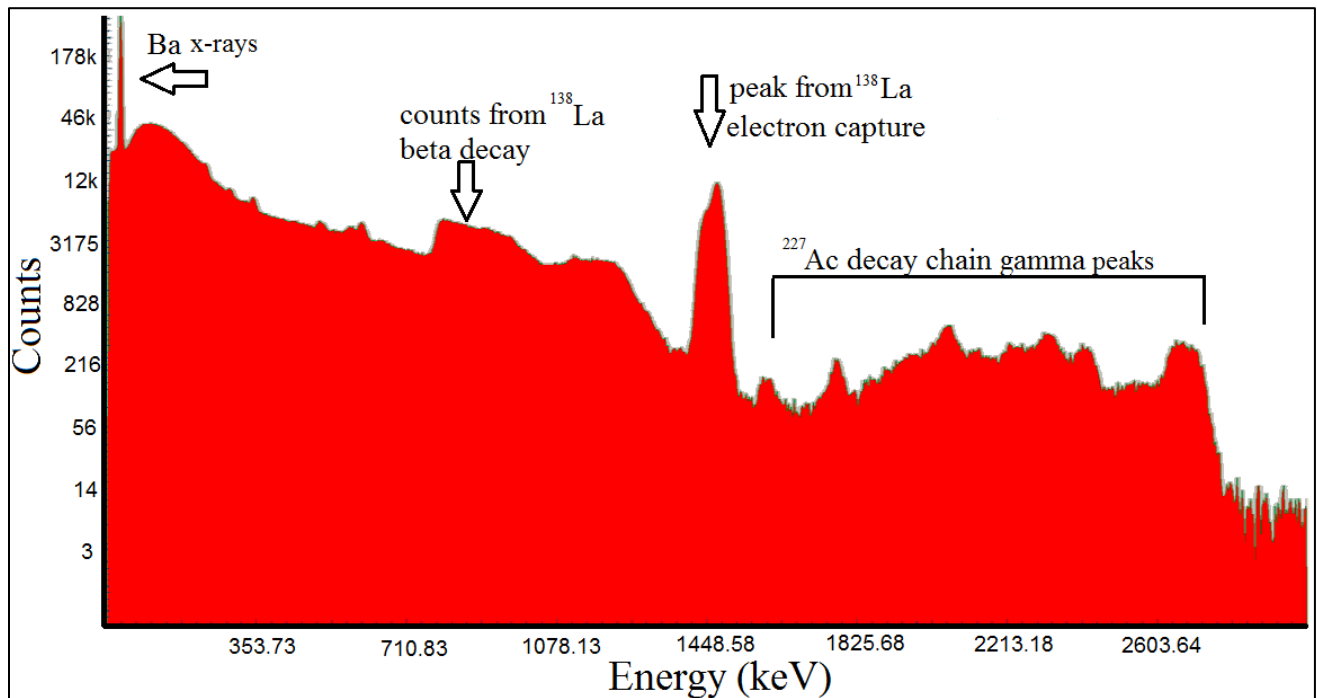


Figure 4: 60,000 second background spectra with LaBr_3 detector [1]. This spectrum shows peaks that you will measure with a LaBr_3 detector, even if no gamma sources are present.

1.6 Directional Sensitivity of Cylindrical Scintillation Detectors

A paper by Klann et al. provides an excellent method for analytically determining the angular efficiency of a cylindrical inorganic scintillation detector [23]. For a scintillation detector to measure an incident gamma ray, there must be an interaction with electrons within the crystal. For a gamma ray passing through the scintillation material we can use the attenuation of the gamma ray in the material as an indication that the gamma ray has interacted with the material and thus been detected. So using equation (5) we see that the un-attenuated portion of incident gamma radiation is given by $I_0 e^{-\mu_{\text{total}} x}$ and conversely the portion of the beam that has been detected is $I_0 (1 - e^{-\mu_{\text{total}} x})$. Here we will redefine μ_{total} as the total linear attenuation coefficient of the detector, μ_{detector} , to indicate that these gamma rays are being attenuated by the detector material. The path length of a gamma ray through the detector, x , will hence be called x_{detector} and it will vary greatly depending on the source position, incident direction, and detector geometry. So we have $I_0 (1 - e^{-\mu_{\text{detector}} x_{\text{detector}}})$. Figure 5 shows a model of a cylindrical LaBr_3 detector measuring a point source of gamma rays represented as a star. For a given source position and detector geometry the path length of the gamma rays through the detector will vary depending on the direction of the path. The path direction can be described by the horizontal angle, θ , and azimuthal angle ϕ as shown on the figure.

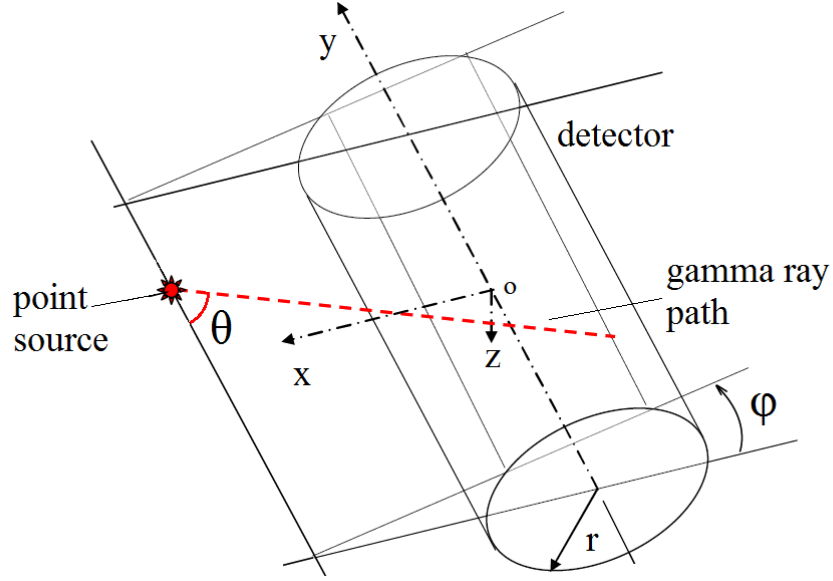


Figure 5: Three dimensional configuration of detector and point gamma source model [23]. The detector is represented as a cylinder. The point source emits gamma rays which may enter the detector volume. The dashed line represents the path of one gamma ray that enters the detector volume.

The portion of the gamma rays in a path that enters the detector volume are attenuated (and thus detected) is given by $I_0(1 - e^{-\mu_{\text{detector}}x_{\text{detector}}})$. The ratio of the number of gammas that are detected by the detector compared to the number of gammas that enter the detector volume is called the intrinsic efficiency.

The intrinsic efficiency is given by:

$$\varepsilon_i = (1 - e^{-\mu_{\text{detector}} \cdot x_{\text{detector}}(\varphi, \theta)}) \quad (7)$$

In addition to this intrinsic efficiency there is also solid angle efficiency which describes how many of the gamma rays emitted from a given source will actually hit the detector.

The solid angle of the detector with respect to the point source of radiation is given by:

$$\Omega = \iint \sin \theta d\theta d\varphi \quad (8)$$

And the solid angle efficiency of the detector is given by:

$$\varepsilon_{SA} = \frac{\Omega}{4\pi} \quad (9)$$

The total counting efficiency ε_T is the combination of the intrinsic efficiency ε_i and the solid angle efficiency ε_{SA} and is given by,

$$\varepsilon_T = \varepsilon_i \cdot \varepsilon_{SA} \quad (10)$$

Combining equations 7-10 and considering all paths of gamma rays through the detector volume from a given source position gives the total counting efficiency.

$$\varepsilon_T = 2 \int_0^{\varphi_0} \int_{\theta_{min}}^{\theta_{max}} (1 - e^{-\mu_{detector} \cdot x_{detector}(\varphi, \theta)}) \sin(\theta) d\theta d\varphi \quad (11)$$

where $x_{detector}$ is the path length of a vector pointing through the detector from the point source at horizontal angle θ and azimuthal angle φ . Details for computing $x_{detector}(\theta, \varphi)$ are shown in [23]. The point source is confined to a position in the x,y plane outside of the detector as shown in Figure 5.

The horizontal angle θ of gamma rays that actually reach the detector lie between θ_{min} and θ_{max} which both depend on the azimuthal angle φ . Hence, equation (11) above takes the form of elliptic double integrals. We constructed a MATLAB program to perform these double integrals numerically. The MATLAB program used produced identical results to Klann et al. for identical point source position and detector parameters presented in the original paper [23]. In the program, the source is placed at a position outside of the detector and the total counting efficiency is calculated using equation (11). The program was used to measure the total counting efficiency of the detector while measuring a point source positioned 2 m away from the center of

the detector at various directions. Figure 6 shows how the point source is positioned and rotated relative to the detector in the program. The MATLAB program output in Figure 7 shows the calculated total counting efficiency of a 1.5 by 1.5 inch (3.81 cm diameter and 3.81 cm height) cylindrical LaBr₃ detector like the one used in this thesis as a function of point source angle as it is rotated in a 180° arc around the forward direction of the detector; starting from the right side of the detector (+ x axis direction) and ending at the left side (-x axis direction) at a distance of 2m from the center of the detector. The source modeled is ¹³⁷Cs.

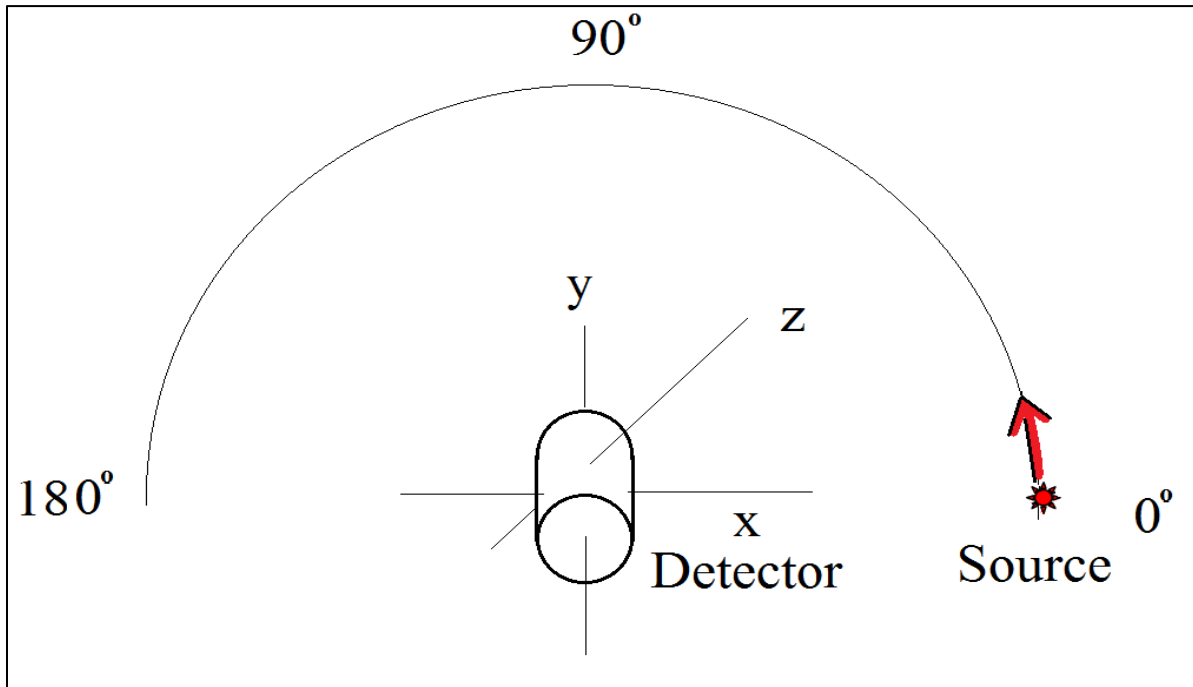


Figure 6: Schematic of point source arc around detector in MATLAB program. A gamma ray point source is represented as a star. The program measures the total counting efficiency of the detector while measuring the source at all positions on the arc, starting at 0° and ending at 180°

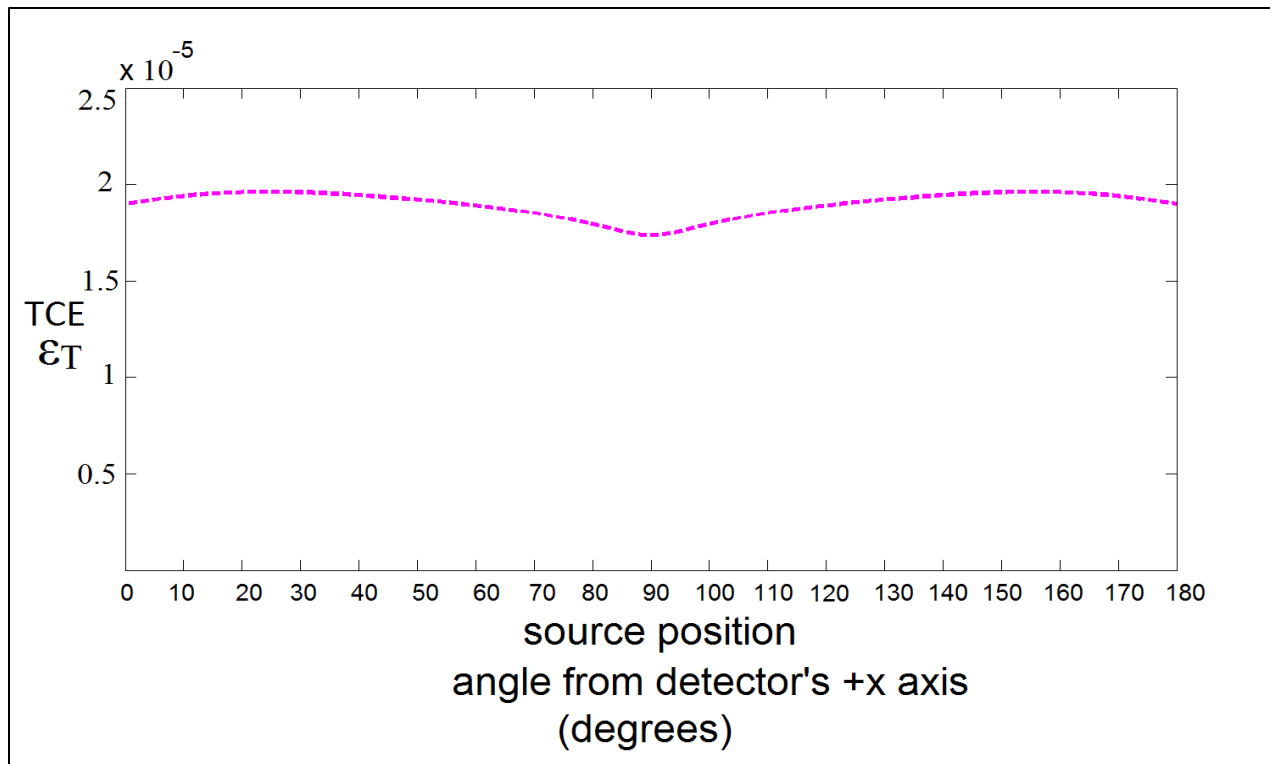


Figure 7: Directional sensitivity of cylindrical LaBr₃ detector. The output of the MTLAB program shows a plot of detector total counting efficiency while measuring a ¹³⁷Cs point source located 2m away from the center of the detector as a function of angle.

1.7 Point Source Triangulation

The two dimensional position of a point can be determined from two or more directional measurements from known positions. Thus, if a mobile robot can discern its own position and orientation on a two dimensional plane and can accurately measure the direction of a point source gamma emitter in that plane, the position of the gamma source may be determined using two or more unique measurements. Measuring the direction of the gamma emitter from three or more known positions will result in an over-constrained system and this may be used to statistically reduce the total error inherent in a point source position estimate. Figure 8 illustrates this concept using a pre-defined 2 dimensional rectangular coordinate system. In this coordinate

system the gamma ray point source occupies a position defined as $(x,y)_{source}$. The robot measures the direction of the source relative to robot's position. The robot repeats directional source measurements from four known positions $(x,y)_{robot\ 1,2...4}$. The robot is oriented so that the forward direction is always oriented toward the +y axis at all four positions.

A directional measurement of the source from the first known position, $(x,y)_{robot\ 1}$ produces a line intersecting the axis of the detector, the position of the robot, and the position of the point source. The angle of the source direction relative to the robot is shown on Figure 8 as θ_{s1} . This provides the slope and a known point of a line in a plane. Thus, a linear equation passing through the unknown source location $(x,y)_{source}$ and the current known position of the robot $(x,y)_{robot1}$ is determined. The slope, m , of the line in the coordinate system is given by,

$$m_1 = \tan (\theta_{s1}) \quad (12)$$

The y-intercept (b_1) in the coordinate system is given by,

$$b_1 = y_{robot1} - m_1 \cdot x_{robot1} \quad (13)$$

Giving the linear equation,

$$y_{source} = m_1 x_{source} + b_1 \quad (14)$$

The angle measurement is then repeated from a series of n unique known positions giving the following system of linear equations for the source position $(x,y)_{source}$.

$$y_{source} = m_1 x_{source} + b_1$$

$$y_{source} = m_2 x_{source} + b_2$$

⋮

$$y_{source} = m_n x_{source} + b_n \tag{15}$$

A map showing the line equations calculated from source direction measurements at four known points is shown in Figure 8. The source position is represented as a red star in the figure. The slopes and y-intercepts are indicated on the figure.

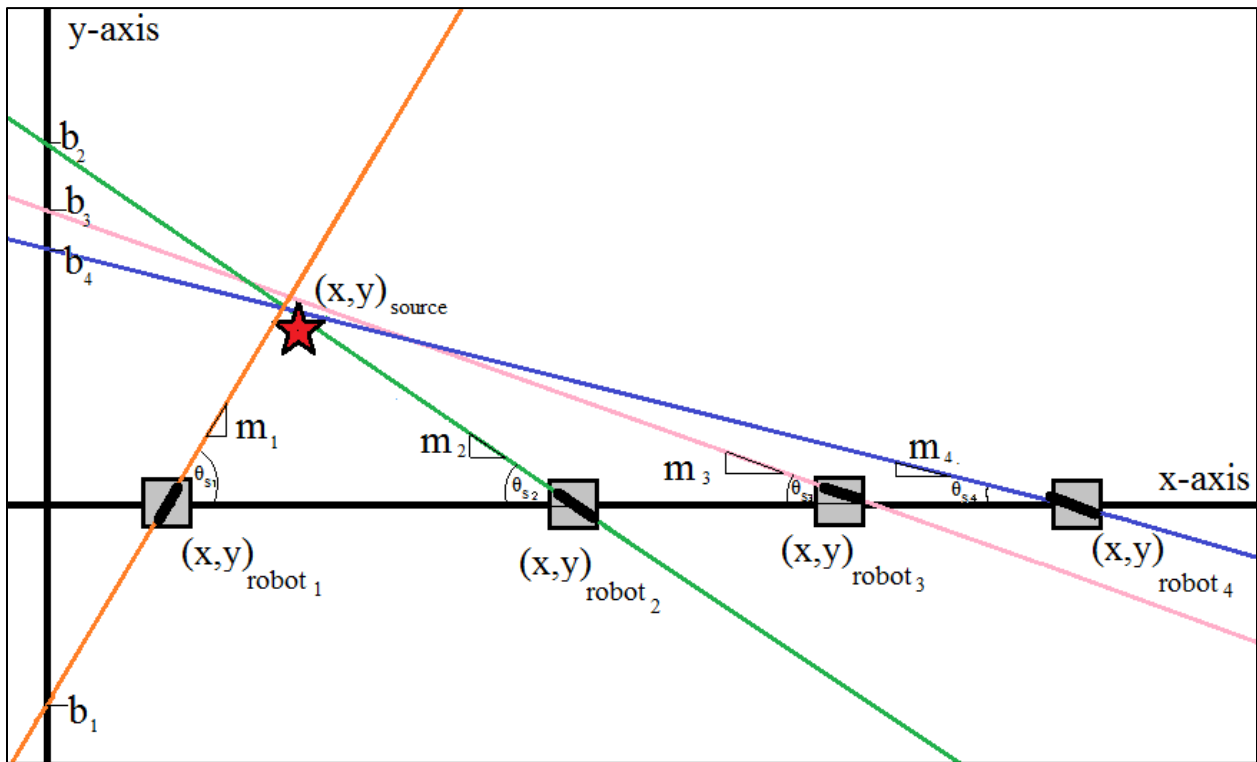


Figure 8: Linear equations determined by robot at four known measurement positions

Arranging the system of equations from equation (15) into matrix form gives the following

$$\begin{bmatrix} -m_1 & 1 \\ -m_2 & 1 \\ \vdots & \vdots \\ -m_n & 1 \end{bmatrix} \begin{bmatrix} x_{source} \\ y_{source} \end{bmatrix} = \begin{bmatrix} b_1 \\ b_2 \\ \vdots \\ b_n \end{bmatrix} \quad (16)$$

This can be expressed more compactly as

$$A \bar{v} = \bar{b} \quad (17)$$

Where A is the coefficient matrix containing the calculated slope terms, \bar{v} is the variable vector for the source position $(x, y)_{source}$ and \bar{b} is the y-intercept vector containing the calculated coordinate system y-intercept values.

This is an over constrained system of linear equations and will in general be inconsistent unless all directional measurements intersect at the exact same point. Due to imperfect measurements and measurement noise this will usually not be the case. The best approximate solution for the position of the point source can be obtained using the method of ordinary least squares. This will provide the estimated source position $(x, y)_{source}$ that minimizes the total error in the system [24].

$$\text{Estimated Source Position } (x, y) = \min_{\bar{x}} \| A\bar{v} - \bar{b} \| \quad (18)$$

And so using the method of ordinary least squares we get,

$$\text{Estimated Source Position } (x, y) = (A^T A)^{-1} A^T \bar{b} \quad (19)$$

Chapter 2: Methodology

Methodology Overview

With the thesis goals in mind (presented in the Introduction), we present an inexpensive and effective method for a small mobile robot equipped with a single and high resolution scintillation detector to trace local point sources of gamma radiation and convey the gamma ray information visually to a human operator. The approach consists of using a lead cylinder surrounding a lanthanum bromide detector as a collimator for incoming gamma rays. Thus, only gamma rays approaching along the detector's forward axial direction are detected without being attenuated by the lead collimator. The detector count rate measurements are taken by the robot autonomously in an adjustable number of directions in the horizontal plane of the robot and a directional profile of gamma rays is constructed. The directional gamma ray profile is then overlaid onto a visual panorama taken by a digital camera mounted on the robot's detector. The direction of the largest gamma ray measurement is stored in the robot's memory and the camera is rotated so that the gamma ray source will appear in the horizontal center of the robot operator's field of view. We also incorporate measurements of gamma ray energy spectra so that specific gamma ray emitting isotopes can be identified. With this method it is possible not only to identify the direction, but also the relative intensity and the composition of multiple radioactive sources in the area around the robot. The detector system used in the design presented in this thesis does not have any appreciable neutron measuring capability [25]. Detecting and measuring alpha and beta radiation with a robot located at distances of several meters from a point source is also difficult due to attenuation as discussed in Section 1.1. Hence, the robot design presented in this thesis will use a detector that is designed to measure gamma radiation. This is because the intention of the robot

is to measure, locate and identify radioactive sources from a single survey point at distances on the order of several meters away from the source location. Gamma ray photons are ideal for this kind of measurement since they tend to be emitted iso-tropically and diverge from the source in primarily straight lines through air [18]. The mobile robot design in this thesis is concerned with locating stationary gamma ray emitting sources that are approximately point sources. The robot's point source search measurements are confined to regions near (within a few cm) the horizontal plane through the middle of the robot's detector and parallel to the floor.

2.1 Directional Gamma Ray Measurement Method

Figure 7 in Section 1.6 shows that the LaBr_3 detector efficiency varies only slightly for point sources located at different angles around the detector. So as to determine incident gamma ray direction, the detector must be altered to show a strong angular response. Ideally the detector should have a high response in the direction of the point source and a low response in all other directions. A cylindrical lead sheath (collimator) covering the detector and open at the end with a lip beyond the edge of the detector will serve to attenuate incident gamma rays coming from all directions except those close to the detector's axial direction. The intrinsic efficiency of the detector will be decreased for each path that goes a distance x_{lead} through the lead sheath. If μ_{lead} is the total linear attenuation coefficient of lead then the total attenuation of gamma rays traveling a distance x_{lead} through the lead will be

$$I = I_0 e^{-\mu_{\text{lead}} \cdot x_{\text{lead}}(\varphi, \theta)} \quad (20)$$

The attenuation from the lead collimator will serve to decrease the intrinsic efficiency of the detector for all paths of gamma rays that pass through the lead by a factor of $e^{-\mu_{\text{lead}} \cdot x_{\text{lead}}(\varphi, \theta)}$.

The lead collimator can be added to the analytical model presented in Section 1.6 giving the following equation,

$$\varepsilon_T = 2 \int_0^{\varphi_0} \int_{\theta_{min}}^{\theta_{max}} e^{-\mu_{lead} \cdot x_{lead}(\varphi, \theta)} (1 - e^{-\mu_{detector} \cdot x_{detector}(\varphi, \theta)}) \sin(\theta) d\theta d\varphi \quad (21)$$

Where, $x_{lead}(\varphi, \theta)$ is the path length through the lead collimator of the gamma rays going toward the detector at horizontal angle θ and azimuthal angle φ . $x_{detector}(\varphi, \theta)$ is the path length of gamma rays through the detector, μ_{lead} is the linear attenuation coefficient of lead and $\mu_{detector}$ is the linear attenuation coefficient of the detector material (LaBr₃). Equation (21) was incorporated into the MATLAB program presented in Section 1.6 so that the angular response of the detector with the addition of the lead collimator could be calculated. The program was again used to calculate the total counting of the detector while measuring a point source positioned 2 m away from the center of the detector at various directions. The plot in Figure 9 shows the output of the MATLAB program. In the program, a cylindrical LaBr₃ detector enclosed in a 1 cm thick lead sheath with a 2cm lip beyond the end of the detector was modeled. The total counting efficiency is plotted as a function of point source angle as the source is rotated in an 180° arc around the forward direction of the detector (as described in Figure 6). The result for the bare detector from Figure 7 is plotted as well for comparison. There is a large peak efficiency near the axial direction of the detector (at 90°). This means that any detector equipped with this kind of collimator will detect a peak in the detector's count rate when the detector axis is pointed directly at a point source of radiation and a smaller count rate at all other angles.

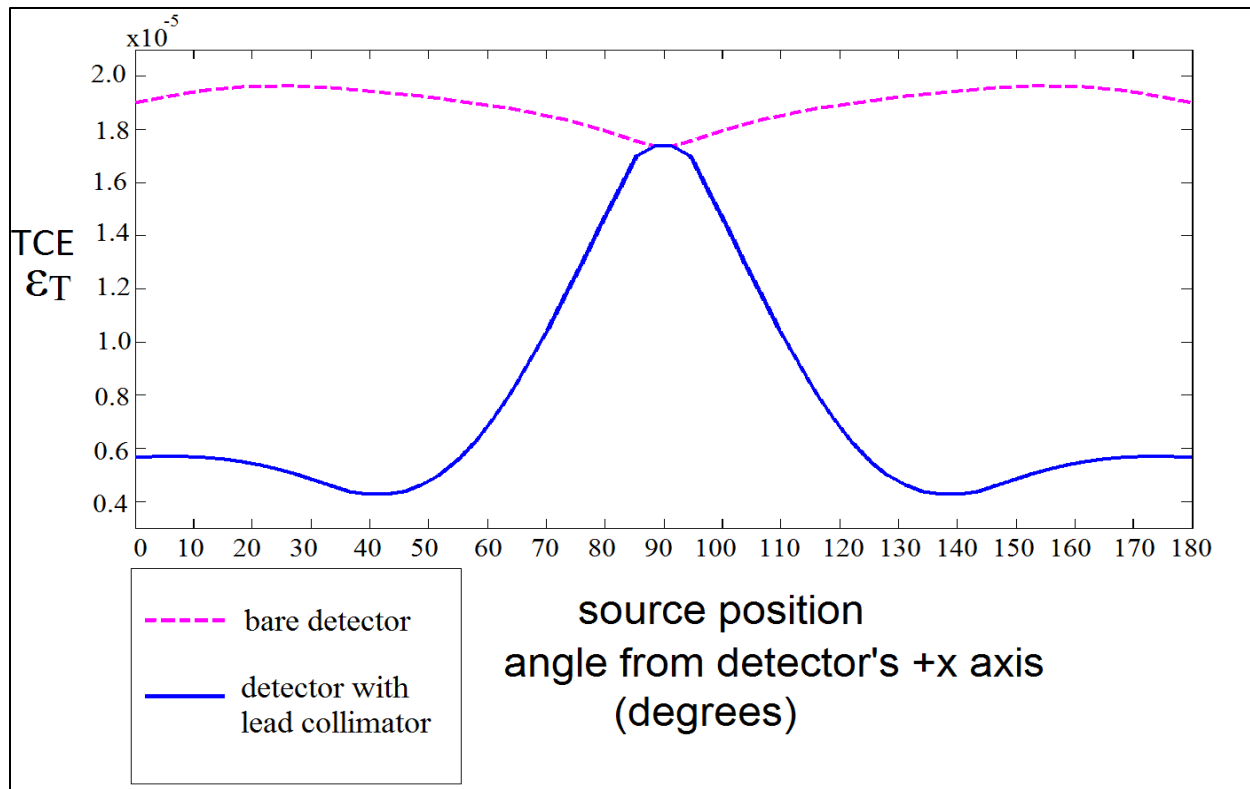


Figure 9: Directional sensitivity of LaBr₃ detector with lead collimator. The graph shows the output of a MATLAB program that calculates the total counting efficiency of a LaBr₃ detector while measuring a point ¹³⁷Cs source at different directions from a distance of 2m. The result with a lead collimator is plotted as a solid line and the bare detector is plotted as a dashed line. The result with the lead collimator shows a large peak efficiency in the detector's axial direction (90°) where there is no lead to attenuate gamma rays.

2.2 Description of the Prototype Design

A prototype mobile robot was designed and constructed with the intention of testing the methods presented in this thesis. The robot body consists of a Lynxmotion 4 wheeled differential drive chassis (shown in Figure 10) and a rotating platform for mounting the radiation detection system. A webcam is mounted on top of the detector to provide visual feed for maneuvering the robot and building visual panoramas of the local area. Four individual electric motors drive each of the wheels independently and are controlled directly by the Sabre-tooth regenerative dual channel

differential drive motor controller system located inside the chassis. A 12 volt Ni-MH battery located inside the chasseur next to the Sabertooth controller provides electrical power for the wheel motors.

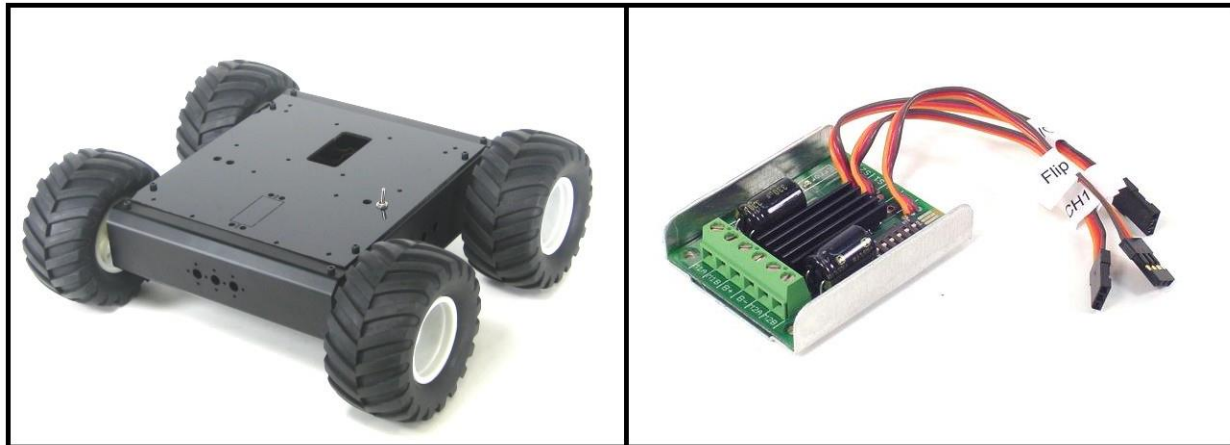


Figure 10: Four wheeled chassis (left) and Saber-tooth differential drive motor controller (right)

The prototype mobile robot designed is 30 cm long, 35 cm wide, 25 cm tall and weighs 4.99 Kg. Figure 11 shows a full external view of the completed prototype with most important components labeled.

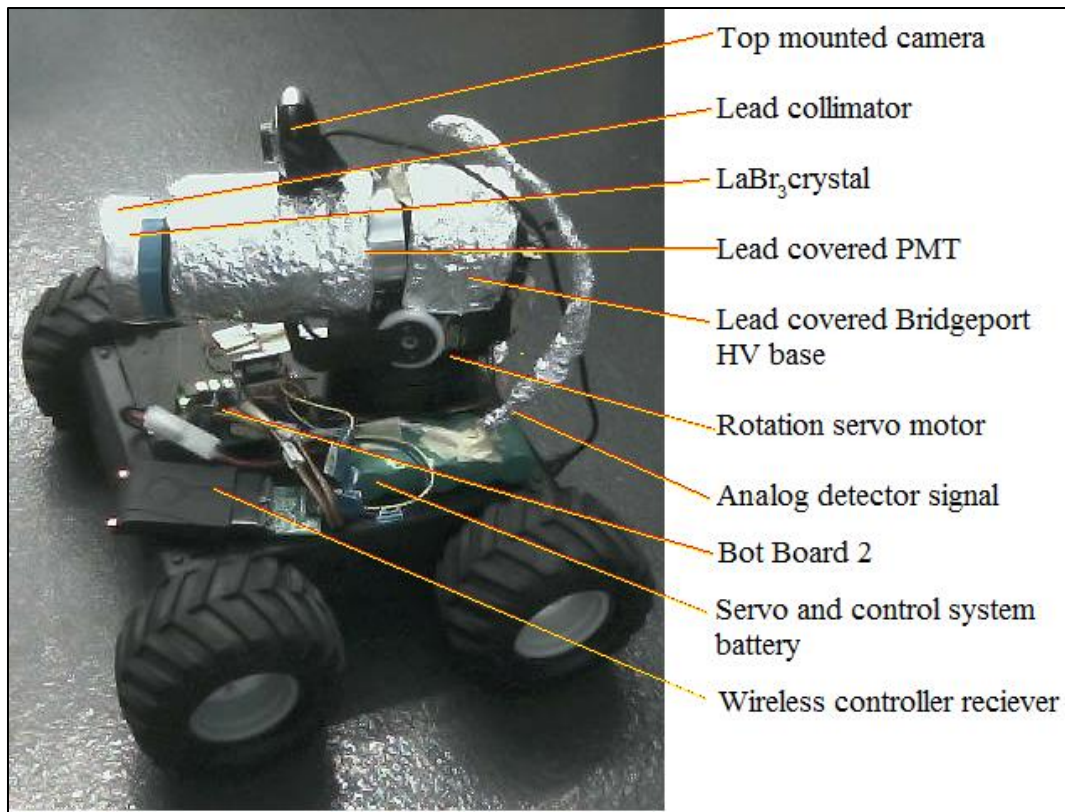


Figure 11: Prototype mobile robot

A 1 cm thick cylindrical lead pipe is used as a collimator for the detection system. The collimator fits around the LaBr_3 crystal and has a 2 cm lip beyond the front of the crystal. The PMT is surrounded by a 0.7 cm thick lead sheath. A Bridgeport HV base is also covered with a 0.4 cm thick lead case. A bracket holds the LaBr_3 detector level so that the detectors axial direction remains parallel to the floor. The detector is held at a height of 21 cm above the ground (measured from the middle of the detector) and the rotation of the detector is limited to the 180° forward direction of the robot due to the servo motor rotation limit. The mobile robot is entirely controlled by the Bot Board 2 control board equipped with a 28 pin Basic Atom Pro microcontroller (shown in Figure 12).

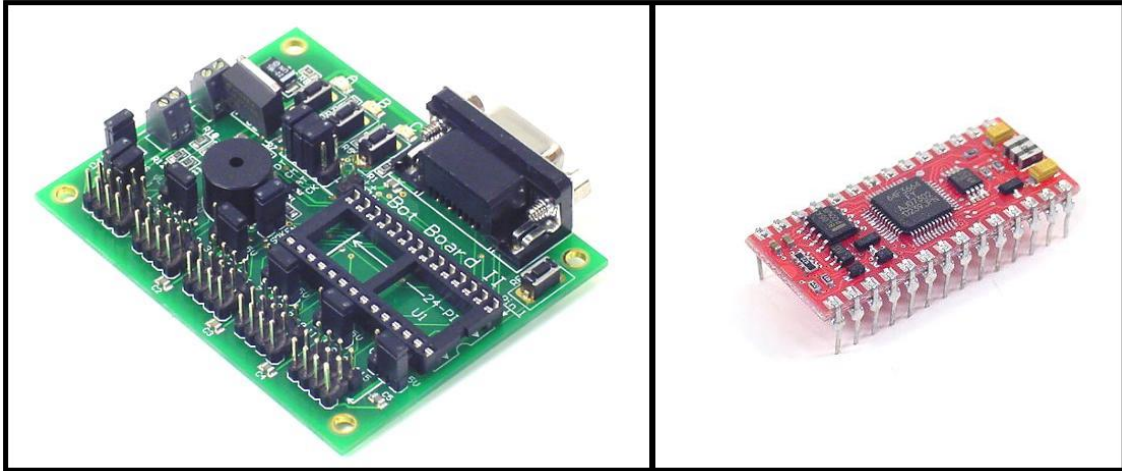


Figure 12: Bot Board 2 (left) and 28 pin Basic Atom Pro microcontroller (right)

Figure 13 shows a detailed schematic of the robot's control system. The pins labeled P0 – 15 (shown on the Bot Board II in Figure 13) act as input and output terminals for the robot's hardware. Output pins P0 and P1 on the board control the dual channel drive motor and maneuver the robot via the Sabertooth controller. Input Pins 12 – 16 receive information from the wireless controller pad and operate the robot in accordance with the human operator. Pin 4 controls the rotating platform carrying the LaBr_3 detector. The positive and negative terminals from Pin 11 are connected to a 3.3 Volt LM1117 voltage regulator and the positive and negative output terminals are connected to the Bridgeport HV base in order to supply high voltage to the LaBr_3 detector. Input Pin AX1 is connected to the LaBr_3 detector's analog output and receives the radiation detection signal.

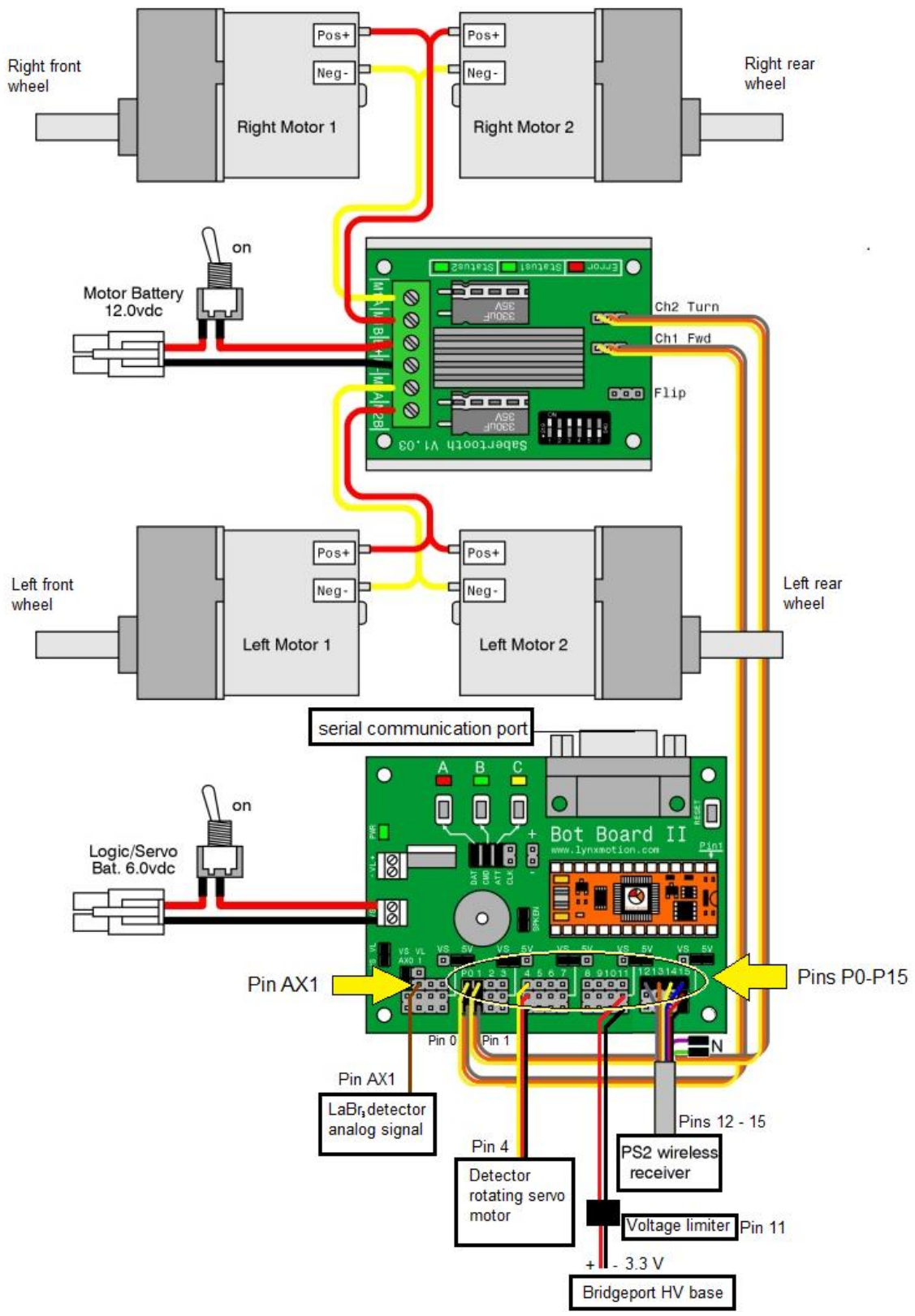


Figure 13: Schematic of robot's control system [26]

The robot is designed to operate in following three modes:

1. Sweep Scan Mode with Count Rate Measurements: This is used to scan a plane with the robot's detector to measure the direction of local gamma ray sources as well as record a visual panorama of the area (see Section 2.4).
2. Sweep Scan Mode with Energy Spectra: Sweep scan mode can also be performed with a MCA for energy spectra measurements to identify both the energy and direction of local gamma ray sources (see Section 2.6).
3. Autonomous source seek mode: This is used to search the local area for gamma ray sources in the area around the robot (see Section 2.7).

The robot is maneuvered directly by a human operator from a wireless controller pad shown in Figure 14. The wheels are controlled by the directional joystick on the controller. The secondary directional joystick on the controller allows the robot's radiation detector to be rotated and alter the direction of the gamma ray measurement or the viewing direction of the mounted camera. The circle button centers the detector in the forward direction of the robot. Pressing the triangle button gives a single measurement from the detector in the current direction. Pressing the cross button instructs the robot to take a 180° forward direction panorama measurement (sweep scan mode). Pressing the select button on the controller instructs the robot to begin the autonomous source seek mode.

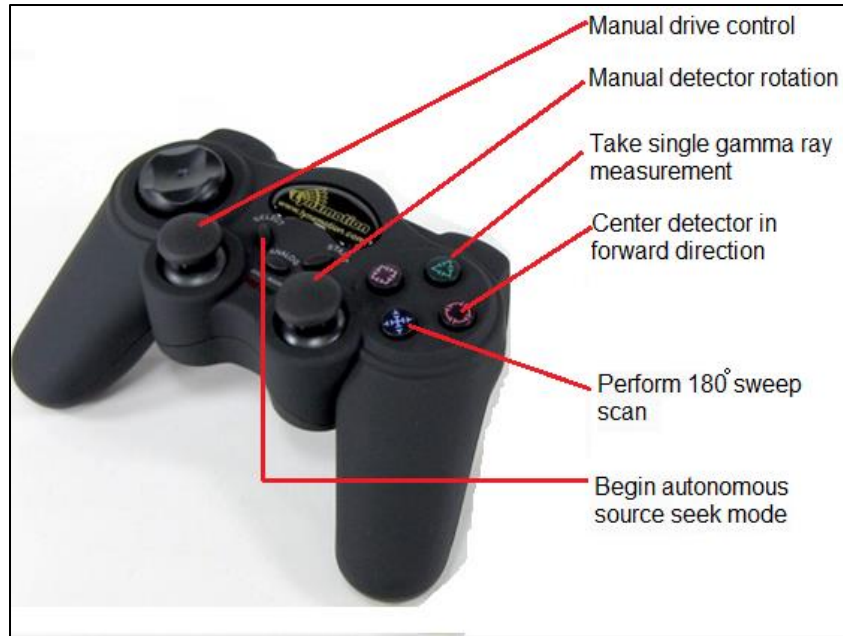


Figure 14: Robot's wireless control pad

2.3 Gamma Ray Detection System

2.3.1 LaBr₃ Scintillator Detector

The detector used in this prototype is a cylindrical 1.5 inch by 1.5inch (3.81 cm diameter and 3.81 cm height) LaBr₃:Ce scintillation detector mounted on a Saint-Gobain 2 inch diameter Hamamatsu R6231 photomultiplier tube. A comprehensive review of this detector and comparison to NaI detectors is presented by Milbrath et al [1]. The LaBr₃ detector and PMT are connected to a Bridgeport HV base which provides high voltage for the PMT from the robot's NiMH battery.

2.3.2 Digital Gamma Ray Measurement: Count Rate Measurements

The analog output signal of the photomultiplier tube is fed directly into the analogue input Pin AX0 of the Botboard 2 (shown in Figure 13). The atom processor reads the input signal as a voltage between zero and five volts. The onboard analogue to digital converter (ADC) translates the voltage into a 10 bit integer between 0 and 1023 with zero corresponding to 0 V input and 1023 corresponding to 5 V. 64 readings are taken consecutively and the sum is given as a value between 0 and 65472. The value is stored on the atom processor as a 16 bit integer that is accessible by the robot's software. The readings taken from the analog input of the LaBr₃ detector are performed in current mode and are not sensitive to the energy of the incoming radiation. This is a measurement of the total current produced in the PMT of the detector during the measurement interval, and thus only counts of the total number incoming gamma rays. In the robot control software individual measurements are repeated and summed over an adjustable measurement period and give a time averaged count rate over the desired time interval. Longer measurements give more accurate average count rates but take more time to complete. In this thesis most measurements were done by summing 15,000 individual readings in each directional measurement. The individual readings take approximately 0.8 ms to acquire, so the total time to take one directional measurement was approximately 12 seconds. When the robot is performing a sweep scan, the detector is set to a specific direction and a measurement is taken. The signal from the LaBr₃ detector is recorded as a 16 bit word and the angle is stored as a 10 bit integer.

2.3.3 Energy Spectra Measurements

The Bridgeport HV base has general purpose input/output (GPIO) pins that can be connected directly to Bridgeport's data acquisition system (DAQ). The DAQ is a four channel data

acquisition system that includes a digital MCA. Raw data from the DAQ system is sent via USB to a computer. The LaBr₃ detector on our prototype mobile robot is connected to one of the four input channels of the DAQ and a laptop with the IgorPro software package is used to record energy spectra. The software program includes a graphic user interface (GUI) for controlling and adjusting the energy spectra acquisition parameters.

2.4 Sweep Scan Measurements: Count Rate Mode

In this mode individual detector measurements are taken in an adjustable number of steps starting from the right direction of the robot (defined as 0°) and increasing in the specified step size all the way to the left direction of the robot (180°). The number of steps as well as the total sweep angle can be adjusted in the robot's software. The step size determines the angular resolution of the directional profile and the total sweep angle determines the total field of view of the measurement. Increasing the number of steps produces a finer angular resolution, but takes more time to complete the total scan. In the experiments performed in this thesis the total sweep angle used was generally 180° and the step sizes were typically 5° or 4.5° each. A schematic of the sweep scan mode is shown in Figure 15. After the scan is complete the detector points in the direction of the highest recorded gamma ray signal, indicating to the human operator that the highest intensity of gamma rays is coming from a location in the center of the field of view of the camera.

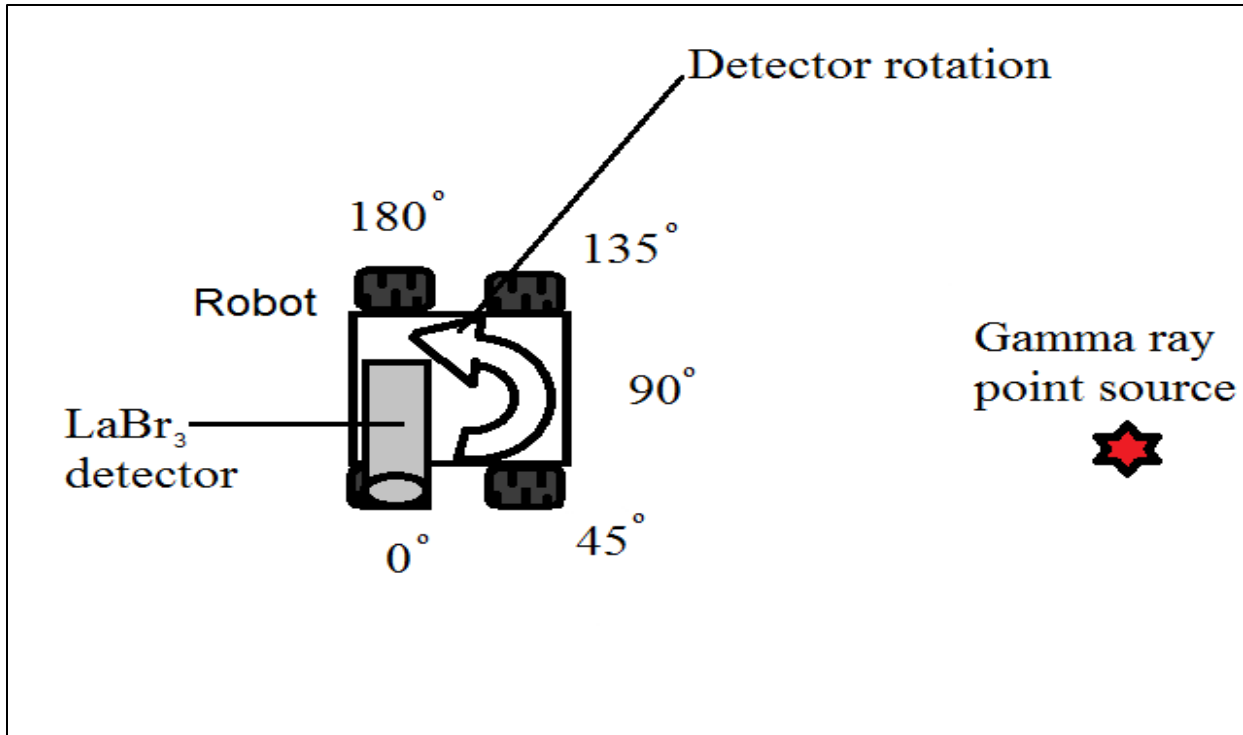


Figure 15: Schematic of robot's 180° sweep scan mode. The detector and camera begin facing the right side of the robot. Radiation measurements are taken by the detector and photos are taken by the camera. The detector and camera are rotated toward the left side of the robot in an adjustable number of steps. After the scan is complete the detector and camera will turn toward the gamma ray point source.

2.5 Radiation Data Visual Overlay

The radiation measurement data is intended to be combined with a visual panorama of the area surrounding the robot so a camera is mounted on top of the detector. A photo is taken at each measurement angle and an 180° composite panorama is constructed from the photos using the GNU Image Manipulation Program (GIMP). The radiation measurements are saved in a directional profile and plotted on a graph with the detector angle along the horizontal axis and the detector signal on the vertical axis. The directional profile graph is overlaid on top of the visual panorama so that the angle measurements of the gamma ray directional profile correspond

to the horizontal pixel row of the panorama at the appropriate angle. The vertical axis is scaled so that all data points fit onto the picture.

2.6 Sweep Scan Measurements with MCA for Energy Spectra

2.6.1 Directional Profiles with Energy Spectra

In this mode sweep scan measurements are performed exactly as described in Section 2.4 except gamma ray energy spectra are measured in each direction instead of count rate. When the full 180° scan is complete the energy spectra from each direction are compiled into a 2D count frequency histogram with the detector angle along the x-axis and the incident gamma ray energy along the y-axis. The frequency (number of counts) for each MCA energy bin at each detector angle is represented along the z-axis of the graph. This produces a map in which individual peaks represent the energy and direction of incoming gamma rays. Thus, the location of gamma sources may be determined as well as the identification of the radioactive isotopes present in the scanned area.

2.6.2 Rapid Scan Directional Profiles with Energy Spectra

The rapid scan mode is designed to quickly locate a single point source and decrease the time required to perform a full 180° sweep scan. In this mode 5 individual spectra are measured in the forward direction of the robot at 0°, 45°, 90°, 135° and 180°, respectively. The direction with the single highest count in the total spectra is designated as the direction of interest. A 90° sweep

scan (as described in section 2.6.1) with steps of 4.5° is then performed around the direction of interest (-45° to $+45^\circ$) with the direction of interest centered in the middle of the sweep scan. This provides a finer resolution sweep scan in all directions near the point source and eliminates the need to perform many measurements in directions far away from the source. Figure 16 shows a schematic and the setup of the first stage of the rapid scan mode. The 5 measurement positions are indicated by white arrows. In the example shown in Figure 16 the region of interest will be at 90° since the source is closest to that direction. The fine sweep scan will then be performed in the region from 45° to 135° .

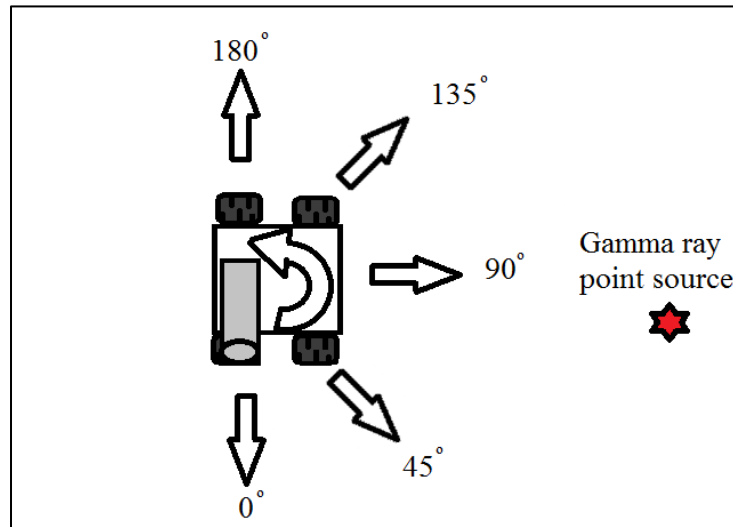


Figure 16: Schematic of robot's rapid sweep scan mode. The first five measurement directions are indicated by white arrows.

2.7 Autonomous Source Seek Mode Operation

In this mode the robot attempts to determine the location of the strongest gamma ray source in the local area as measured from the robot's current position. The robot begins by taking a single count rate measurement with the detector in the forward position and then rotating the whole

body 45° via the differential drive wheels. It takes seven additional count rate measurements and rotates until it has returned to the original direction as shown in Figure 17. This allows the robot to measure 8 directions around the original position. The rotation of the body is necessary since the detector is only capable of rotating 180° in the forward direction of the robot. After measuring the 8 directions shown in Figure 17, the robot will turn and center the forward direction of the body in the direction of the highest recorded measurement. A forward drive step can be adjusted in the robot's software so that the robot will drive a specified distance toward this measured direction before beginning the next phase. The robot will then begin a second measurement by performing an 180° degree sweep scan of the forward direction. This sweep is done in nine individual measurements each separated by 22.5° and upon completion the robot again turns to face the forward direction of the robot body to the direction of highest recorded gamma ray intensity as shown in Figure 18. Now the point source gamma emitter should be located in a direction close to the forward direction of the robot. A final fine sweep scan is done in the forward 90° field of view of the robot, starting at 45° degrees to the right of the forward direction and ending at 45° degrees to the left of the forward direction (shown in Figure 19). After the scan is complete the robot will point the detector toward the direction of the highest recorded gamma ray intensity and make a beeping sound indicating to the user that the gamma ray source should be located near the center of the field of view of the onboard camera.

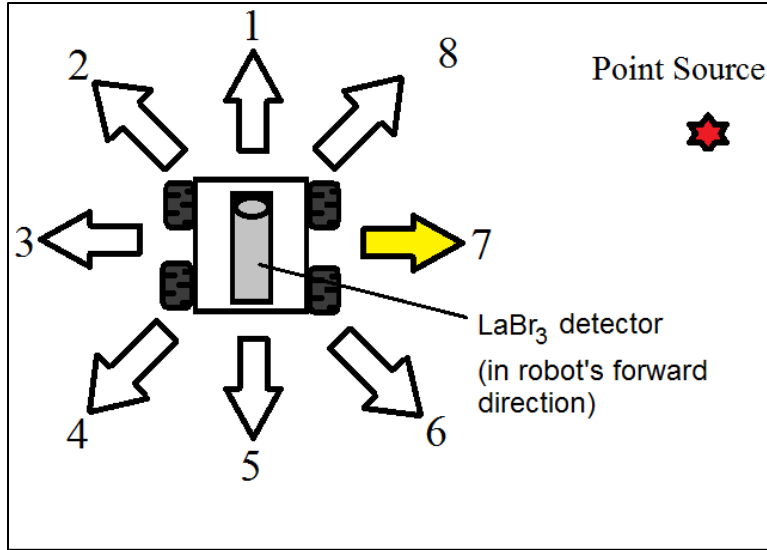


Figure 17: Rotational stage in source seek mode. The 8 measurement directions are indicated by arrows in the figure. The detector remains in the forward direction of the robot. The wheels are turned to turn the robot body and orient the detector to the 8 measurement directions.

In the example shown in Figure 17 the highest gamma ray measurement occurs at step 7. The robot will then turn the body 90° to the right and proceed to the sweep scan shown in Figure 18. In the case illustrated in Figure 18, the highest gamma ray measurement occurs in step 14. The final fine sweep scan region is represented in Figure 19 as a shaded region. The final detector and camera direction is shown in Figure 20. Ideally the robot points directly at the source.

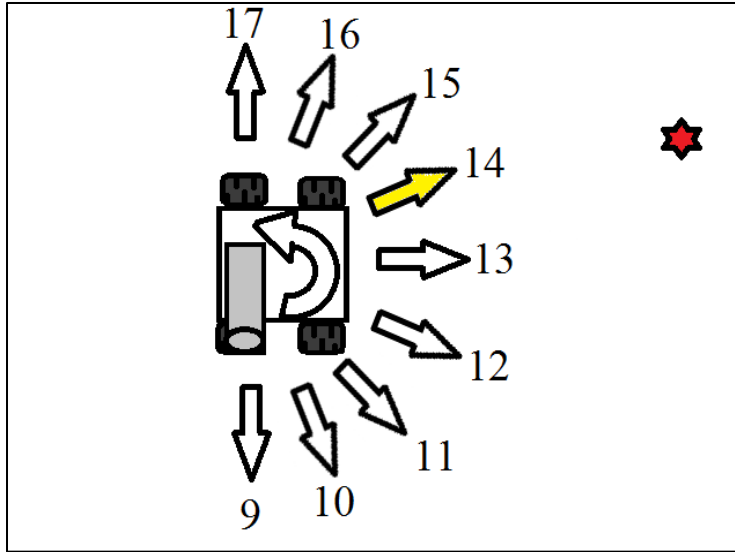


Figure 18: Nine direction sweep scan in source seek mode. The robot has turned 90° after completing the measurements illustrated in Figure 17. The measurement directions here are shown as arrows. The measurement at step 14 will produce the highest gamma count rate so the robot will turn to face this direction.

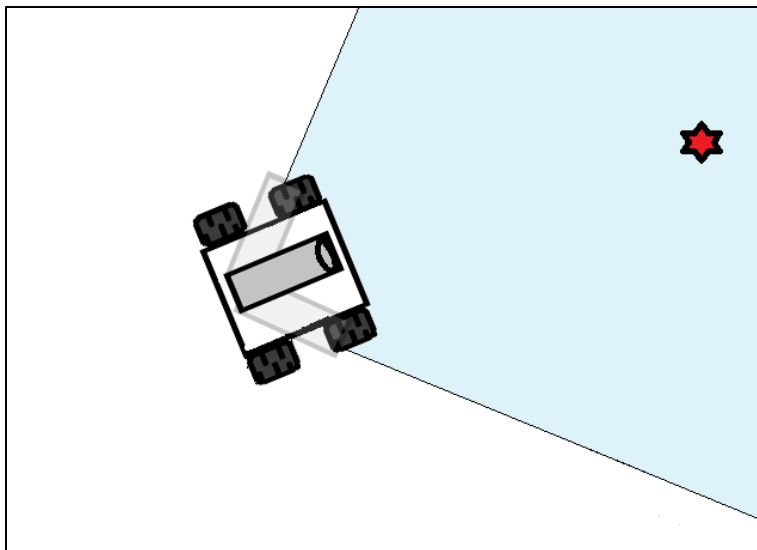


Figure 19: Forward direction 90° fine sweep in source seek mode. In this stage the robot will perform a 90° sweep scan (the shaded region) in an adjustable number of steps in order to determine the gamma ray source position.

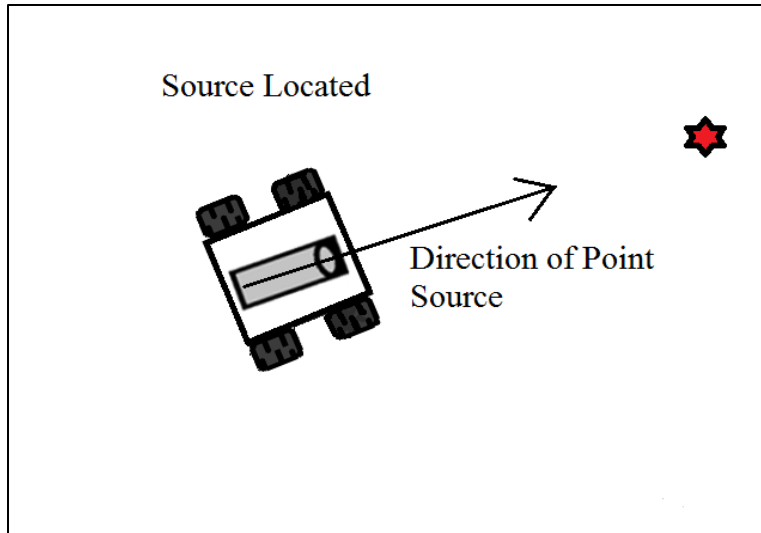


Figure 20: Final localization of source in source seek mode. After the source seek mode is complete, the detector and camera will be pointed toward the gamma ray source. The source should appear in the center of the camera's field of view.

2.8 Experimental Setup

Several series of experiments were designed and performed to test the method developed in this thesis. The prototype mobile robot described in this section was used in all experiments carried out at the UOIT radiation facilities. The robot has been observed while operating in the three modes described in Sections 2.4 – 2.7 and relevant data has been recorded.

2.8.1 Equipment and Gamma Ray Sources

The following is an annotated list of relevant equipment used the experimental work performed in this thesis.

- Prototype mobile robot : See Section 2.2
- Johnson Self-Adjusting Laser Level Kit: This was used in tandem with a tape measure to measure the robot and source position and direction in the lab. Whenever necessary, it was also used to align the robot and gamma sources into desired positions.
- Retort stand: This was used to hold gamma sources in position.
- Glass aquarium: This was used to contain a pile of radioactive rocks.
- Bridgeport's MCA DAQ system: This was used to record all spectra measurements (see Section 2.3.3).
- Laptop Computer: This was used to record all count rate data, energy spectra, visual panoramas and directional data measured in all experiments.

The following is an annotated list of gamma ray sources used.

- **(2x) Sealed Caesium-137 solid sources (Stuart Hunt & Associates Ltd.):** These two sources are each labeled with an activity of 1.0 mCi (3.7×10^7 Bq). The sources are a 25.4 mm x 5 mm solid disc that resides inside a lead pig that can be opened.
- **Sealed Barium-133 solid source (Stuart Hunt & Associates Ltd.):** This source is labeled with an activity of 0.5 mCi (1.85×10^7 Bq) \pm 15%. The source is a 25.4 mm x 5 mm solid disc that resides inside a lead pig that can be opened.
- **Sealed Cobalt-60 solid source (Stuart Hunt & Associates Ltd.):** This source is labeled with an activity of 0.5 mCi (1.85×10^7 Bq) \pm 15%. The source is a 25.4 mm x 5 mm solid disc that resides inside a lead pig that can be opened.
- **(7x) SPECTECH calibrated RSS-5 source kits:** Each of these source kits contains five sealed plastic disc sources. The sources are in the form of 1 inch (2.54 cm) diameter and $\frac{1}{8}$ inch (3.175 mm) height cylindrical plastic “buttons”. The five button sources each contain a different radioactive material that is sealed at the centre. The isotopes present in the five button sources are as follows: ^{137}Cs , ^{60}Co , ^{204}Tl , ^{90}Sr , and ^{210}Po . The activity of the ^{137}Cs sources are labeled as: 5.0 μCi (from date of manufacture) and the ^{60}Co sources are labeled as 1.0 μCi . The ^{210}Po and ^{90}Sr sources are both labeled as 0.1 μCi and the ^{204}Tl sources are 1.0 μCi . Due to radioactive decay, these sources have an activity that is less than the activity at the date of manufacture which is listed as November 2004 on all sources in all seven kits except the ^{210}Po sources which were all manufactured in October 2011. The activity of each source at the time of the experiments performed in this thesis is listed in Table 3 in Appendix C [27].

- **(2x) SPECTECH calibrated RSS-8 source kit:** Each of these source kits contains eight sealed plastic disc sources in the form of 1 inch (2.54 cm) diameter and $\frac{1}{8}$ inch (3.175 mm) height cylindrical plastic “buttons”. The isotopes present in the eight button sources are as follows: ^{137}Cs , ^{60}Co , ^{57}Co , ^{54}Mn , ^{22}Na , ^{109}Cd , ^{133}Ba , and a disk labeled as “unknown” containing both ^{137}Cs and ^{65}Zn . The activity of all button sources is labeled as 1.0 μCi (from date of manufacture) except the “unknown” source where the activity of the ^{137}Cs is 0.5 μCi and the ^{65}Zn is 1.0 μCi . Due to radioactive decay, these sources have an activity that is less than the activity at the date of manufacture which is listed as June 2005 on all sources in both kits. The activity of each source at the time of the experiments performed in this thesis is listed in Table 3 in Appendix C [27].

2.8.2 Directional Profile and Visual Panorama – Sweep Scan Mode with Count Rate Measurements

Single Point Source

A series of experiments were performed to observe the ability of the robot to locate a point source of gamma radiation using the sweep scan mode with count rate measurements described in Section 2.4. A 180° field of view and steps of 5° were used for these measurements. Figure 21 shows the setup of the experiment. A single 1 mCi ^{137}Cs (3.7×10^7 Bq) source was placed in the forward direction of the robot (90° relative to the right side of the robot) at a distance of 2m. The source was placed on top of a box with a height of 25 cm in order to align the height of the source with the height of the robot’s detector. The source’s lead pig was opened and a sweep scan measurement was performed. The experiment was repeated with the ^{137}Cs source and box

located at 60° , 30° , and 0° relative to the right side of the robot. The sweep scan data was recorded for all four source positions. A photo of the robot performing a sweep scan in one of these experiments is shown in Figure 22. The ^{137}Cs source was removed from the lab and objects were placed at all four source positions and another sweep scan measurement was recorded. This scan had no gamma sources present thus provides a radiation background measurement of the local area. The camera also recorded a visual panorama of the area during this sweep scan to give a representative picture with all four source positions. The radiation background sweep scan was repeated three times so that a total of three background measurements were recorded.

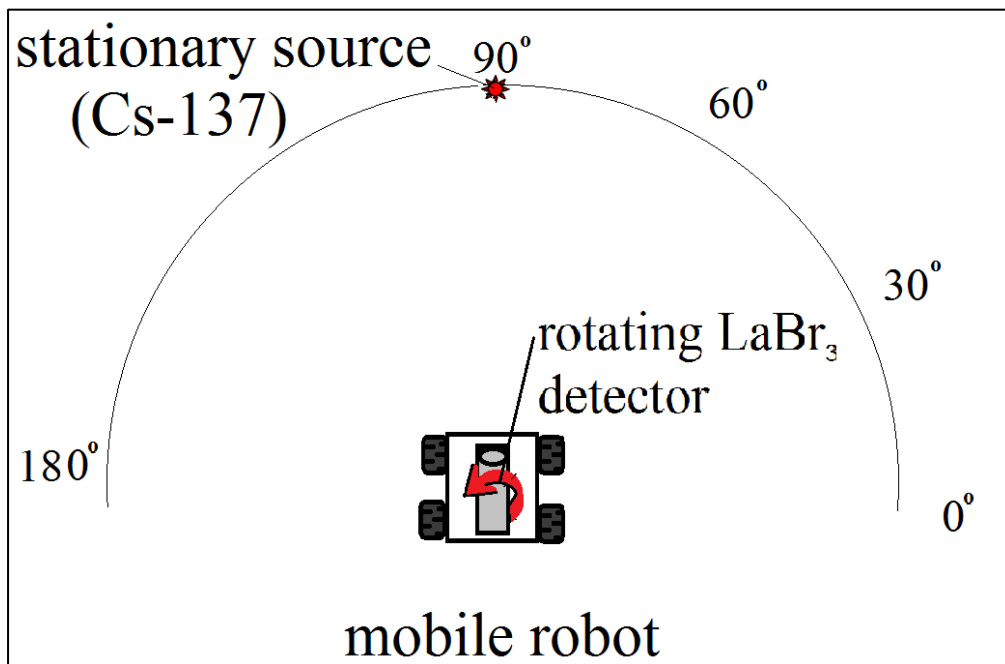


Figure 21: Diagram of sweep scan measurements with a ^{137}Cs source at 90° . The four source positions used in these measurements are indicated on the figure.

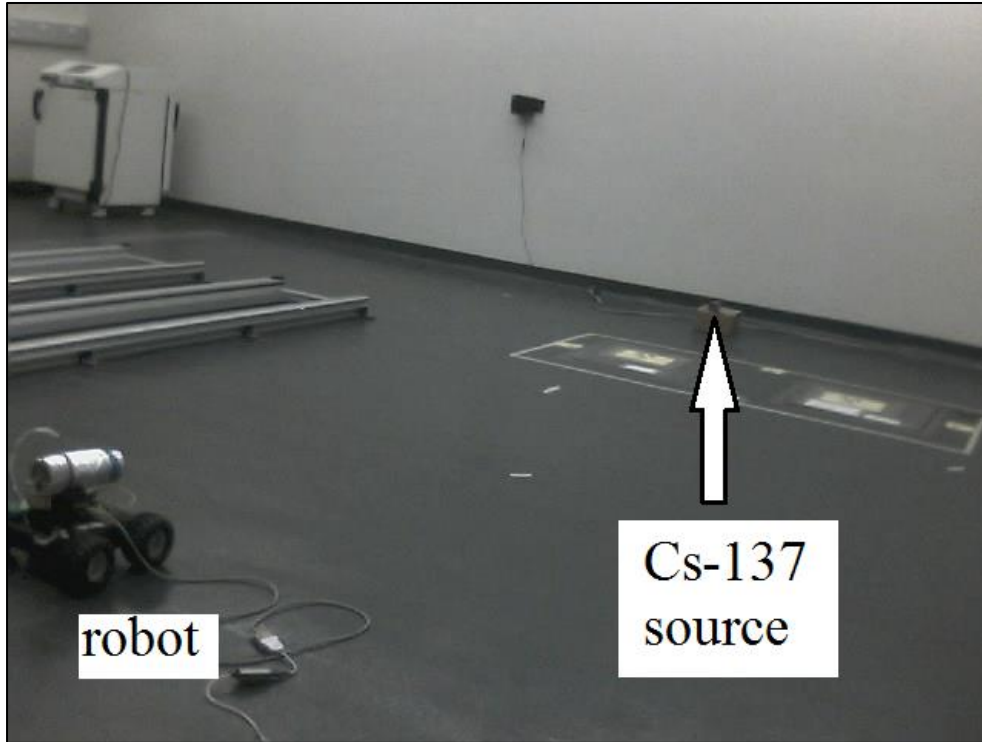


Figure 22: Photo of sweep scan experiment setup with a 1mCi ^{137}Cs source at 90°

Multiple Point Sources

Another series of experiments were conducted to test the capability of the prototype to distinguish between two point sources of gamma radiation using a single sweep scan with count rate measurements. The experiments were conducted exactly the same as the experiments described in the above section, except two identical 1 mCi ^{137}Cs sources were placed at 60° and 120° , relative to the robot position, at the same time. These sources were both placed directly on the floor. A schematic of this experiment setup is shown in Figure 23.

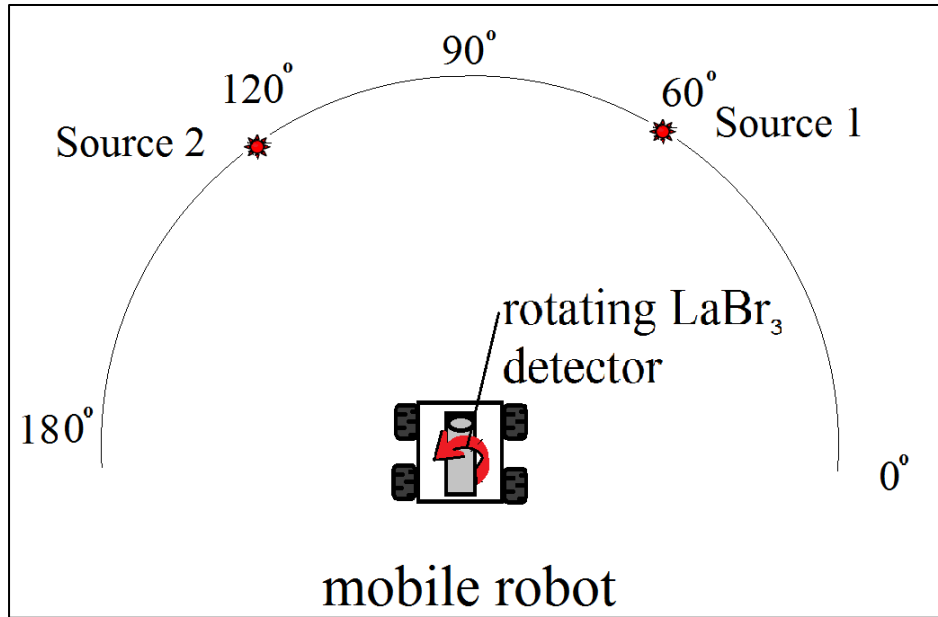


Figure 23: Diagram of sweep scan measurements with two sources of 1 mCi ^{137}Cs at 60° and 120°

Distributed Natural Mixed Alpha Beta and Gamma Source

The third series of experiments was performed to observe the directional gamma profile produced when a distributed, mixed natural radiation source is measured. In this case the robot was placed approximately 30 cm away from an aquarium filled with rocks known to be radioactive due to thorium and uranium decay chains [28]. The experimental setup is shown in

Figure 24. A 180° sweep scan with count rate measurements was performed in steps of 4.5° . A photo of the experimental setup is shown in Figure 25. Another 180° sweep scan was measured in a separate room with no radiation sources present. This was done to give a representative ambient radiation background sweep scan measurement.

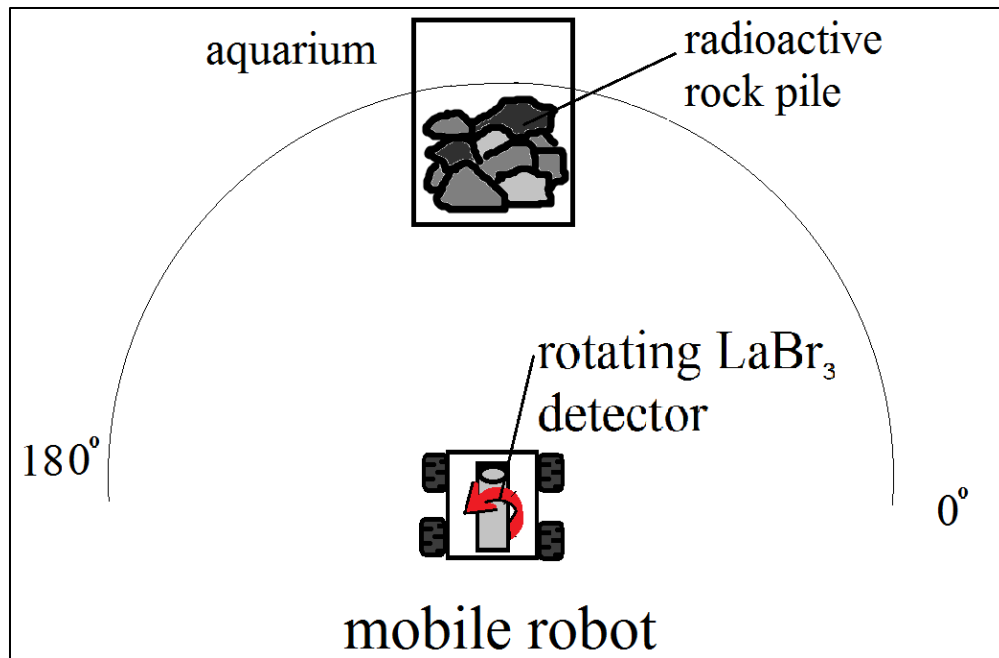


Figure 24: Diagram of sweep scan measurements with natural rock source

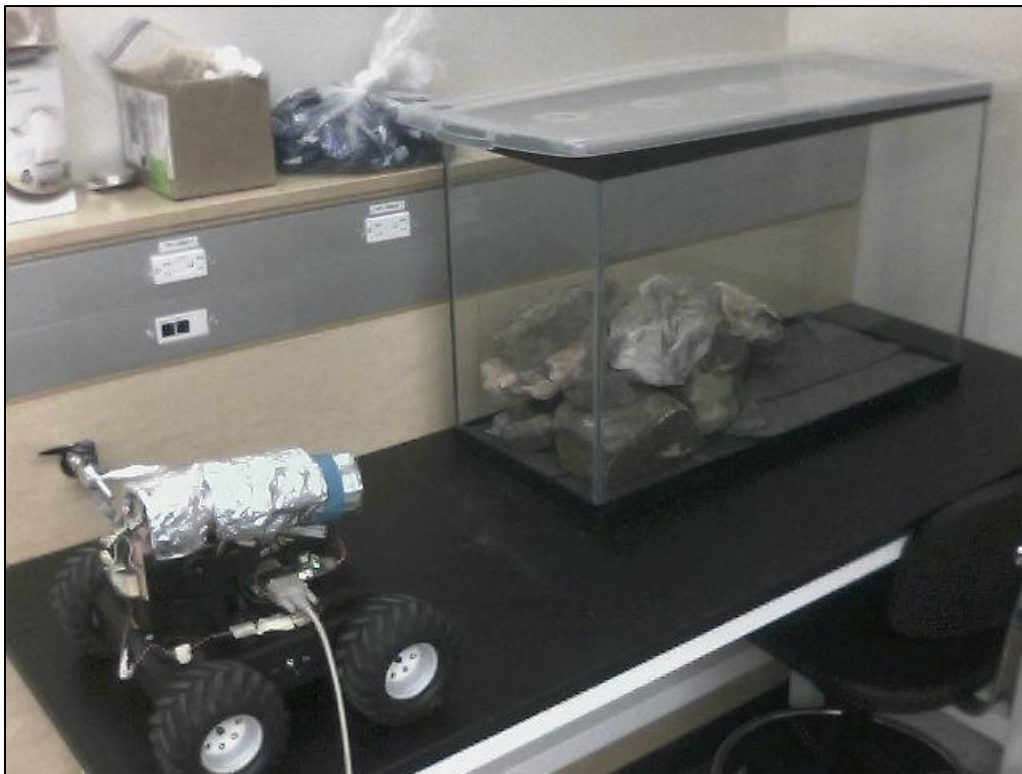


Figure 25: Experimental setup of natural rock source measurement

2.8.3 Directional profile and Visual Panorama – Sweep Scan Mode with Energy Spectra

Another series of experiments was performed to determine the effectiveness of the sweep scan mode with the addition of a MCA for the purpose of identifying both the location and energy spectra of nearby gamma ray sources. This was done by connecting the robot's detector to the MCA data acquisition system described in Section 2.3.3. Before beginning directional profile measurements, a three point energy calibration spectra was recorded to determine a linear equation to convert spectra channel number into gamma ray energy. A 4.1 μCi (1.52×10^5 Bq) ^{137}Cs button source and a 0.32 μCi (11800 Bq) ^{60}Co button source (from an Rss-5 source kit) were placed directly onto the LaBr_3 detector and a 10 minute energy spectrum was acquired. The resulting calibration spectrum is shown in Figure 48 (Section 3.2). After obtaining an energy calibration, experiments were performed in sweep scan mode with energy spectra measurements. A single 28.7 μCi (1.1×10^6 Bq) ^{137}Cs source was constructed by stacking seven ^{137}Cs button sources together from the RSS-5 source kits. This source was placed on top of a box (height 20 cm) directly in front of the robot (90°) at a distance of 150 cm. In addition to the ^{137}Cs source, a single 2.2 μCi (81400 Bq) ^{60}Co was also constructed by stacking seven ^{60}Co button sources together from the RSS-5 source kits. This was placed in a retort stand so that the source would reside at an angle of 45° and distance of 25 cm away from the robot at a height of 21 cm (directly in the middle of the robot's LaBr_3 detector) . 180° sweep scans in step angles of 4.5° were performed and an energy spectrum was measured at each position. Two minute spectrum measurements were acquired in each direction in order to obtain significant counting statistics for the low activity sources used. A 2D count frequency histogram (described in section 2.6.1) of the spectra and direction data was plotted in MATLAB. A 1D Gaussian filter was used to smooth

the histogram data along the x-axis (angle measurements) [29]. This allowed for a proper estimation of the centroid of the directional measurement peaks without disturbing the energy spectra plotted along the y-axis. Directional gamma ray profiles for the energies corresponding to ^{137}Cs and ^{60}Co were extracted from the 2D count frequency histogram. These gamma ray directional profiles were plotted and overlaid on top of the visual panorama recorded by the robot's camera. A layout of this experimental setup is shown in Figure 26 and a photograph of the experimental setup is shown in Figure 27.

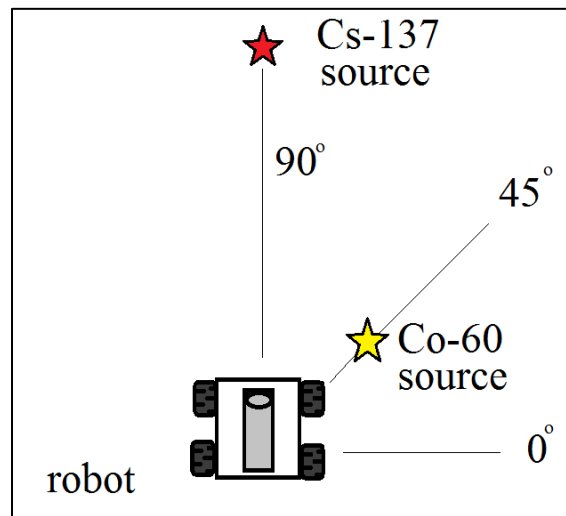


Figure 26: Experimental setup of directional profile with energy spectra measurement with $28.7\mu\text{Ci } ^{137}\text{Cs}$ and $2.2\mu\text{Ci } ^{60}\text{Co}$ sources

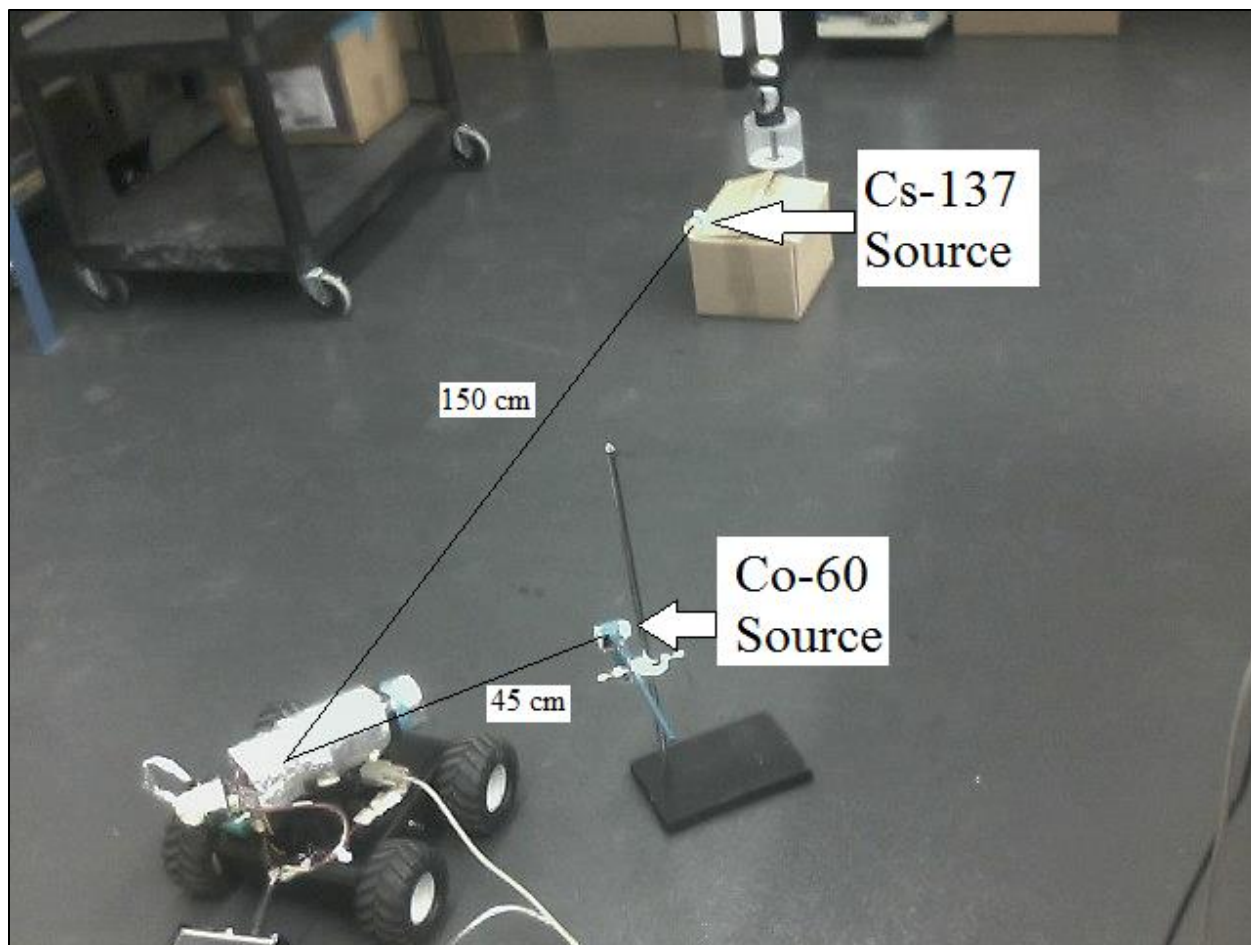


Figure 27: Photo of the Experiment with $28.7 \mu\text{Ci } ^{137}\text{Cs}$ and $2.2 \mu\text{Ci } ^{60}\text{Co}$ sources

2.8.4 Rapid Scan Directional Profile and Visual Panorama with Energy Spectra

Another series of experiments was performed with the MCA to observe the effectiveness of the rapid scan directional and spectral profile method. In these experiments a single source was placed at an arbitrary position near the forward direction of the robot at a distance of approximately 150 cm. The spectra were obtained from the rapid scan sequence described in Section 2.6.2 and the direction of interest was determined. Using the direction of interest, a 90° sweep scan was performed in steps of 4.5° starting from 45° to the right side of the direction of interest and ending at 45° to the left side. A 180° visual panorama of the local area was also

recorded with the onboard camera. 30 second energy spectrum measurements were acquired in each direction to obtain reasonable counting statistics in a relatively short period of time. A 2D count frequency histogram (described in section 2.6.1) of the energy spectra and direction data for the 90° sweep scan was plotted in MATLAB. A 1D Gaussian filter was used to smooth the histogram data along the x-axis (angle measurements). This experiment was first performed with a 500 μCi (1.85×10^7 Bq) ^{133}Ba source placed directly on the floor. The experiment was repeated, except a 500 μCi (1.85×10^7 Bq) ^{60}Co source used instead of ^{133}Ba . In both experiments the robot position was identical. Figure 28 shows a layout of the robot and source position in this experiment. Figure 29 shows a picture of the ^{133}Ba source captured from the robot's onboard camera. The gamma ray directional profiles from the peak energy channels were extracted from the smoothed 2D frequency data. The gamma ray directional profile for the 356 keV peak of ^{133}Ba was overlaid on top of the visual panorama captured by the camera.

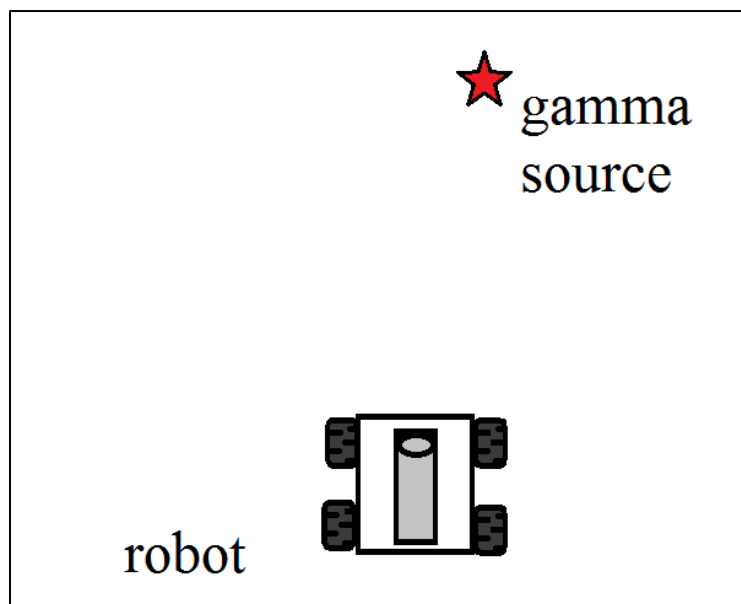


Figure 28: Schematic of a rapid scan experiment

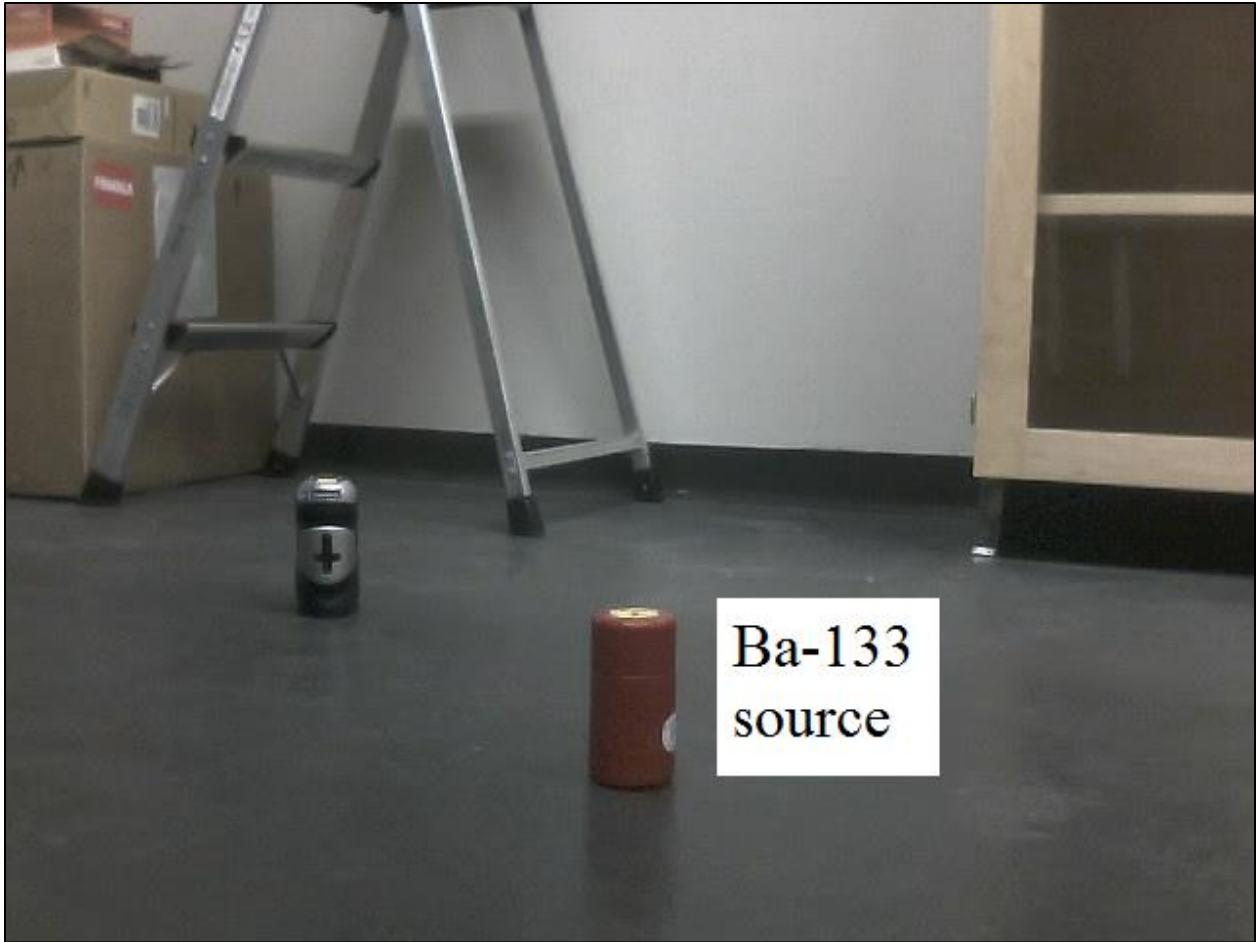


Figure 29: Photo of 500 μCi ^{133}Ba source used in rapid scan experiment

2.8.5 Point Source Triangulation Experiments

A series of experiments was performed to test the ability of the robot to locate the actual position of a point source in a horizontal plane using the principles of triangulation (Section 1.7). A two dimensional coordinate system (with x and y axis) was plotted on the floor of the applied radiation laboratory at UOIT, and key points were marked (see Figure 30). A mixed 28.7 μCi ^{137}Cs and 2.2 μCi ^{60}Co source (total activity: 1.14×10^6 Bq) was constructed by assembling seven ^{137}Cs and seven ^{60}Co button sources (from the RSS-5 source kits) into a single horizontal stack. The source stack was placed vertically at the (50 cm, 50 cm) position of the coordinate system on

top of a lead brick with a height of 10 cm to bring the height of the source close to the height of the robot's detector. The stacked source can be seen in the right side picture of Figure 31. A cardboard box was placed at an arbitrary orientation to obscure the visual identification of the source. This serves to simulate a situation in which the robot operator cannot visually identify the position of the gamma source even if directional information of the source is given. So the source cannot be visually identified by the robot operator from a single sweep scan. The robot performed 180° sweep scans with count rate measurements in steps of 4.5° (see Section 2.4). These sweep scans were performed at four different positions in the coordinate system with the robot body oriented in the +y axis direction. The center of the robot's detector rotation axis was used as the robot's reference position. The 180° sweep scans were performed at the following positions (0, 0), (0, 30), (0, 60) and (0, 90) where the units of the coordinate system are in cm. At each position, the direction of the gamma source was determined by the robot using the sweep scan mode described in Section 2.4. The equation of the lines connecting the robot positions to the sources position was calculated in MATLAB using the method described in Section 1.7. The linear equations were arranged in matrix form and the ordinary least squares solution for the source position was obtained. Figure 30 shows a map of the setup of this experiment. Figure 31 shows a view of the box from the robot's onboard camera at (0,0) position. The right side of the figure shows the same view where the walls of the box are semitransparent, revealing the position of the source inside the box.

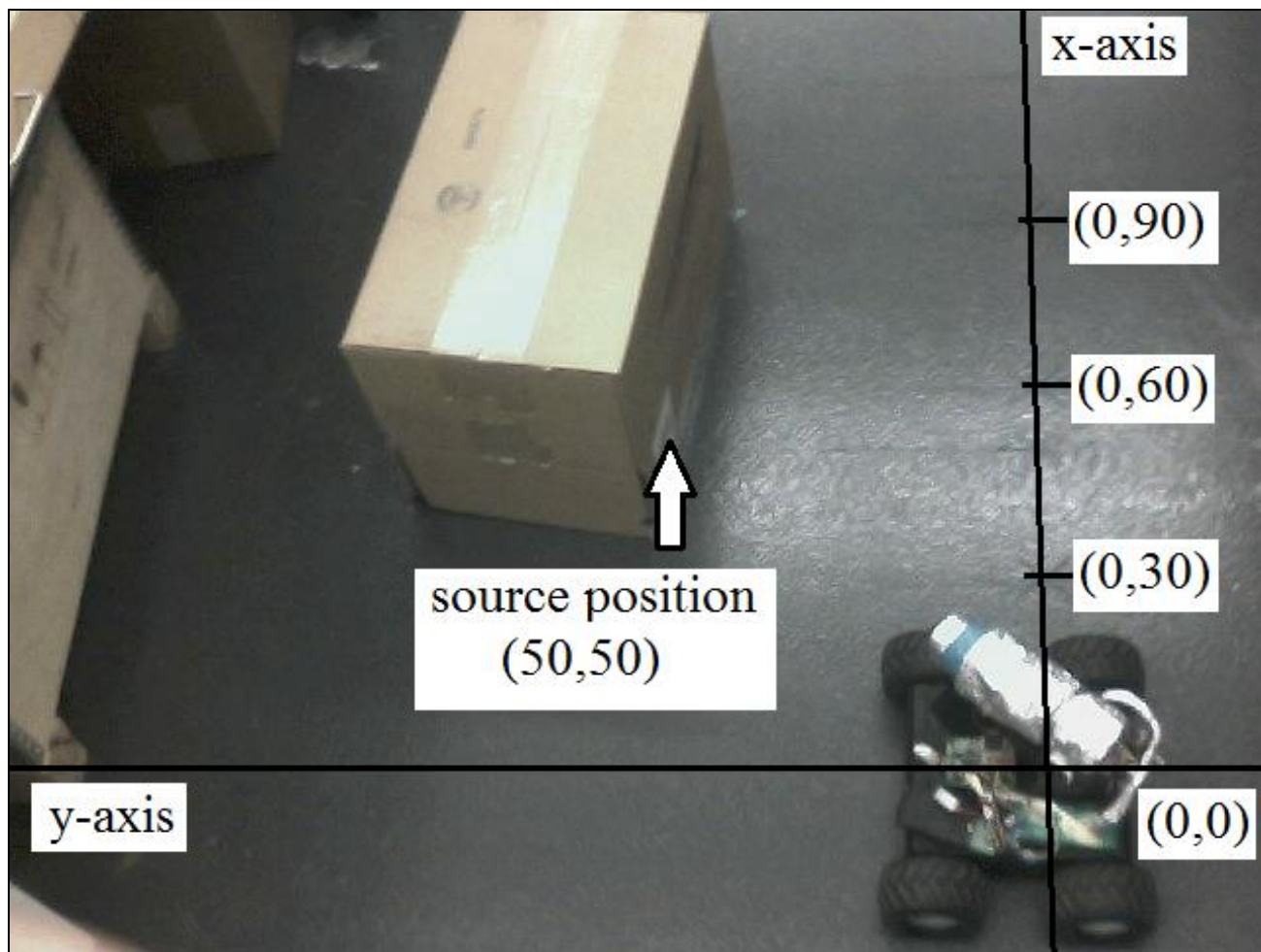


Figure 30: Setup of source position triangulation experiment



Figure 31: View of box and internal view of box revealing internal gamma source

2.8.6 Autonomous Source Seek Mode

Source Seek Mode

The autonomous source seek mode of the prototype mobile robot was tested extensively. The first series of experiments involved placing a 1 mCi (3.7×10^7 Bq) ^{137}Cs directly on the floor in the middle of a room. The robot was placed at a random direction and orientation from the source at a distance between 1 m and 2 m and the autonomous source seek mode was activated. In these experiments no forward drive movements were used between the scan stages so the robot would remain in the same position for the whole sequence. The gamma ray measurement for each of the steps was transferred from the robot's processor to a laptop computer via serial cable. Figure 32 shows a photograph of the setup of these experiments.

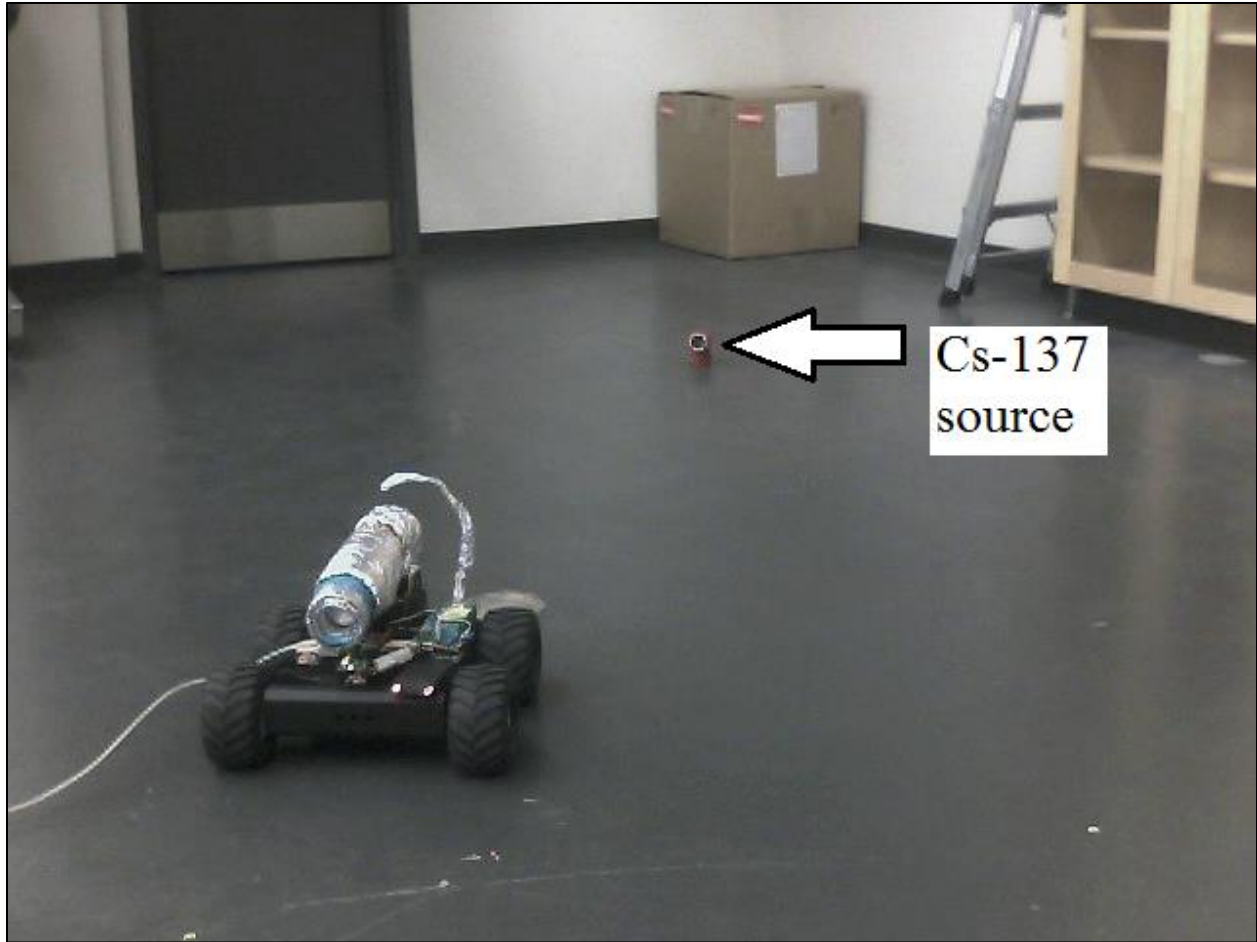


Figure 32: Setup of source seek mode experiment

Source Seek Mode with Hidden Source

Another series of experiments was performed to test the ability of the robot to locate hidden sources using the autonomous source seek mode. In these experiments two $2.17 \mu\text{Ci}$ (80100 Bq) mixed button source of ^{137}Cs , ^{60}Co , ^{58}Co , ^{133}Ba and ^{22}Na were constructed by stacking five button sources from the RSS-8 kits. These sources were placed adjacent to each other behind a flap on top of a cardboard box with a height of about 17 cm. The robot was placed at an arbitrary position and orientation at a distance between 1 m and 2 m away from the source. The autonomous source seek mode was activated and the robot was allowed to search for the source.

In these experiments a 10 cm forward drive step was used so that the robot would taxi slightly towards the source between each of the scan sequences. A video of the source seeking mode was recorded from the detector mounted camera on the robot. A diagram of the experimental setup is shown in Figure 33. A photo of cardboard box and hidden gamma ray sources are shown in Figures 34 and 35.

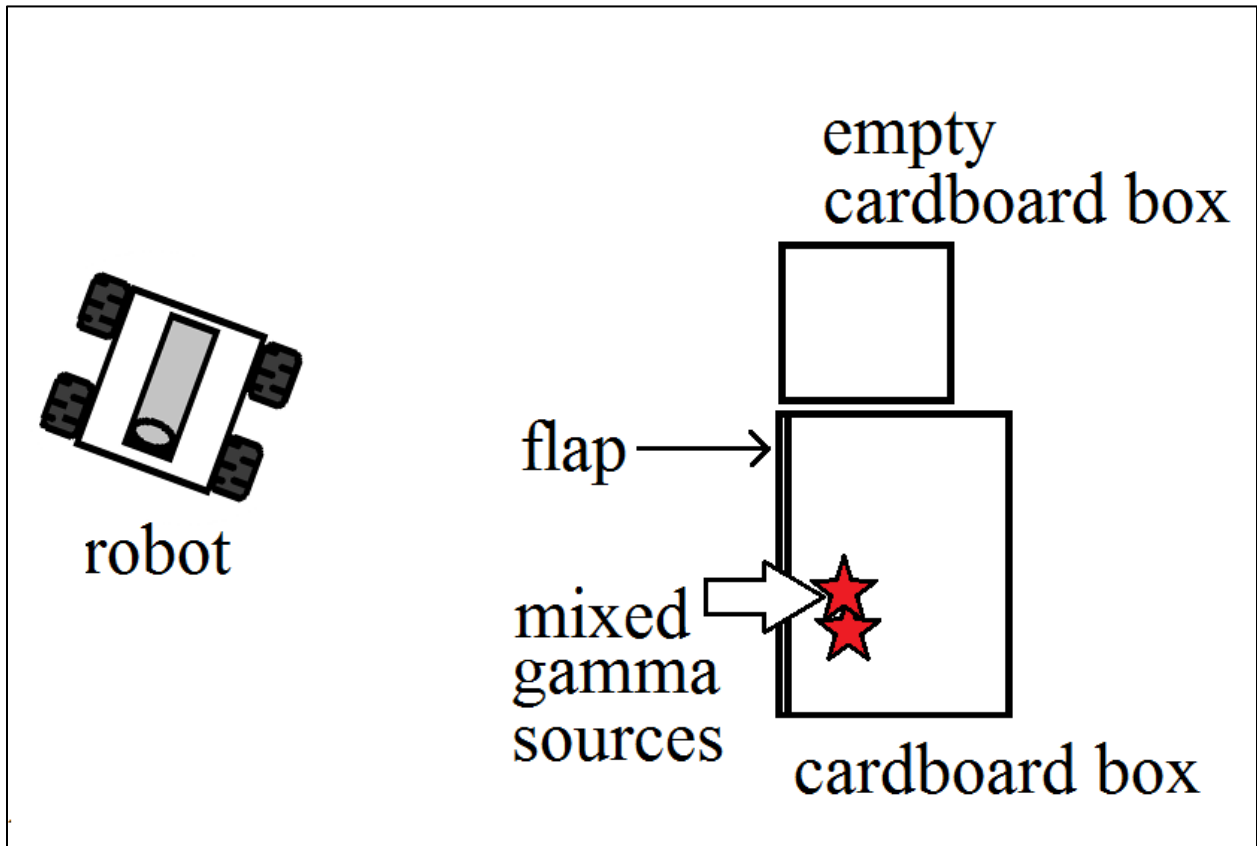


Figure 33: Setup of source seek mode experiment with hidden sources

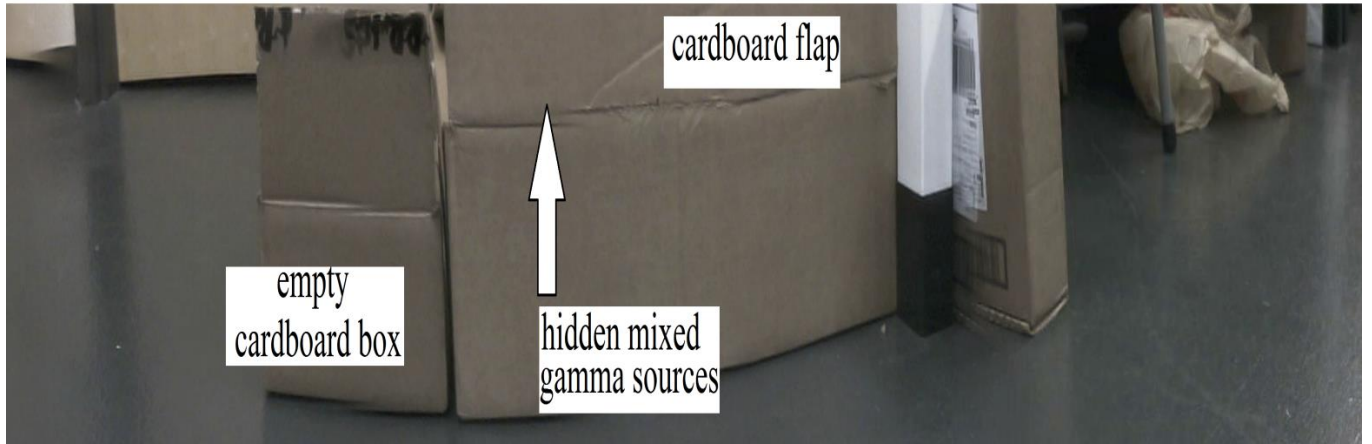


Figure 34: Source seek mode experiment with hidden sources

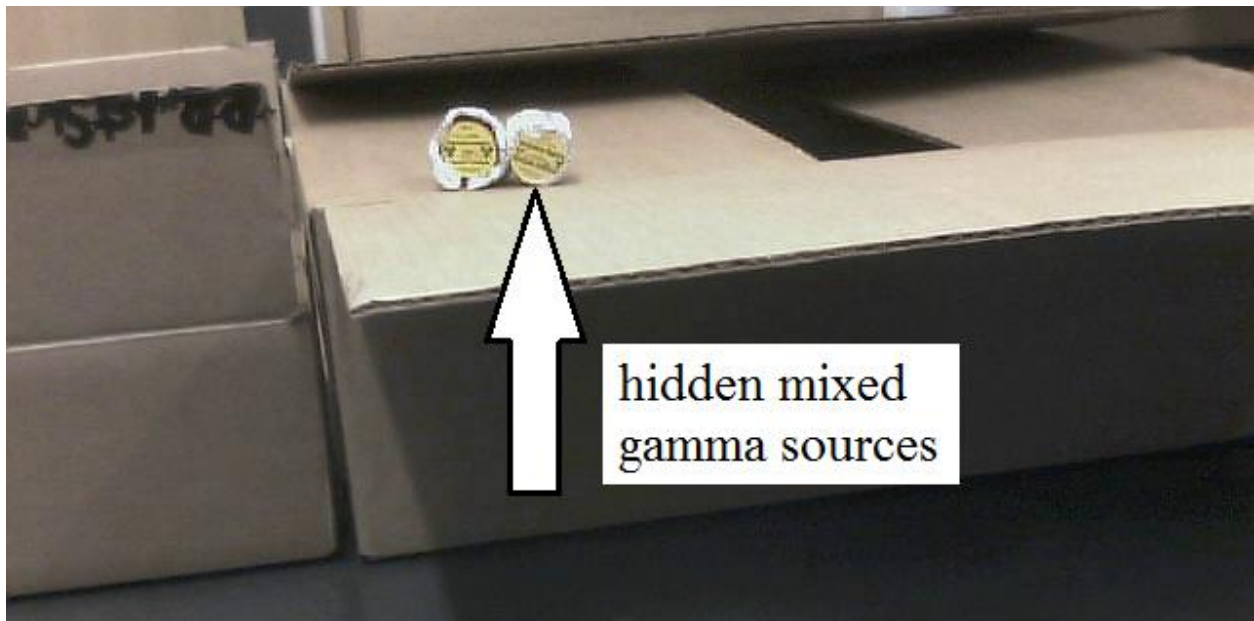


Figure 35: Source seek mode experiment location of hidden sources

Chapter 3: Experimental Results and Discussion

3.1 Directional Profile and Visual Panorama Results: Sweep Scan Mode with Count Rate Measurements

3.1.1 Gamma Ray Directional Profile Results

As described in Section 2.8.2, a 1 mCi ^{137}Cs source was placed at 0° , 30° , 60° and 90° relative to the right side of the robot at a distance of 2 m and a 180° sweep scan with 5° steps was performed for each source position. Figure 36 shows the results of these four scans. The angle of measurement is plotted on the horizontal axis of and the LaBr_3 detector count rate response is plotted on the vertical axis.

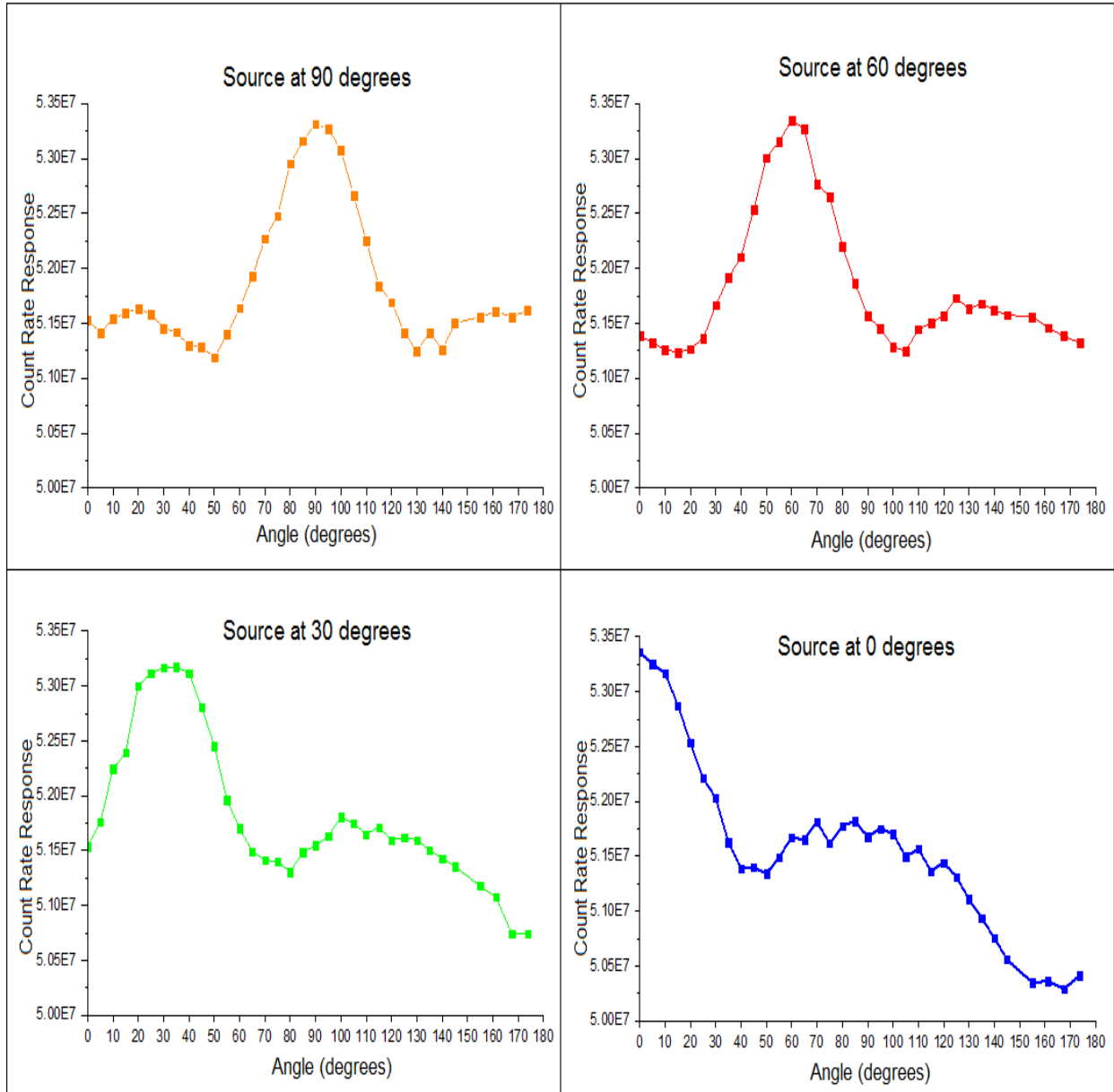


Figure 36: Directional profile results for a 1mCi ¹³⁷Cs point source at 0°, 30°, 60° and 90°

Each graph shows a clear peak centered in the direction of the point source with the highest point of the peak at the angle of the source with the exception of the 30° position, where the measurement at 35° is slightly higher. The case where the source was located at 0° shows a maximum at 0° which is at the boundary of the robot's field of view. However, the consistency of the shapes of these graphs indicates that a peak at 0° would be measured if measurements

were taken at angles beyond (to the right side) of this point. The result at 90° is similar to the analytical simulation presented in Figure 9 including the central maxima and two minima. Three additional 180° sweep scan measurements were recorded with no radioactive sources present in order to measure the radiation background. The results from Figure 36 along with the radiation background measurements are shown in Appendix C (Figure A4). All measurements with the sources present produced count rate measurements significantly above the radiation background.

3.1.2 Visual Overlay Results

A visual panorama of the local area was constructed and the data from Figure 36 was overlaid onto the image using the GNU Image Manipulation Program (GIMP). Objects were positioned at 0° , 30° , 60° and 90° to indicate visually where the source was placed. The results are shown in Figures 37-40. In each case the peak of the gamma ray profile data clearly indicates where the radioactive source was located.

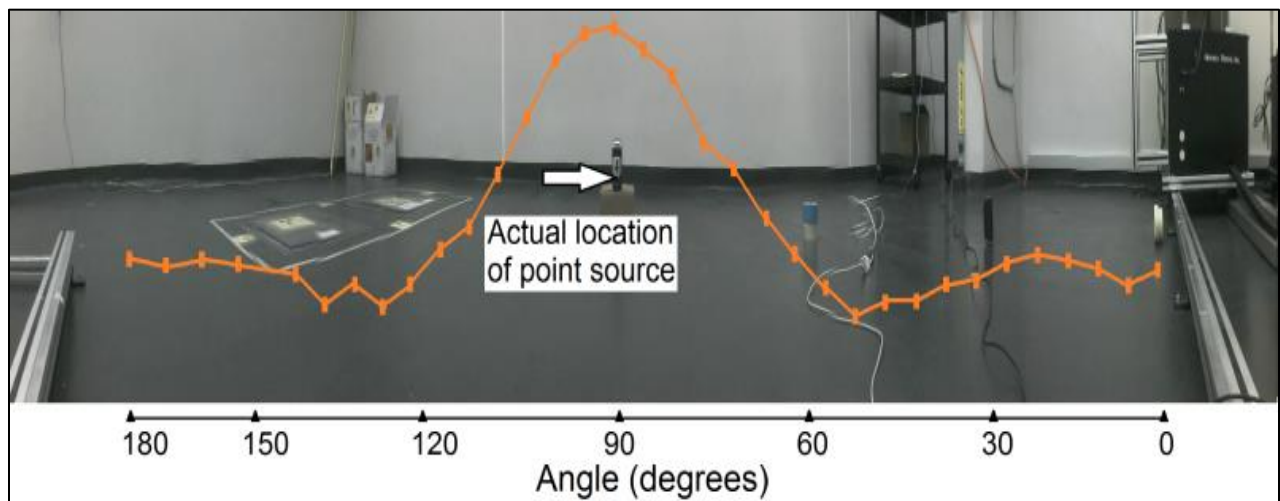


Figure 37: Panorama and directional profile overlay for source at 90°

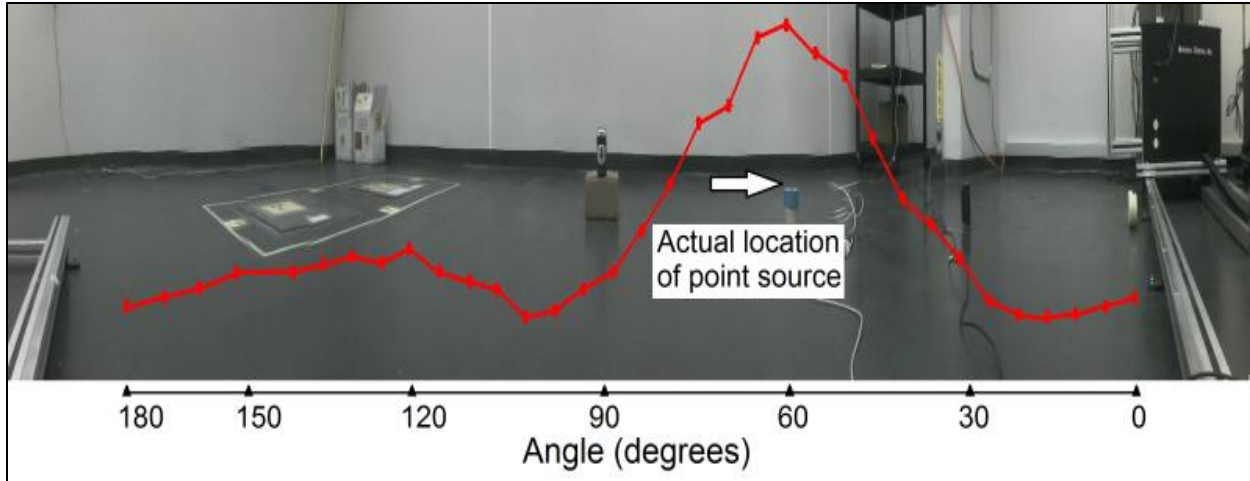


Figure 38: Panorama and directional profile overlay for source at 60°

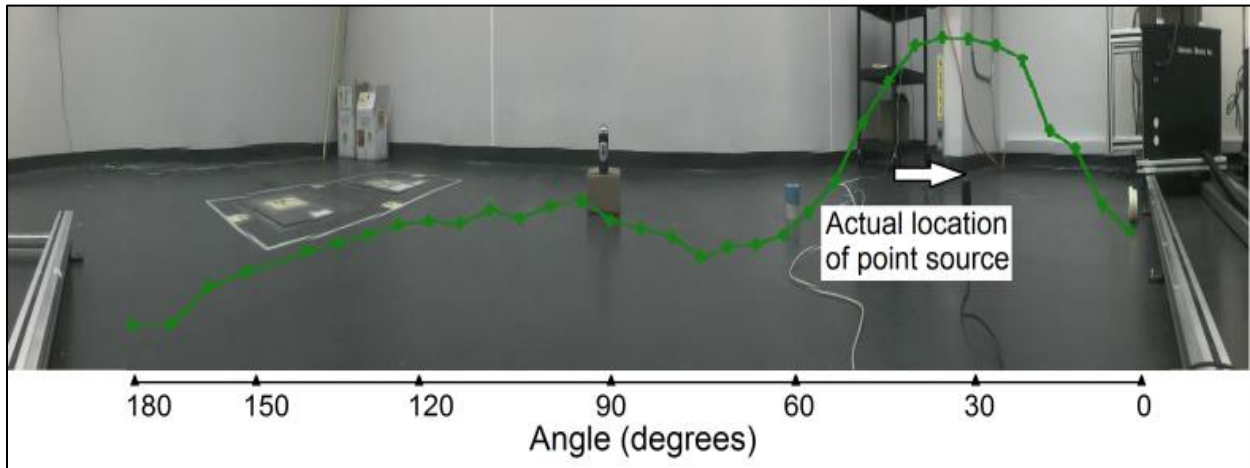


Figure 39: Panorama and directional profile overlay for source at 30°

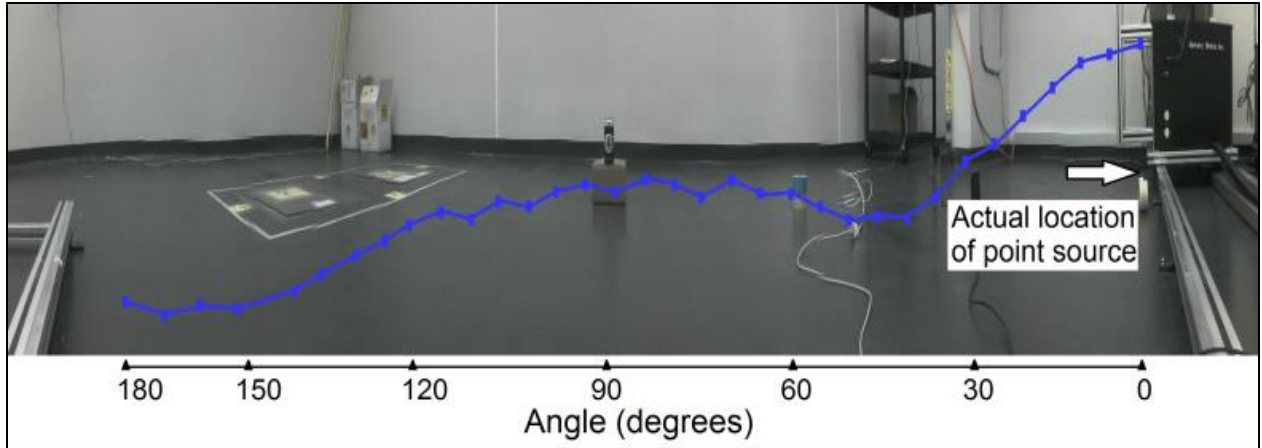


Figure 40: Panorama and directional profile overlay for source at 0°

3.1.3 Point Source Directional Localization Results

At the end of each scan, the robot would orient the camera to indicate the estimated direction of the gamma source. The point source is intended to appear as close as possible to the center of view of the camera, thus indicating the location of the source to the robot operator. The camera view for the source positions at 0° , 30° , 60° and 90° are displayed in Figure 41. The target circle indicates an area slightly less than 10° across. This means that the right and left boundary of the target circle indicate the position of the count rate measurement before and after the measurement from the middle of the target respectively. The white arrow indicates the actual position of the point source in each case. The horizontal field of view of the camera image is approximately 40° .

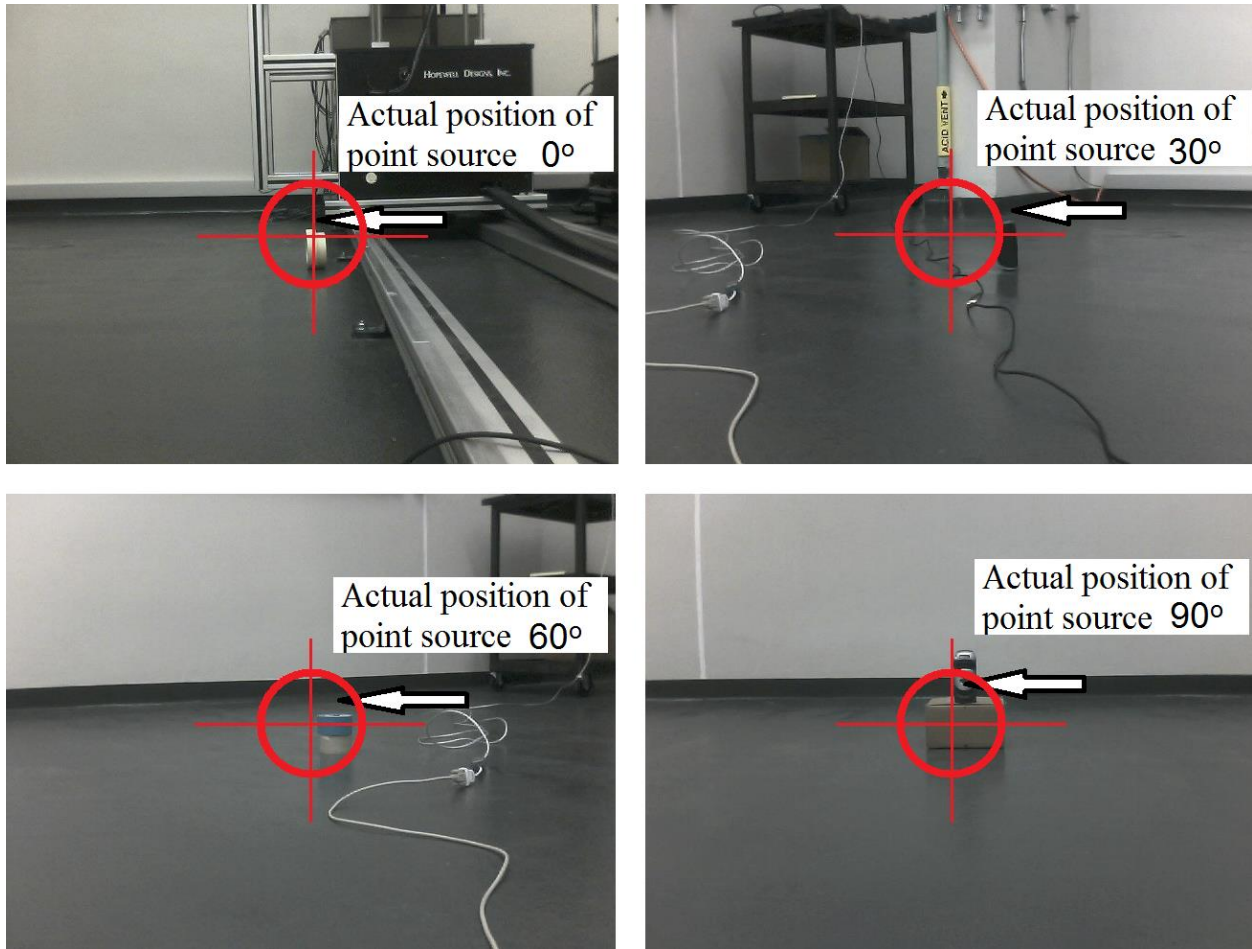


Figure 41: Source locations indicated by mobile robot

In every case the source is very near the center of view (within 7°). The largest deviation is the result with the source positioned at 30° where the robot indicated a source direction closer to 35° . This is because the absolute maximum of the directional profile peak was used as the estimated source direction in the robot's software. However, if the centroid of the directional profile peak was used instead of the maximum value, the indicated direction would be very near 30° (see Section 3.6.1).

3.1.4 Multiple Point Source Results

Two 1 mCi ^{137}Cs sources were placed at 60° and 120° relative to the robot and a 180° sweep scan measurement was recorded as described in Section 2.8.2. The results are shown in Figure 42. There are two peaks located near 60° and 120° , respectively. In this particular experiment, the stepper motor used to rotate the detector was less precise and the step angle used was 9° as opposed to 5° used in the previous experiments. However, the overlay of the data from Figure 42 on to the visual panorama shown in Figure 43 still displays a good correspondence of the peaks to the actual location of the point sources.

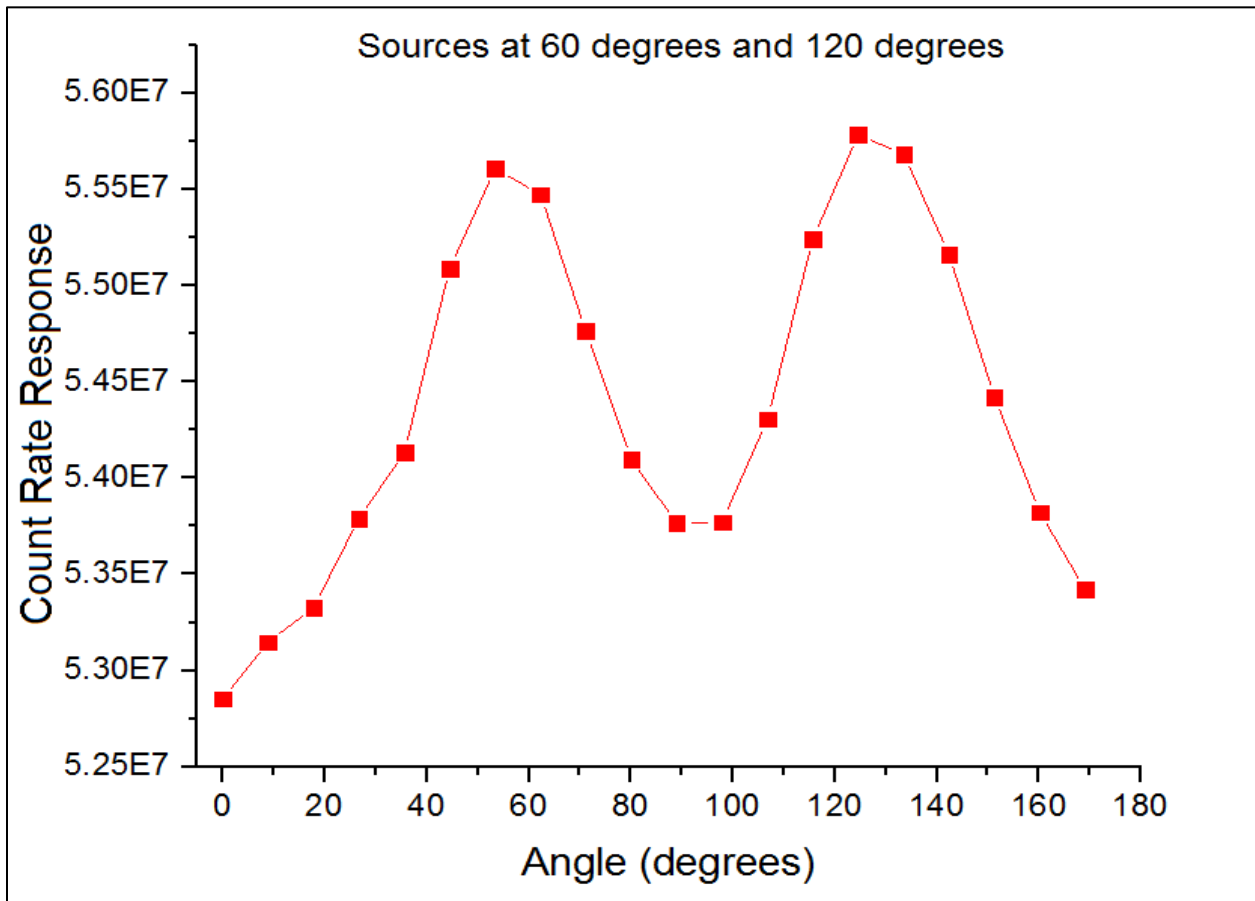


Figure 42: Directional profile results for two ^{137}Cs sources at 60° and 120°

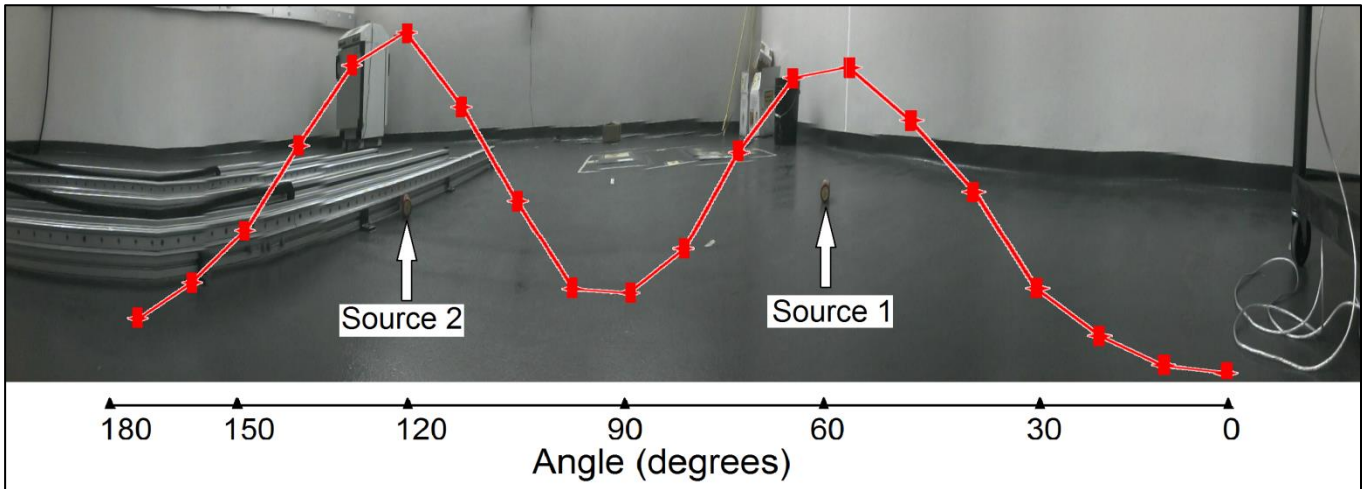


Figure 43: Panorama and directional profile overlay for two sources at 60° and 120°

The robot software identified the peak from source 2 as the direction of highest gamma ray measurements and turned the camera to center the source in the camera view. The result is shown in Figure 44. The camera position corresponding to the slightly smaller peak from source 1 is also shown. Both camera positions have a centre point within 5° of the true source location.

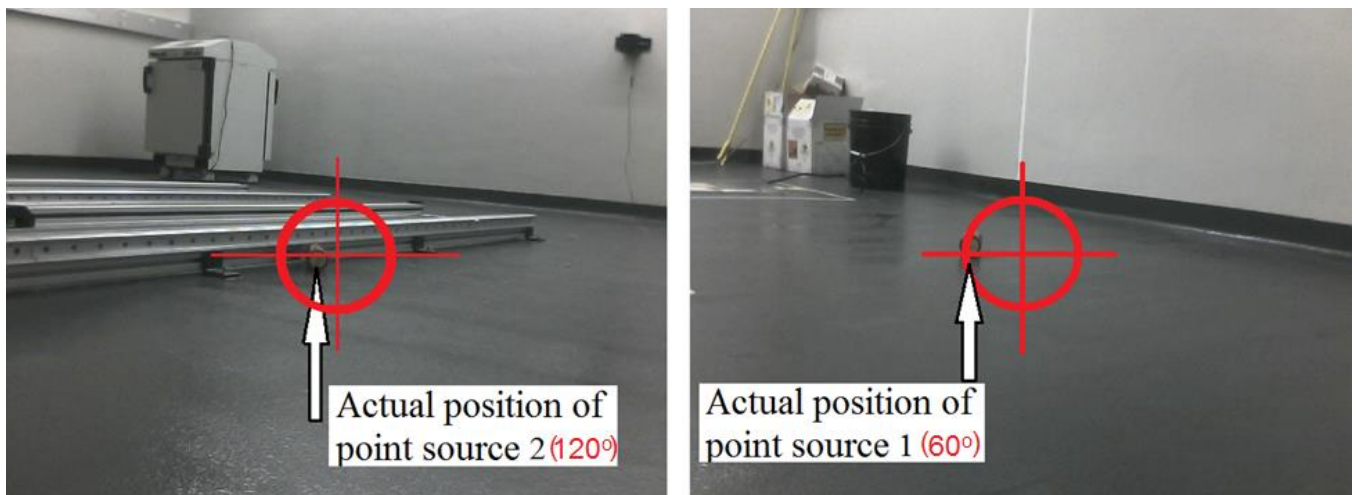


Figure 44: Multiple source locations indicated by mobile robot

3.1.5 Directional Profile Results with Natural Distributed Mixed Alpha, Beta and Gamma Source

The robot was placed approximately 30 cm away from an aquarium filled with rocks known to be radioactive due to contents resulting from thorium and uranium decay chains. A 180° sweep scan was performed in steps of 4.5° and the directional gamma ray profile was constructed. A visual panorama was also recorded by the onboard camera. The directional gamma ray profile data is shown in Figure 45. A second directional profile was recorded with no radiation sources present and is also plotted in Figure 45 for comparison. The background measurements here are slightly smaller than the background measurements in Figure A4 (Appendix C) due to changes made in the robot's electronics after the first set of experiments.

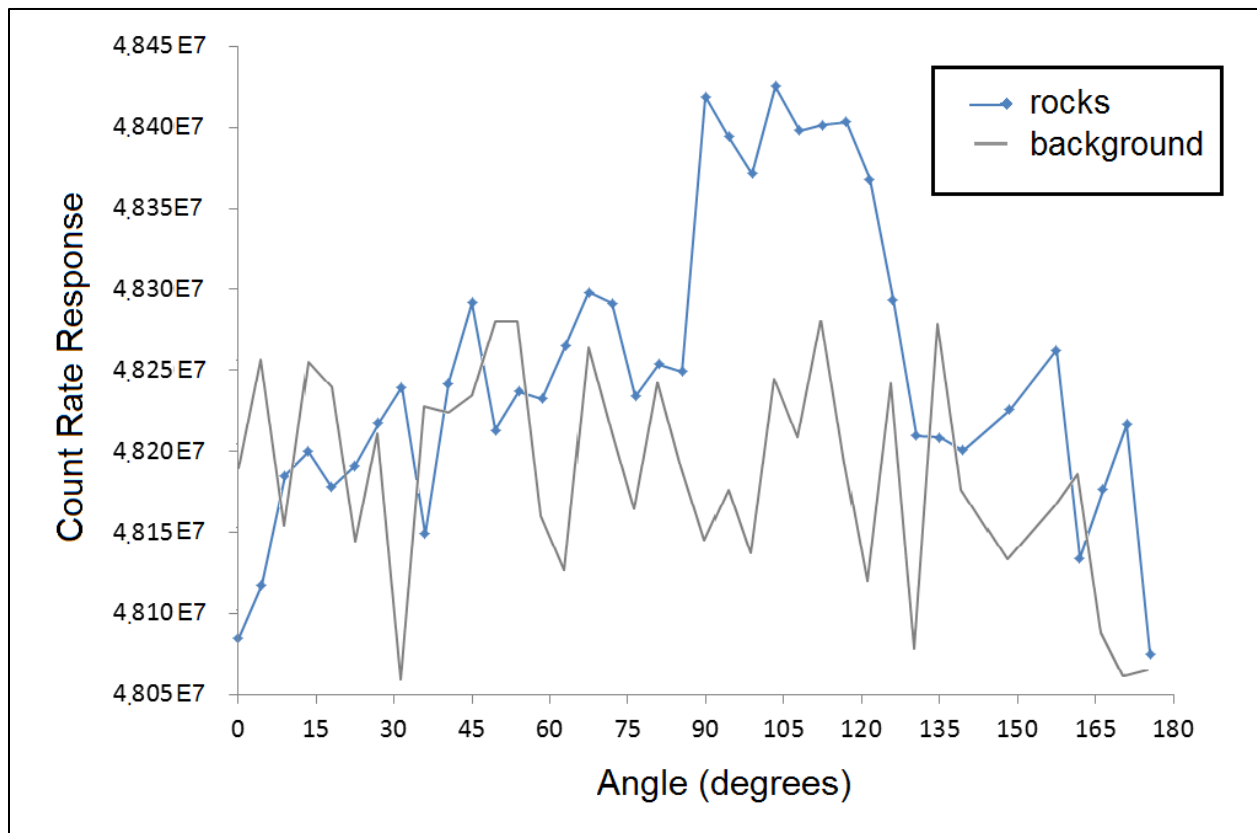


Figure 45: Directional profile results for natural rock source

The directional gamma ray profile recorded from the rocks shows a distinct plateau between 90° and 117° where all of the gamma ray measurements are noticeably above the background noise. These directions correspond very well to the boundaries of the rock pile as seen from the robot's perspective. A single distinct peak is not observed because the source occupies a larger area than a single point source. The correlation of the plateau to width of the rock pile is clearly seen when the data is overlaid onto the visual panorama as shown in Figure 46.

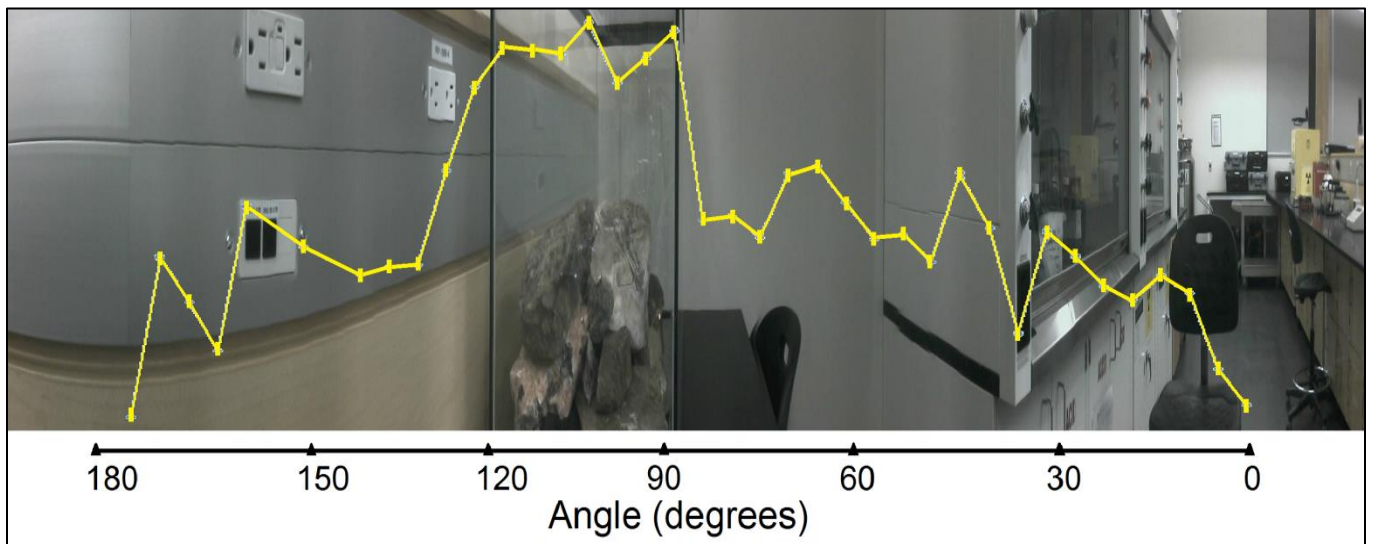


Figure 46: Panorama and directional profile overlay for natural rock source

At the end of the sweep scan the robot turned the detector to center the direction of highest measured gamma ray intensity in the camera's field of view. The rock pile is clearly centered in the image and the robot successfully identified that direction as being a source of detectable gamma rays. The result is shown in Figure 47.



Figure 47: Natural rock source target location indicated by the mobile robot

3.2 Directional Profile and Visual Panorama Results: Sweep Scan Mode with Energy Spectra

The calibration spectra recorded with the ^{137}Cs and ^{60}Co button sources described in Section 2.8.2 is shown in Figure 48.

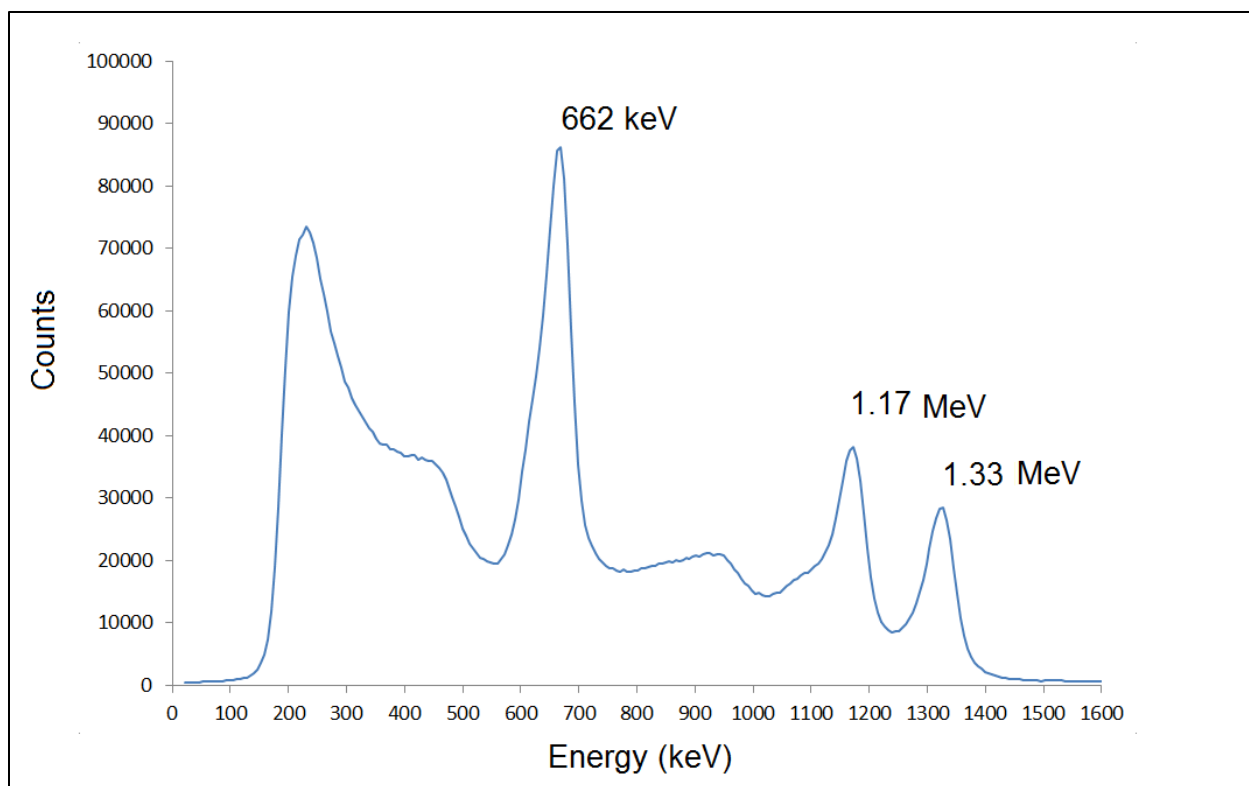


Figure 48: Gamma Ray Energy Calibration Spectra

After obtaining a proper energy calibration the directional experiments described in Section 2.8.3 were performed. A $28.7 \mu\text{Ci } ^{137}\text{Cs}$ source was placed directly in front of the robot (90°) at a distance of 150 cm and a $2.2 \mu\text{Ci } ^{60}\text{Co}$ was placed at an angle of 45° and distance of 45 cm. 180° sweep scans (with spectra) in step angles of 4.5° were performed and a visual panorama was recorded. The spectra and directional data were plotted in a 2D count frequency histogram with the detector angle along the x-axis and the incident gamma ray energy along the y-axis (from Section 2.6.1). The result is shown in Figure 49. Energies below 500 keV were removed from the histogram since the peaks of interest in these measurements are all above this energy. This was done so that the gamma peaks of ^{137}Cs and ^{60}Co would appear more prominent in the figure.

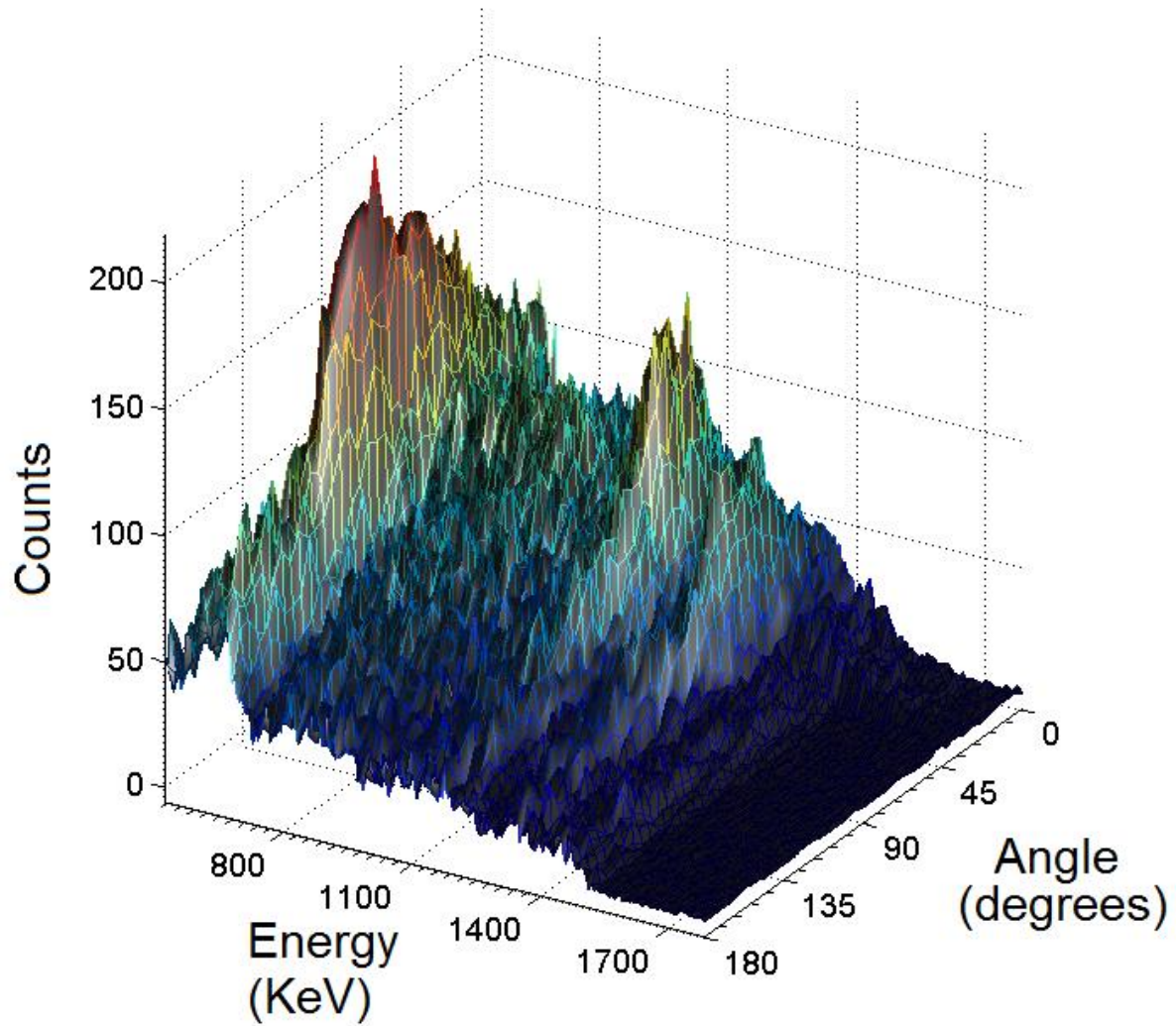


Figure 49: Raw frequency data for spectra and directional profile

A 1D Gaussian filter was used to smooth the data from Figure 49 along the x-axis to allow for an estimation of the centroid of the directional measurement peaks. The smoothed results are shown in Figure 50.

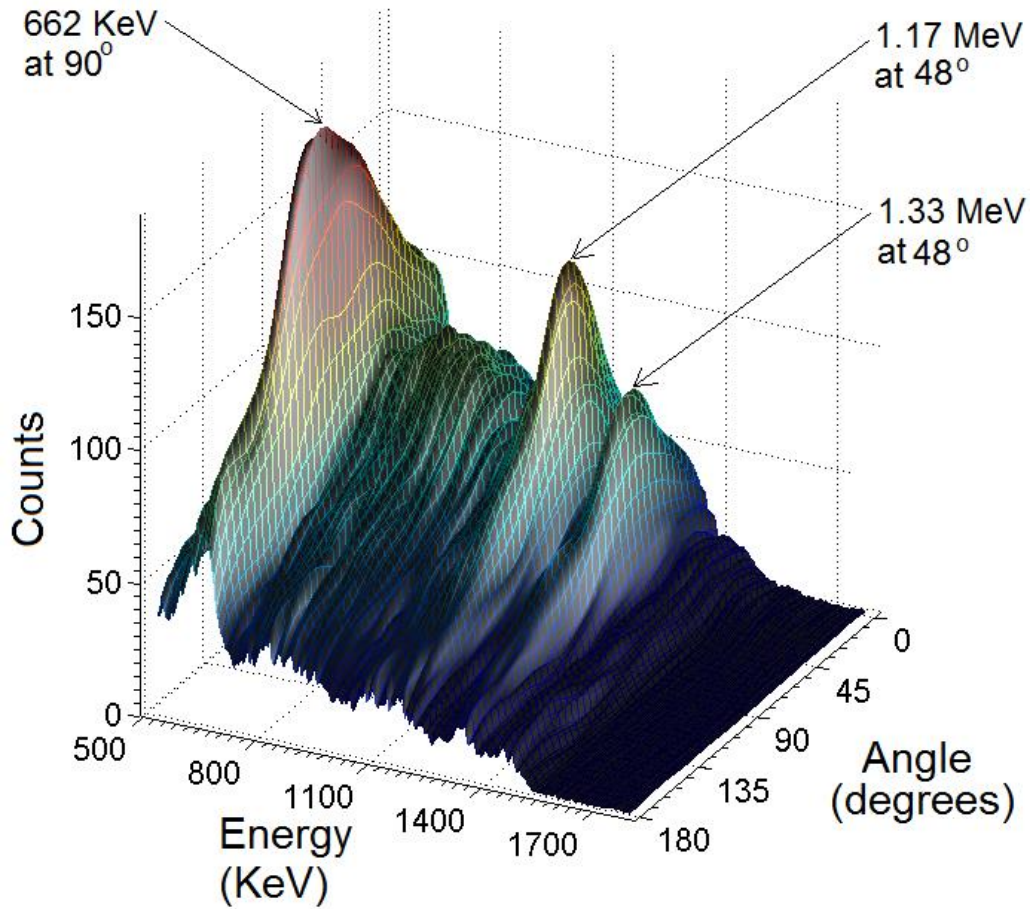


Figure 50: Smoothed spectra and directional profile

When the graph from Figure 50 is viewed side on (from the perspective of the +y axis) the spectra of all incoming gamma rays from every direction is revealed in a typical energy spectra as shown in Figure 51. It is clear in this case that there is a peak at 662 KeV from ^{137}Cs source as well as peaks at 1.17 MeV and 1.33 MeV from ^{60}Co source.

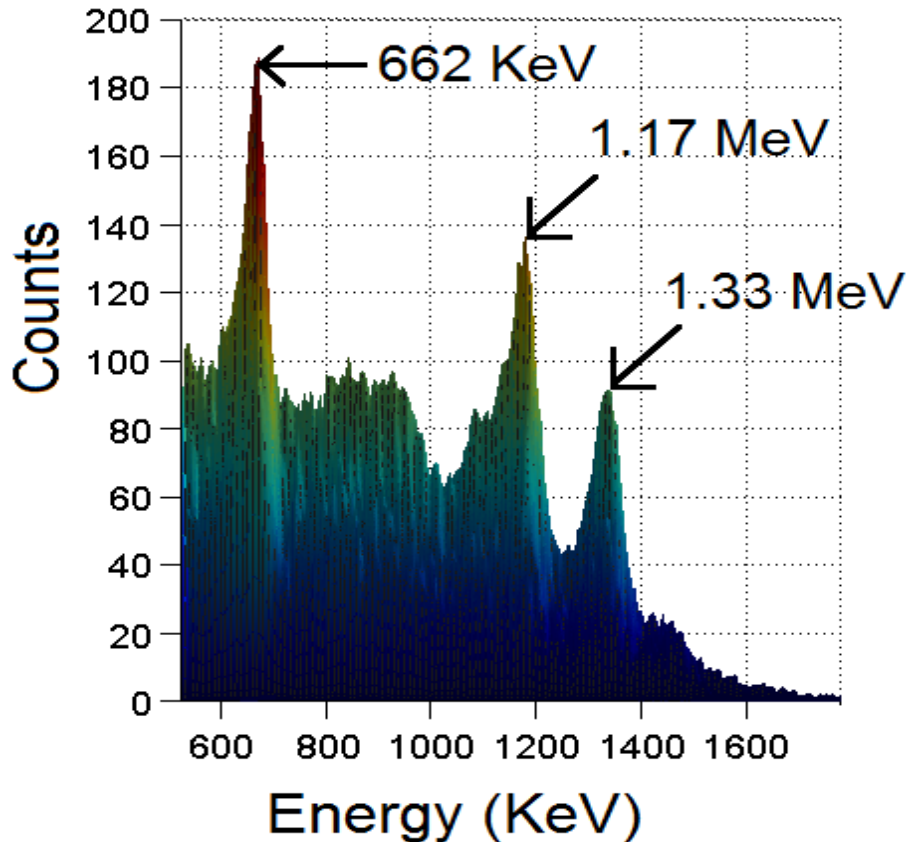


Figure 51: Total energy spectra profile

The peaks on the graph in Figure 50 represent the direction and energy of incoming gamma rays. There is a clear peak at 90° with energy 662 keV indicating that there is a ^{137}Cs source directly in front of the robot. There are two distinct peaks at 1.17 MeV and 1.33MeV both located at 48° . This indicates that there is a ^{60}Co source in that direction.

The directional profile data for the energies corresponding to ^{137}Cs and ^{60}Co were extracted from Figure 50 and overlaid on top of the visual panorama taken by the robot's camera and the result is shown in Figure 52.

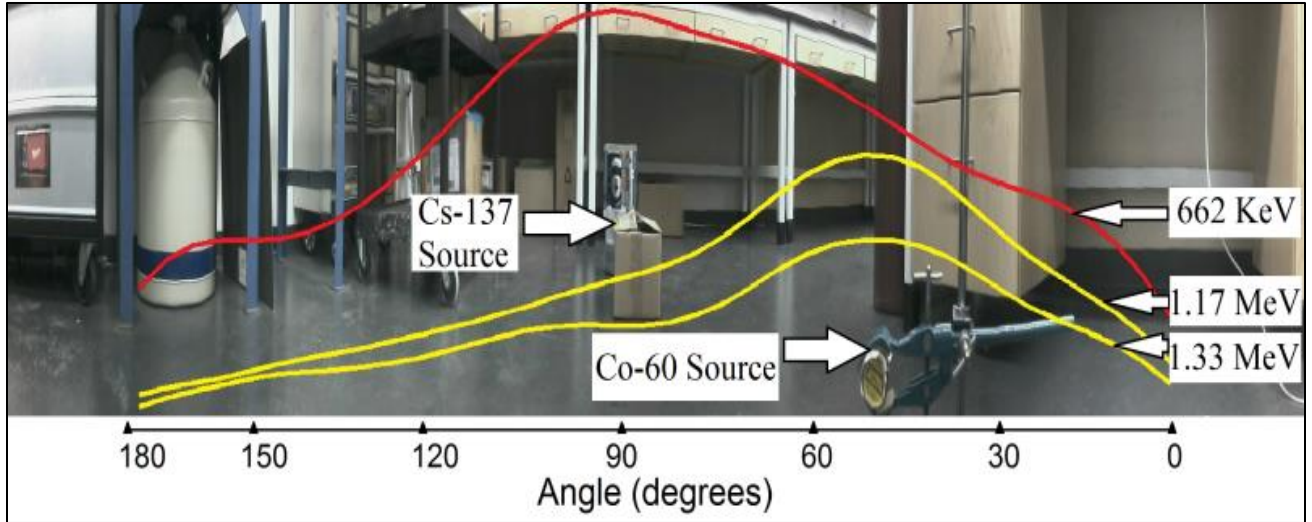


Figure 52: Panorama and directional profile overlay for ^{137}Cs (red) and ^{60}Co (yellow)

The peak of each curve corresponds closely to the location of the source. The closest camera positions corresponding to the directional profile peaks are shown in Figure 53. In both cases the camera's center point is very near the actual source. The camera is mounted above the detector so the nearby ^{60}Co source appears below the vertical center of the image. Nevertheless, the source is in the horizontal center of the image as expected. The camera direction corresponding to the ^{137}Cs directional profile peak is exactly 90° . The closest camera position to the directional profile peak of for ^{60}Co is 49.5° .

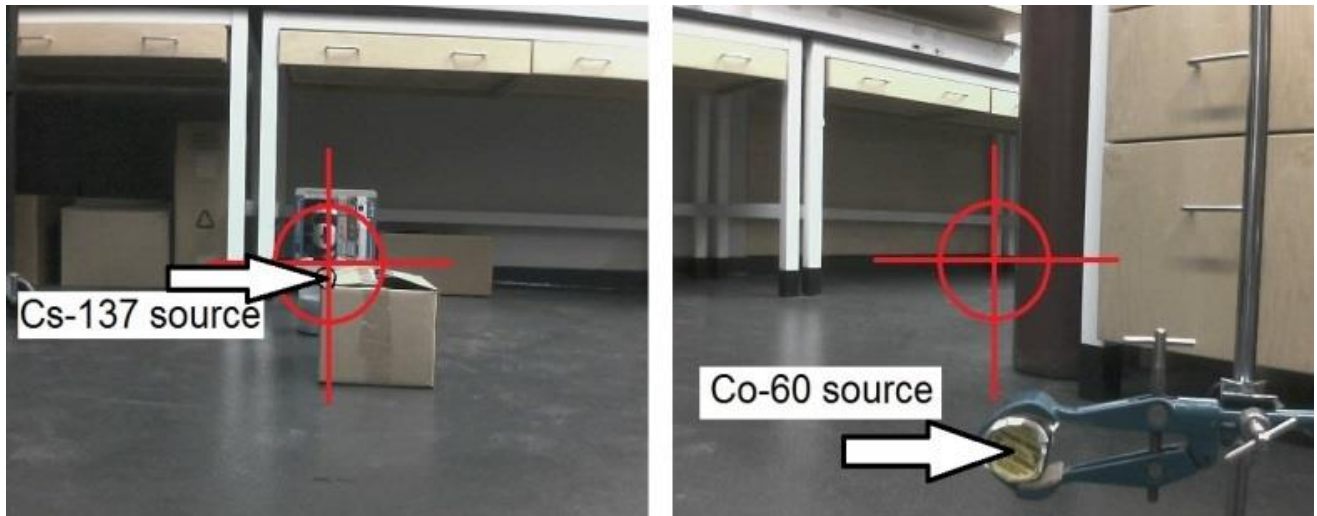


Figure 53: Location of ^{137}Cs at 90° and ^{60}Co at 48° as indicated directional profile peaks

3.3 Rapid Scan Directional Profile Results with Energy Spectra

3.3.1 Rapid Scan Directional Profile Results with ^{133}Ba

A source of $500\ \mu\text{Ci}$ ($1.85 \times 10^7\ \text{Bq}$) ^{133}Ba source was placed near the forward direction of the robot at a distance of approximately 150 cm. The spectra obtained from the rapid scan are shown in Figure 54. It is evident from this figure that there is a large peak at 356 keV in the forward direction at 90° . Using this direction as the region of interest, a 90° forward sweep scan was performed in steps of 4.5° starting from the right-front direction of the robot and ending in the left-front direction.

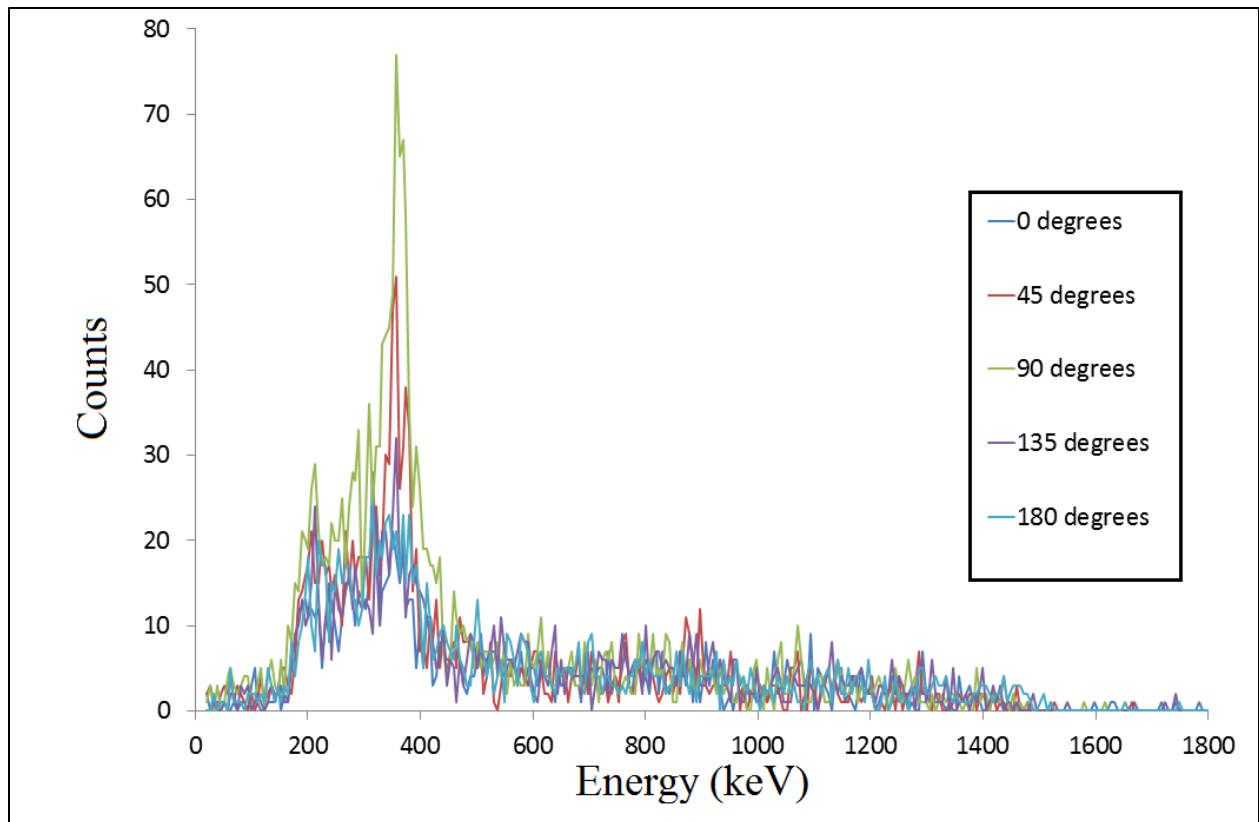


Figure 54: Rapid spectra scan with ^{133}Ba Source

The raw 2D frequency data from the forward sweep scan is shown in Appendix C (Figure A5). The smoothed data is shown in Figure 55. There is a very clear and distinct peak with energy 356 keV at 75° . This indicates that there is a ^{133}Ba source in this direction.

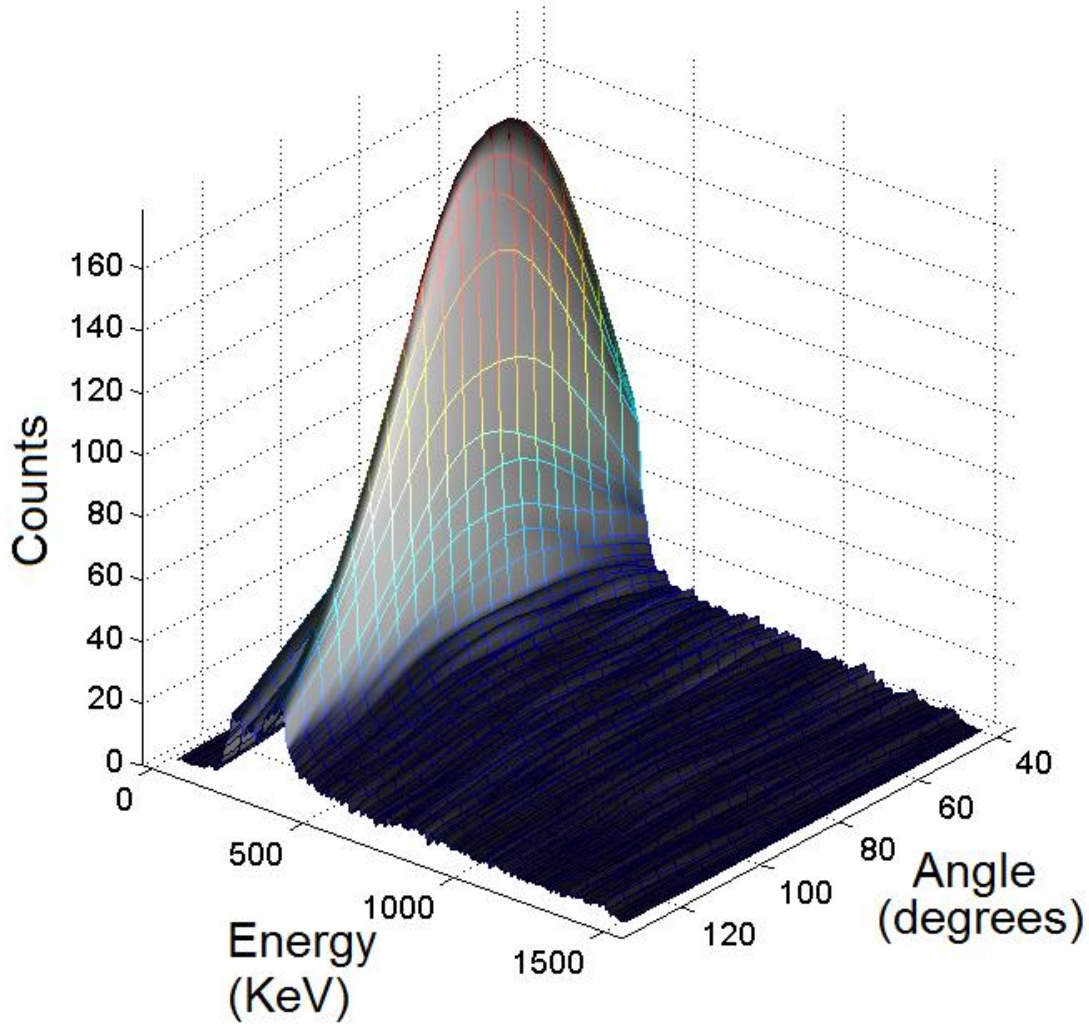


Figure 55: Smoothed spectra and directional profile for forward direction sweep of ^{133}Ba

The gamma ray directional profile from the 356 keV energy channel was extracted from the data in Figure 55 and overlaid on top of the visual panorama captured by the camera. The resulting image is shown in Figure 56. The peak again shows very close correlation to the actual position of the source.

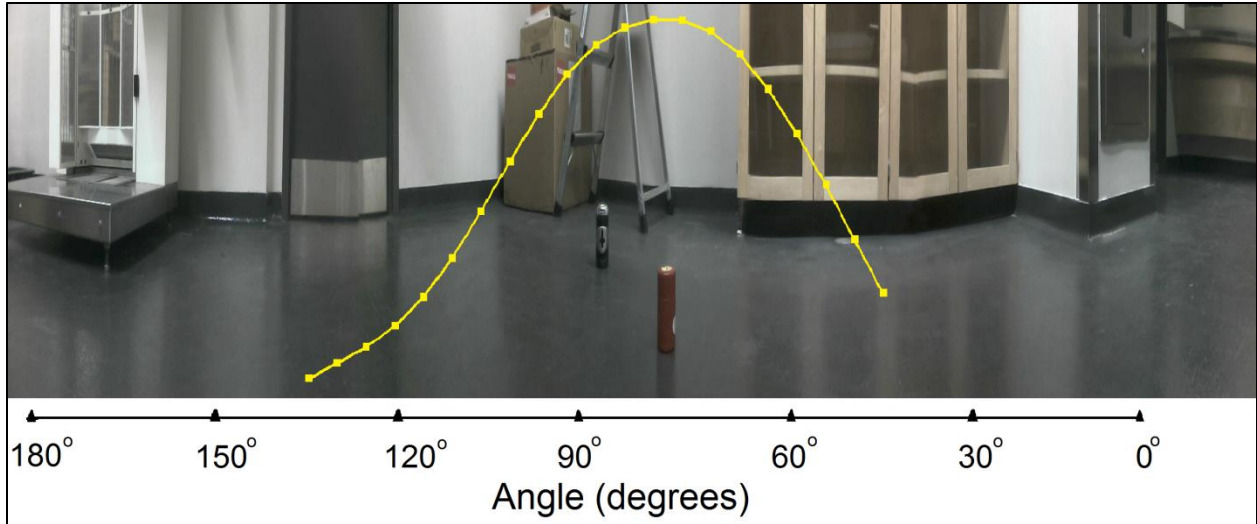


Figure 56: Panorama and smoothed directional profile for 356 KeV Channel from ^{133}Ba source

From the peak of the directional profile, the location of the source was estimated to be 75° . The robot's camera position closest to the estimated direction from the peak is displayed in Figure 57. The camera position in Figure 57 corresponds to 76.5° and the figure shows that the center of the source corresponds very well to this position.



Figure 57: Location of the ^{133}Ba source as indicated by mobile robot

3.3.2 Rapid Scan Directional Profile Results with ^{60}Co

The experiment described in the previous section was repeated with a $500\ \mu\text{Ci}$ ($1.85 \times 10^7\ \text{Bq}$) ^{60}Co source instead of the barium source. The spectra obtained from the rapid scan are shown in Figure 58 and it is clear from this figure that the counts obtained in the 90° direction are larger than all other directions. Two peaks around $1.17\ \text{MeV}$ and $1.33\ \text{MeV}$ are evident, thus indicating a ^{60}Co source is present. The large number of counts in energies from $200\ \text{keV}$ to $1.0\ \text{MeV}$ is a result of Compton scattering of the ^{60}Co gamma rays (see Figure 3).

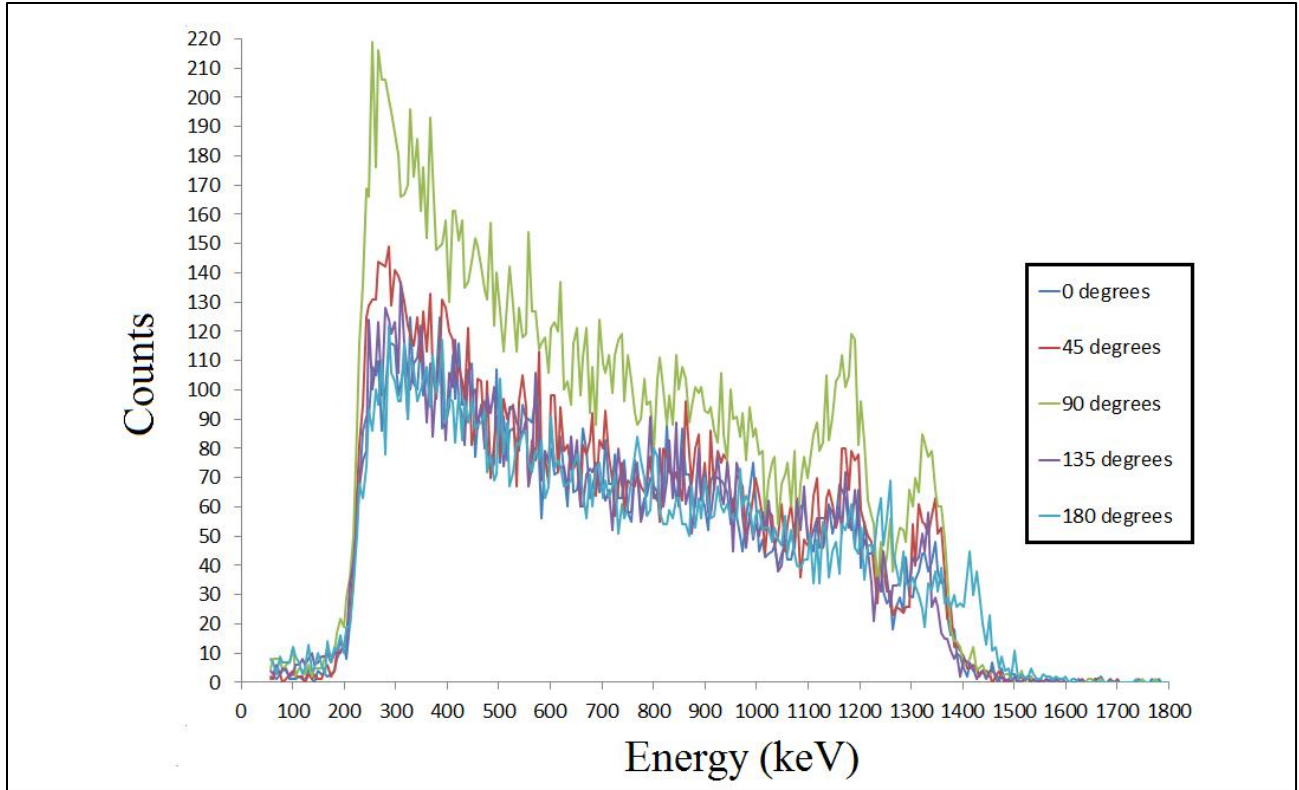


Figure 58: Rapid spectra scan for ^{60}Co Source

A 90° sweep scan was measured in the direction of interest. The 2D frequency data from this scan is shown in Appendix C (Figure A6) and the smoothed data is shown in Figure 59. The characteristic double peak of ^{60}Co is visible in Figure 59. The two peaks indicate energies of 1.17 MeV and 1.33 MeV both located at an angle of 81° .

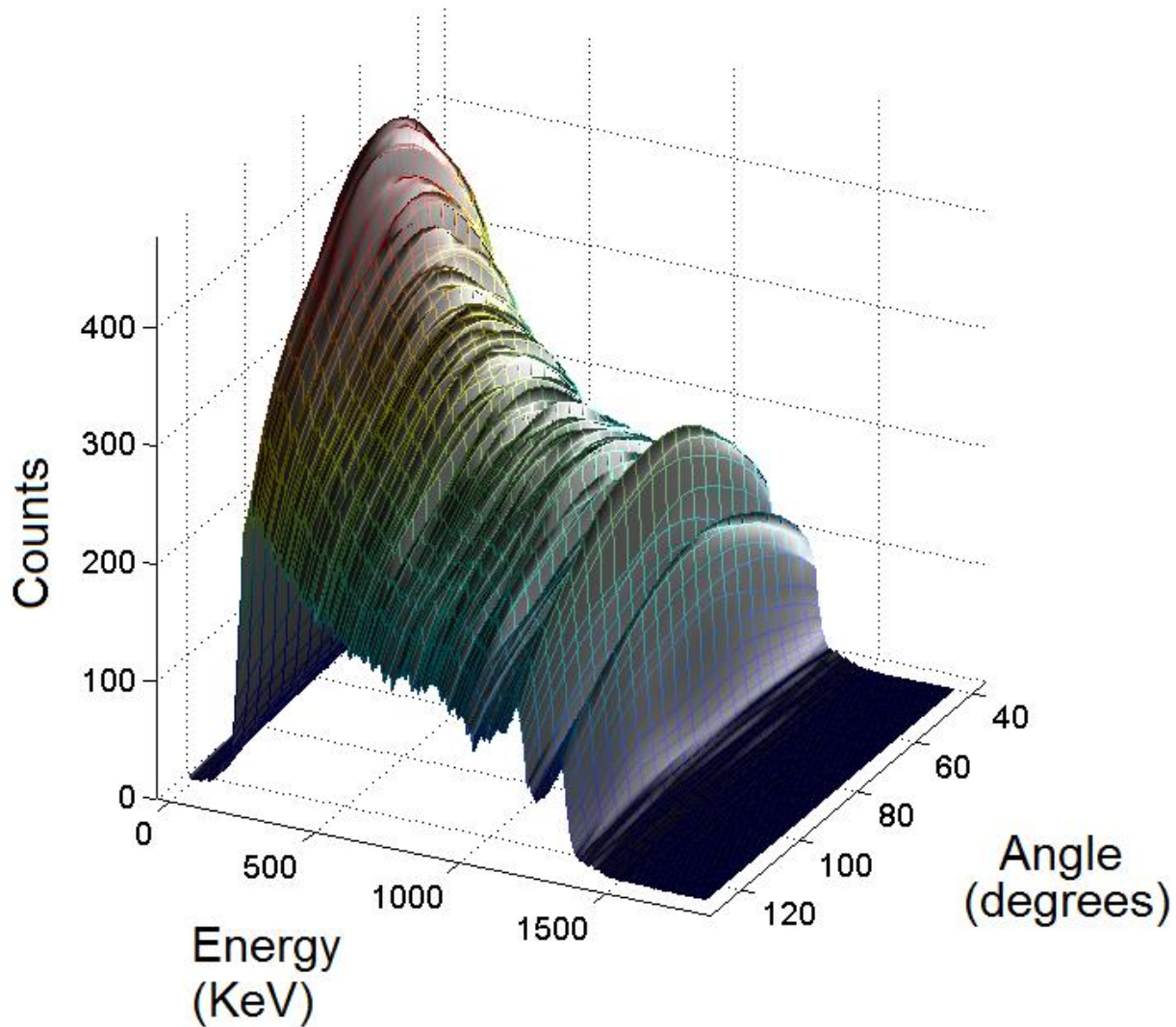


Figure 59: Smoothed spectra and directional profile for forward direction sweep of ^{60}Co

The directional gamma ray profile for 1.17 MeV and 1.33 MeV is shown in Figure 60. The peaks located at 83° (from 1.17 MeV) and 80° (from 1.33 MeV) (see Section 3.6.2) correspond closely to the actual source direction which was measured in the lab to be approximately 80° . No visual panorama was recorded for the ^{60}Co source.

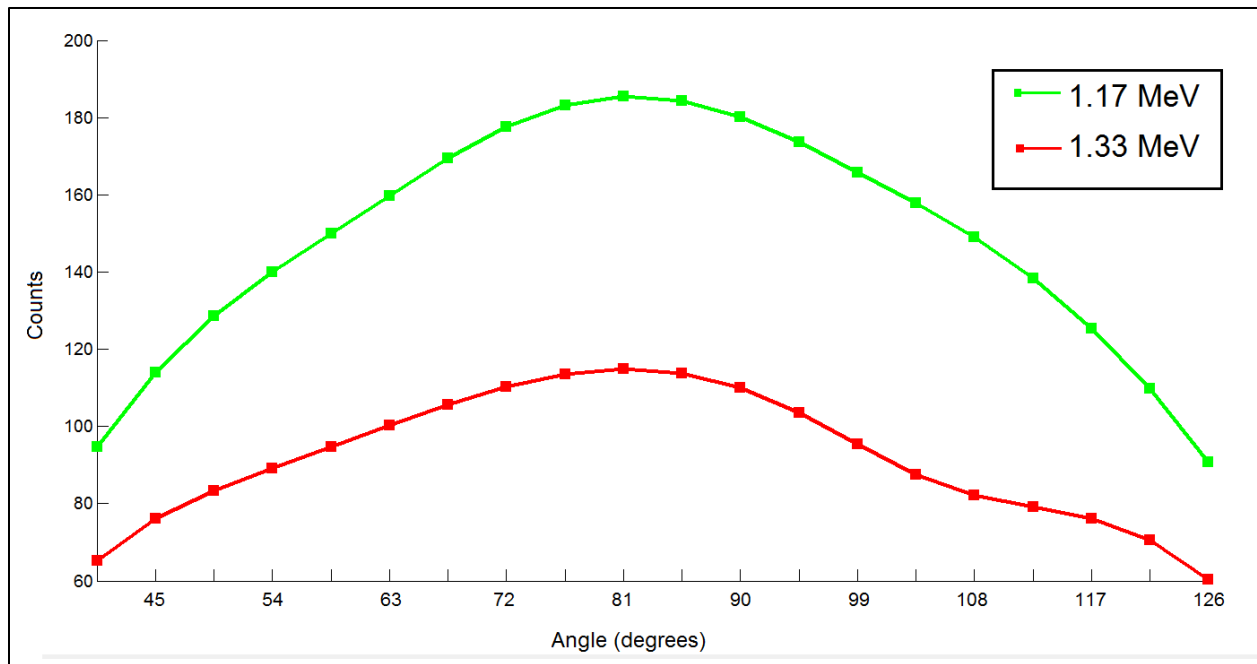


Figure 60: Smoothed gamma ray directional profile for ^{60}Co rapid scan

3.4 Point Source Triangulation

A two dimensional coordinate system was plotted on the floor of the laboratory and key points were marked. A $30.9 \mu\text{Ci}$ ($1.14 \times 10^6 \text{ Bq}$) mixed ^{137}Cs and ^{60}Co source was placed at the (50 cm , 50cm) position of the coordinate system at a height of 15cm and a cardboard box was placed at an arbitrary orientation to obscure the source as described in Section 2.8.5. The robot performed 180° sweep scan measurements in steps of 4.5° at four different positions in the coordinate system with the robot body oriented in the +y axis direction. 180° sweep scans were performed at the following positions (0 , 0), (0 , 30), (0 , 60) and (0 , 90) where the units of the coordinate system are in cm. At each position the direction of the gamma source was determined by the robot as described in section 2.4. Table 1 shows the direction of the source measured at

each position and the true direction. The robot oriented the camera to center the source in the camera's view after each sweep scan. The resulting camera view from each position is shown in Figure 61.

Table 1: Source Directions determined from 4 known robot positions

Robot (x, y) Position ($\pm 0.5\text{cm}$)	Estimated Direction ($\pm 4.5^\circ$)	True Source Direction ($\pm 1^\circ$)
(0,0)	45°	45°
(0,30)	72°	68.2°
(0,60)	99°	101.3°
(0,90)	130.5°	128.7°

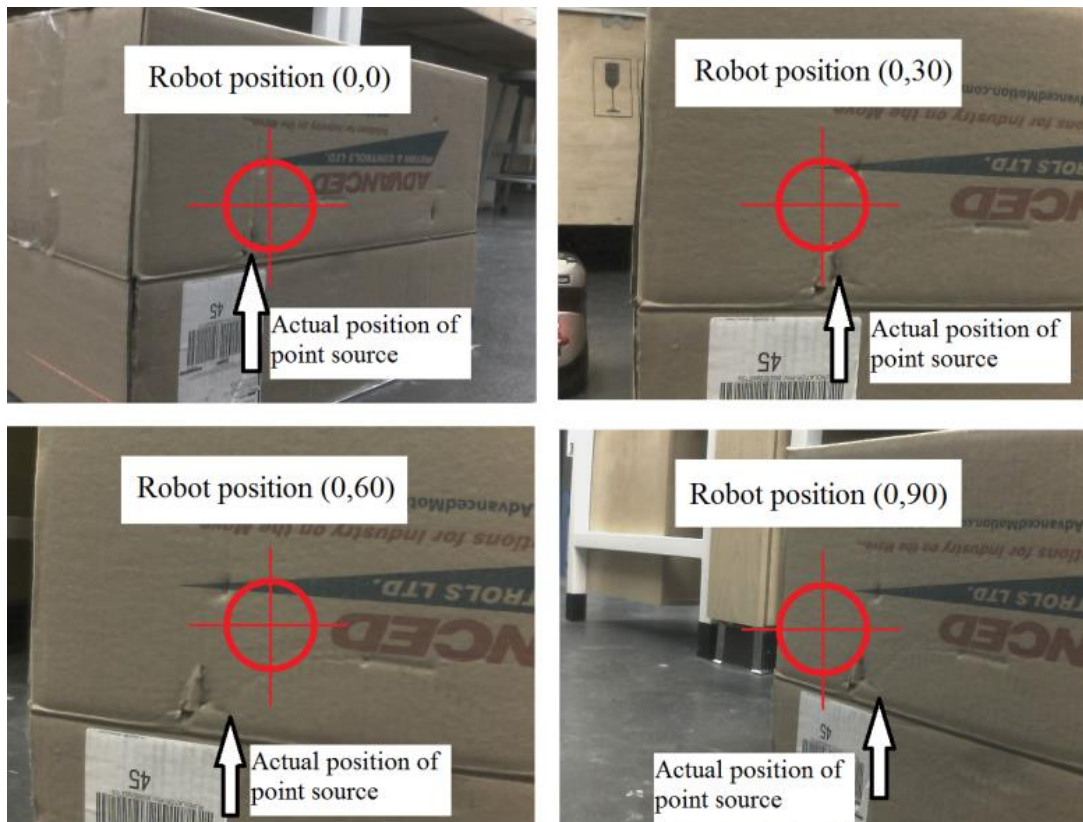


Figure 61: Source direction indicated by the mobile robot from four known locations

The slopes and y-intercepts in the coordinate system (described in section 1.7) were calculated for each of the four measurement positions using MATLAB. Putting the slopes and intercepts from this experiment into equation (16) gives the following matrix equation:

$$\begin{bmatrix} -1.00 & 1 \\ -3.07 & 1 \\ 6.31 & 1 \\ 1.17 & 1 \end{bmatrix} \begin{bmatrix} x \\ y \end{bmatrix} = \begin{bmatrix} 0 \\ -92.33 \\ 378.82 \\ 105.37 \end{bmatrix} \quad (20)$$

The sum of least squares solution for the source position described in Section 1.7 was calculated in MATLAB (using equation 19). The estimated position of the source using this method was found to be (50.5, 54.9) which is near (within 5 cm) the true position of (50 cm, 50cm). Figure 62 shows a top-down photo of the experiment including the box and the robot positioned at the origin. The perimeter of the box was marked on the floor and the position of the source was marked with a red “star”. The position of the source as estimated above was marked with a blue “x” for comparison. Figure 63 shows a closer view of the region inside the box with a scale marked for the box and the distance between the true source position and estimated source position.

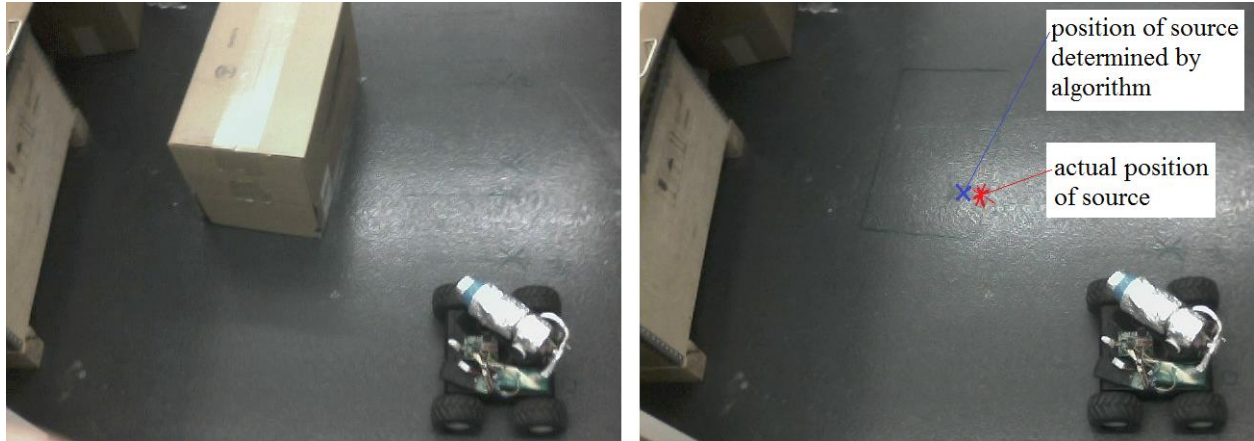


Figure 62: Top-down view of triangulation experiment

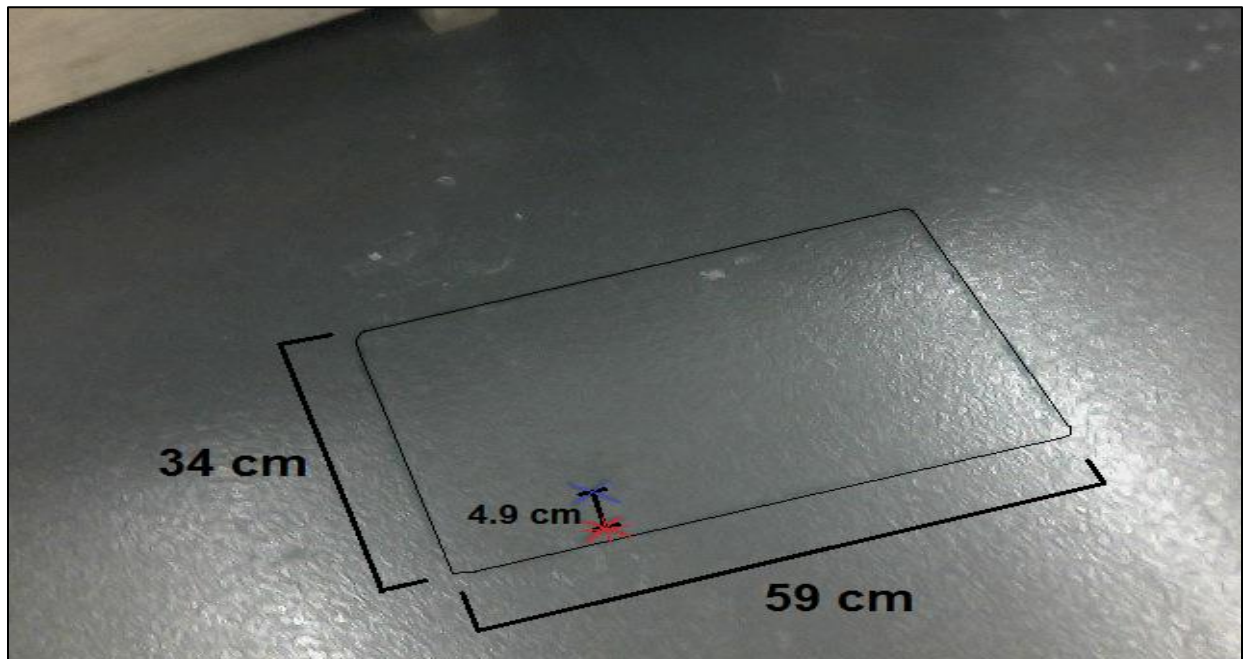


Figure 63: Triangulation experimental results (Actual source position is shown as red “star” and estimated position is shown as blue “x”). The scale of the box is given. The distance between the estimated source position and the true source position is 4.9 cm.

A map of the area of the experiment was plotted in MATLAB and is shown in Figure 64 with the actual position of the source indicated by a red star and the estimated position of the source indicated by a blue star. In comparison to the size of the box, the position of the source was estimated with a high degree of accuracy. A MATLAB program was designed to determine an

estimate of the confidence interval of the source position determined by the algorithm using a Monte Carlo method to combine the measurement errors. In this program 1000 iterations of the estimated source position calculations were repeated with a random Gaussian distribution noise added to the robot position, source position, and source direction measurements using MATLAB's random number generator. The region containing 500 of the 1000 estimated source position measurements provided an estimate of the 50% confidence interval and the region containing 900 of the 1000 source position measurements provides an estimate of the 90% confidence interval. The result is displayed in Figure 64. The estimate of the 50% confidence interval of the source position is indicated by a smaller oval shape around the estimated source position and the larger oval indicates the 90% confidence interval. The true position of the source is near the 50% confidence interval and within the 90% confidence interval. The confidence intervals are not circles because the measurement positions were taken along the coordinate x-axis in a manner that gave a better estimate of the sources x position than the y position. See Section 3.6.3 for an analytical estimation of the uncertainty in the estimated point source location.

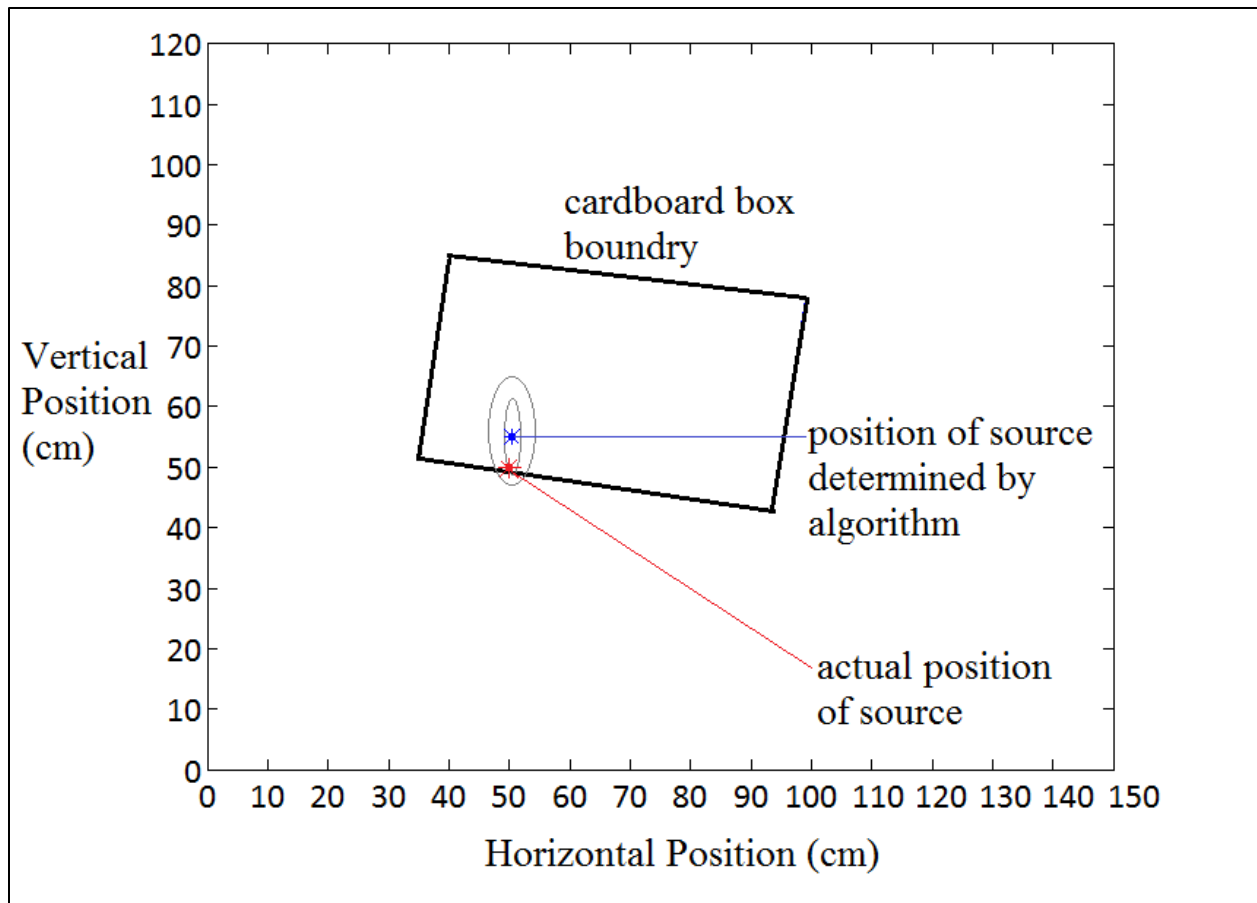


Figure 64: Map of point source triangulation experiment. The oval contours illustrate an estimate of the 50% and 90% confidence intervals. The smaller oval is the region where the source is estimated to reside with a 50% measurement confidence. The larger oval is the region where the source is estimated to reside with a 90% measurement confidence.

3.5 Autonomous Source Seek Mode Results

3.5.1 Source Seek Mode Results

A 1mCi (3.7×10^7 Bq) ^{137}Cs was placed in the middle of a room as described in Section 2.8.6. The robot was placed at a random direction and orientation at a distance between 1 m and 2 m. Figure 65 shows the data collected from one of these trials and Figure 66 shows images captured from a video of the trial. The horizontal axis, on Figure 65, represents the steps in the source seek mode

sequence (see Figures 9-11). The vertical axis shows the detector signal recorded at each step in the sequence. The first 8 data points represent the detector signal measurements in the 360° turning phase of the source seek mode (refer to Figure 17).

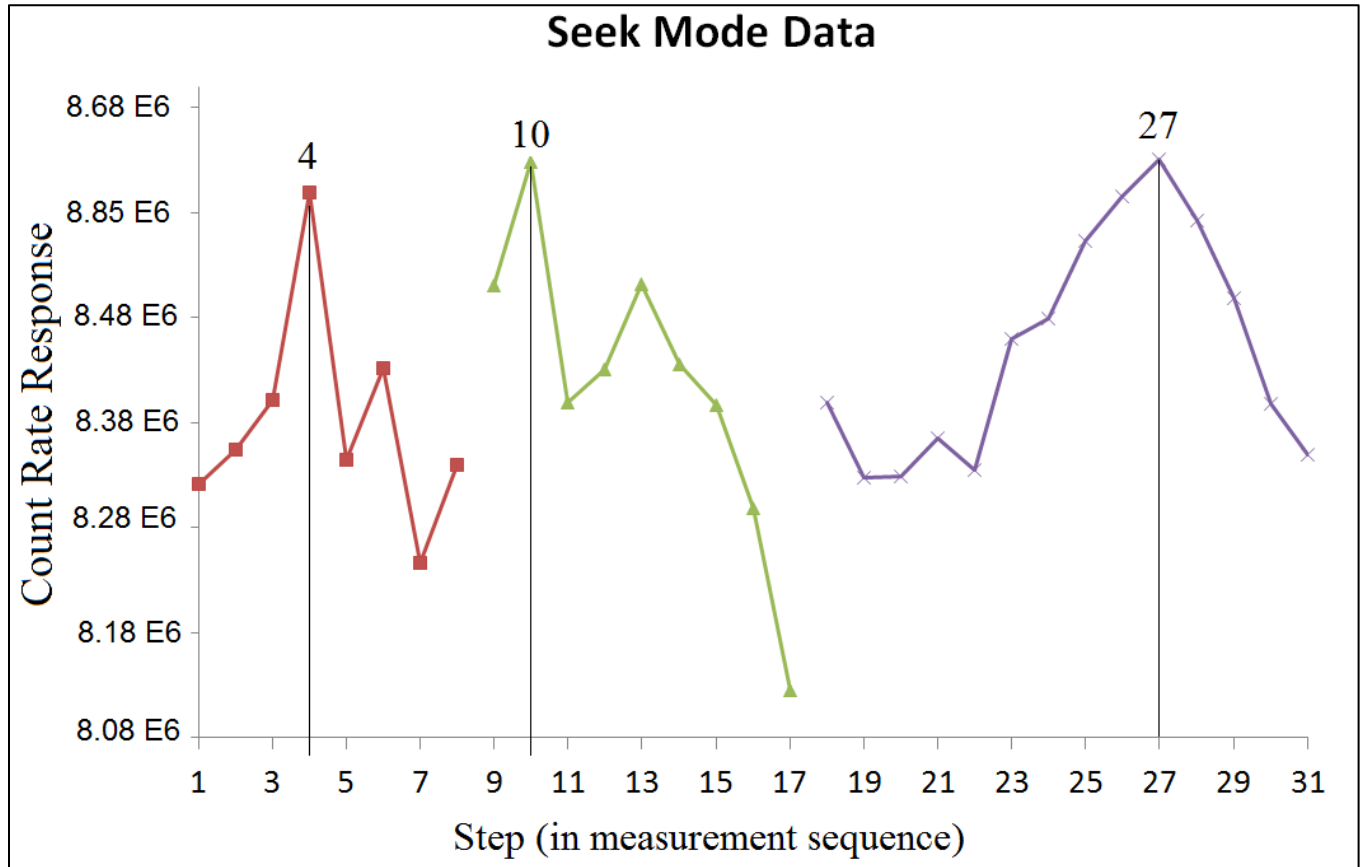


Figure 65: Source Seek Mode Data

Step 4 has the highest recorded detector count rate response in the sequence and it can be seen in Figure 66 that this corresponds to the direction closest to the source. The robot attempted to turn its body toward this direction following this sequence. Steps 9-17 (shown Figure 65) represent the 180° scan that is performed in steps of 22.5° (refer to Figure 18). Figure 67 reveals that the forward direction of the robot is not directed toward the source during this sequence due to over

steering in the turning phase. However, the highest recorded gamma ray signal measured in step 10 still represents the closest direction to the gamma ray source and the robot is able to make a correcting turn after step 17 in order to center the source closer to the forward direction. Figure 67 shows that the robot's forward direction is indeed much closer to the source direction after completing this correcting turn. Steps 18-31 represent the final forward direction scan that the robot performs (refer to Figure 19). The total sweep angle is shown in Figure 67 with lines indicating the sweep angle boundaries. The data from the final sweep scan in Figure 67 produces a peak similar to the peaks discussed in Section 3.1.1 with the maximum corresponding to the location of the source. After the scan was complete the robot turned its detector toward the direction of the source which was measured in step 27. A yellow arrow in step 4 on Figure 67 illustrates the direction of the detector after completing the sequence.

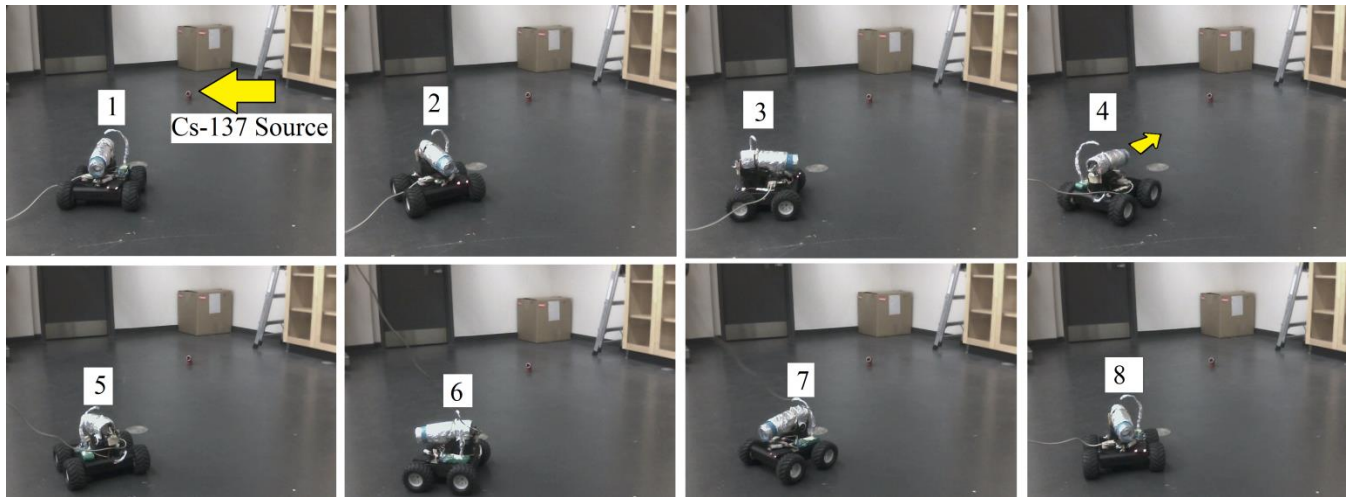


Figure 66: Video sequence of first phase in source seek mode with a 1mCi ^{137}Cs source. The numbers indicate the steps in the source seek mode. The steps run chronologically from left to right and the corresponding gamma measurements from these steps are shown in Figure 65.

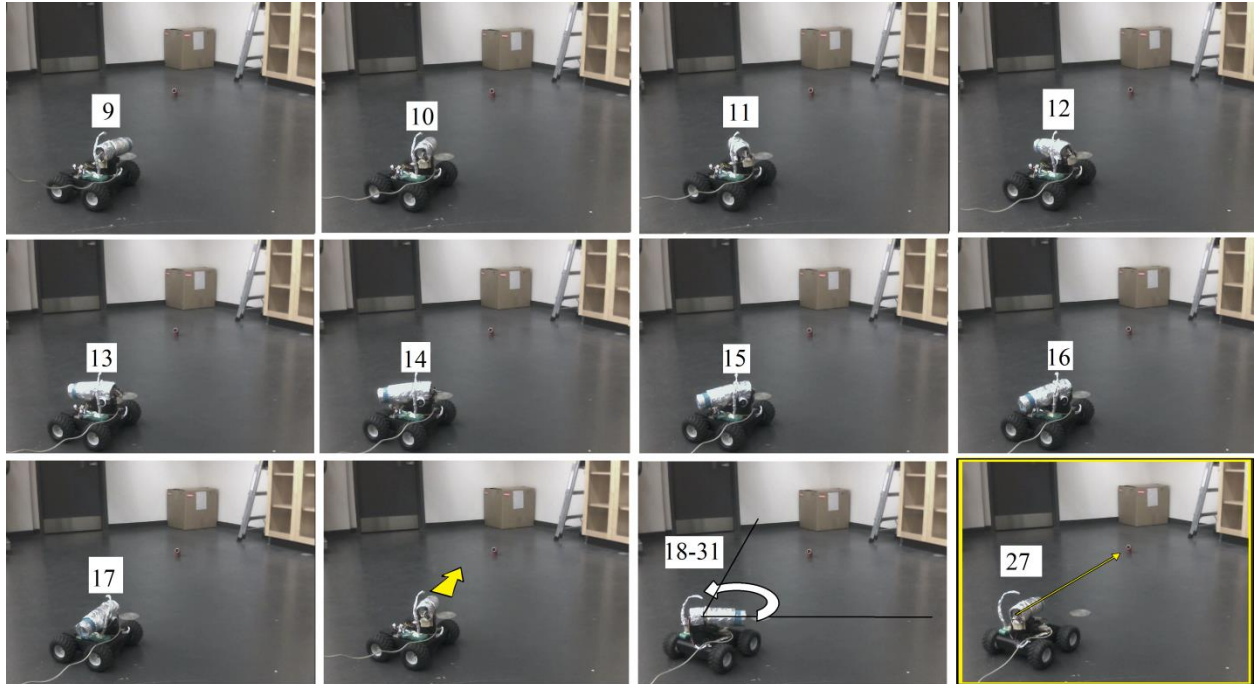


Figure 67: Video sequence of source seek mode with a 1mCi ^{137}Cs source. Steps 9-17 are from the 180° sweep scan with steps of 22.5° . Steps 18-31 comprise the final sweep scan and the source position is indicated as the direction measured in step 27. Corresponding count rate measurements are shown in Figure 65.

3.5.2 Source Seek Mode Results with Hidden Source

A pair of 2.17 μCi mixed button sources containing ^{137}Cs , ^{60}Co , ^{58}Co , ^{133}Ba and ^{22}Na were placed behind a flap on top of a cardboard box. The robot was placed at a random position and orientation at a distance approximately 1.5 m away from the source and the source seek mode was activated. Pictures from a video sequence of the camera mounted on the detector in this experiment are shown in Figure 68. The steps in the source seek mode sequence are indicated on each of the pictures. The direction of highest recorded detector signal in each phase of the seek mode indicated with an arrow.

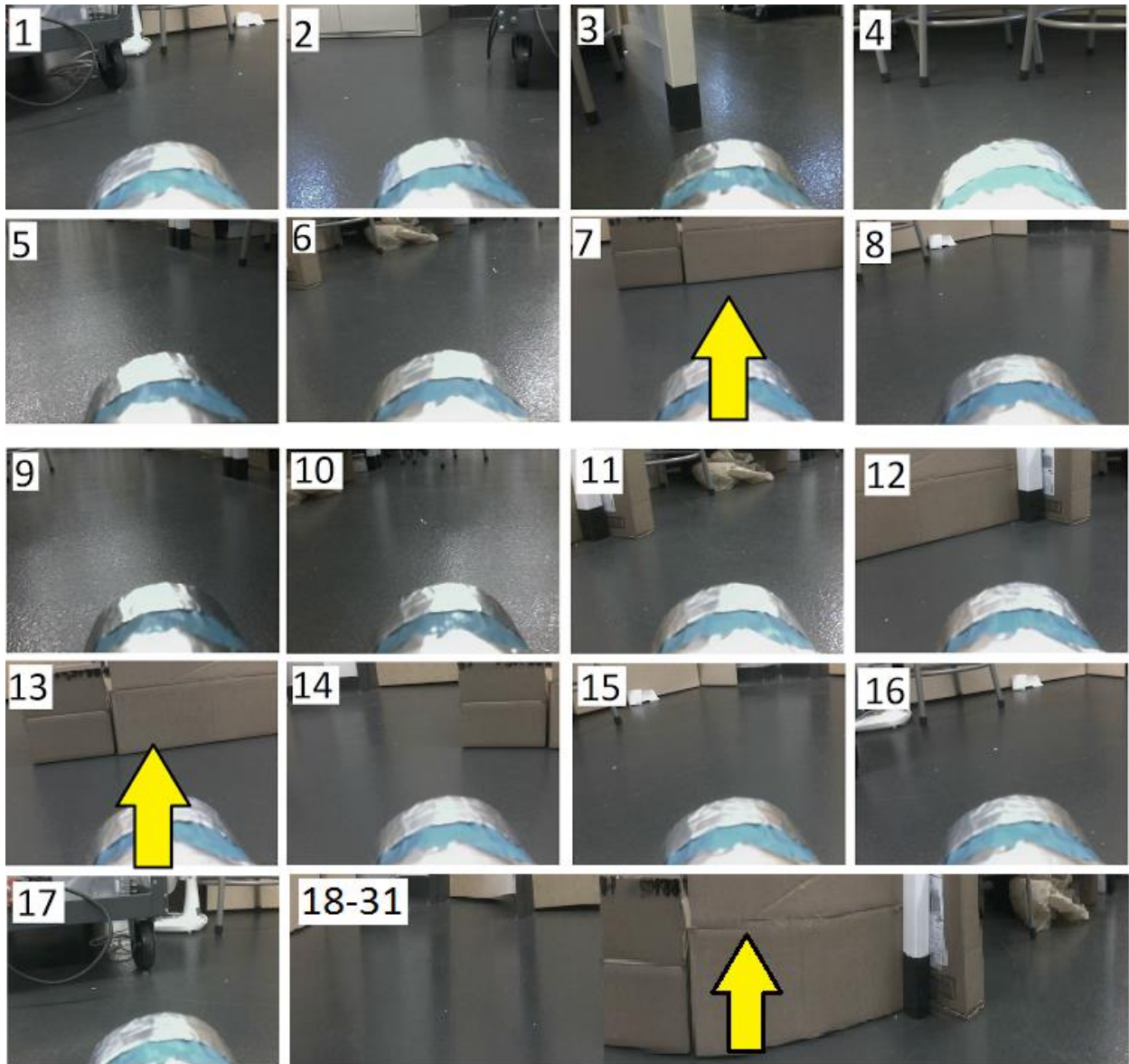


Figure 68: Video sequence of source seek mode with a hidden mixed gamma source

The arrow on step 7 indicates that the highest recorded gamma ray signal in the first phase occurred in this direction. In the second phase between steps 9 and 17 the highest recorded gamma ray signal occurred at step 13. The final fine sweep scan performed in steps 18-31 is represented by a panorama encompassing all of the directions measured during the sweep. Here

the arrow indicates the direction of highest recorded detector signal which corresponds to the location of the source.

After completing the sequence, the robot turned the camera to center the gamma ray source in the camera's field of view. The result is shown in the picture on the left in Figure 69. This indicates that the source was determined to be near the edge of the box in the corner of the room. The picture on the right in Figure 69 shows the box with the flap turned down to reveal the source which is within the camera's view.



Figure 69: Hidden source located by source seek mode

3.6 Discussion of Uncertainty and Measurement Error

3.6.1 Uncertainty in Sweep Scan Mode with Count Rate Measurements

The directional profile data from Figure 36 (from Section 3.1.1) was compiled into a single graph to estimate the error involved in estimating the source direction using the peak gamma ray measurements in the sweep scan mode with count rate measurements. In order to analyze the error involved in individual count rate measurements, the directional profiles were all shifted so that the source position would be equivalent to the case when the source was placed at 90° . So the 0° source position data was shifted to the right by 90° , the 30° source data was shifted by 60° , and the 60° source data was shifted by 30° . The compiled graph is shown in Figure 70. The average count rate measurement in each shifted direction was calculated and the average measurements are plotted as a directional profile represented in black on Figure 70.

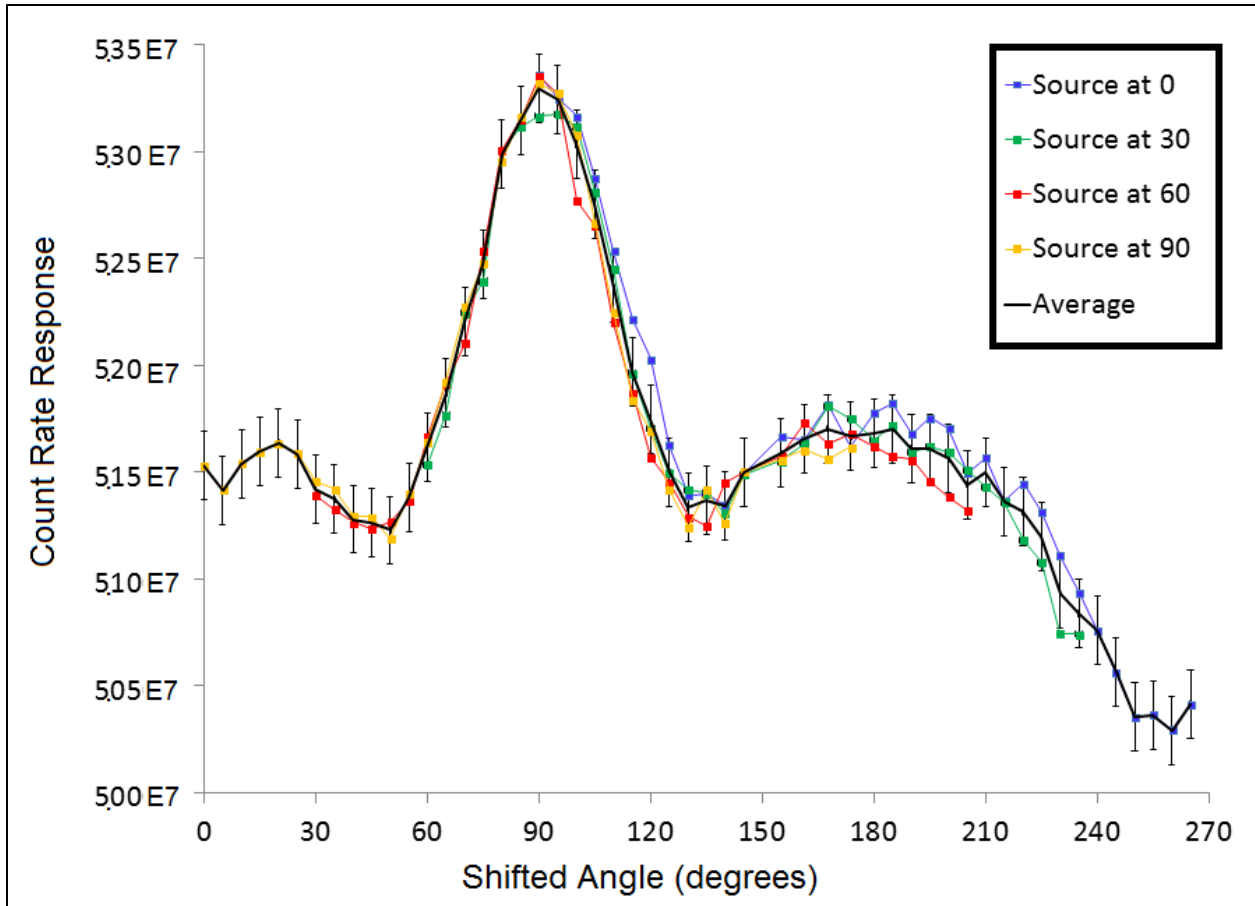


Figure 70: Shifted gamma ray directional profiles. The data from Section 3.1.1 was shifted to normalize the source position and compiled into a single figure.

The peak shows a consistent shape for all four source sweep scans, so it is apparent that the source direction determined at 0° was reasonable in this case, even with no measurements beyond the 0° direction. A statistical standard deviation of the count rate measurements were calculated and added to the graph as error bars (vertical lines). The estimated error in the directional measurement (resulting from imperfections in the robot's motor and detector alignment) were also added to the graph as horizontal error bars. The combined average data shows that the average peak is located at 90° (the true source direction after shifting). Using the error bars as boundaries, maximum and minimum expected peak angles were estimated from the data. This provides an estimate on the error produced when measuring the source direction using

the maximum count rate measurement in the gamma ray directional profile. The maximum estimated peak (source direction) is located at 101° and the minimum estimated peak is at 84° , which are both within 11° of the true source direction. Thus this method can identify the source direction within $\pm 11^\circ$. The autonomous source seek mode also identifies the source direction using the maximum count rate measurements in a gamma ray directional profile and thus should have the same amount of error.

Another more accurate method could be used to measure the source direction from the directional profile data from Figure 36. The gamma ray profile data follows an approximately Gaussian peak around the source direction. Fitting a Gaussian function to the data and determining the peak centre would provide a better estimate of the source direction that takes all measurements into account, rather than just using the single highest measurement direction. A Gaussian function was fitted to three of the four directional profiles from Figure 36 (the 0° source direction was not used since only half of the peak was measured) and the peak direction was determined from each. The best fit Gaussian function for the data was calculated by the Origin Pro 8 software package using the software's least squares Gaussian fit function. The Origin Pro software also calculated an estimated standard error on the peak position. The result is shown in Figure 71 where the measurement data is plotted along with the best fit Gaussian curve. The peak position and estimated peak position error is indicated on the figure. In each case the peak is very near the actual source direction (within 2°) and the error in the estimates is very small (about 1°). This suggests that a Gaussian method could be used on the robot to identify the source direction within $\pm 3^\circ$.

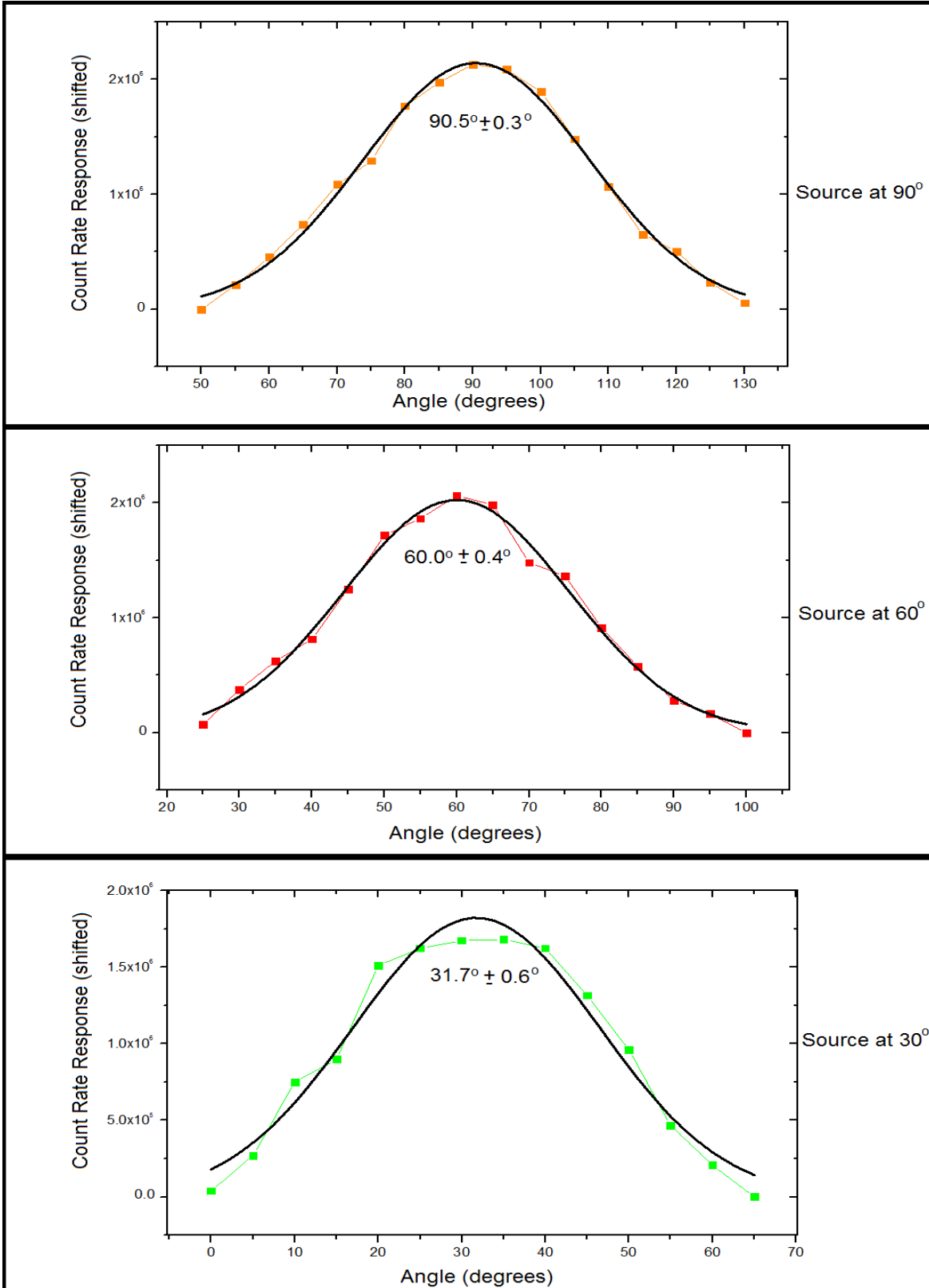


Figure 71: Gamma ray directional profile peaks with best fit Gaussian functions.

3.6.2 Uncertainty in Sweep Scan Mode with Energy Spectra

2D count frequency histograms were used to measure source energy and direction from the sweep scan mode data with energy spectra. The energy peaks from the histogram data clearly indicated the source energy. However, the directional data was subject to much more noise than the energy spectra. Spectra produce much less counts in a single energy channel than total count rate measurements, so the counting statistics are less robust when using single energies from a spectrum. For this reason, a 1D Gaussian filter was used to smooth the data along the x-axis (direction measurements) of the 2D frequency histograms to obtain a more accurate measurement of the peak. The raw data of the 662 keV channel (from ^{137}Cs) was extracted from Figure 49 (experiment from Sections 2.8.3 and 3.2) and is shown in Figure 72. The smoothed curve obtained with the Gaussian filter is also plotted in the figure.

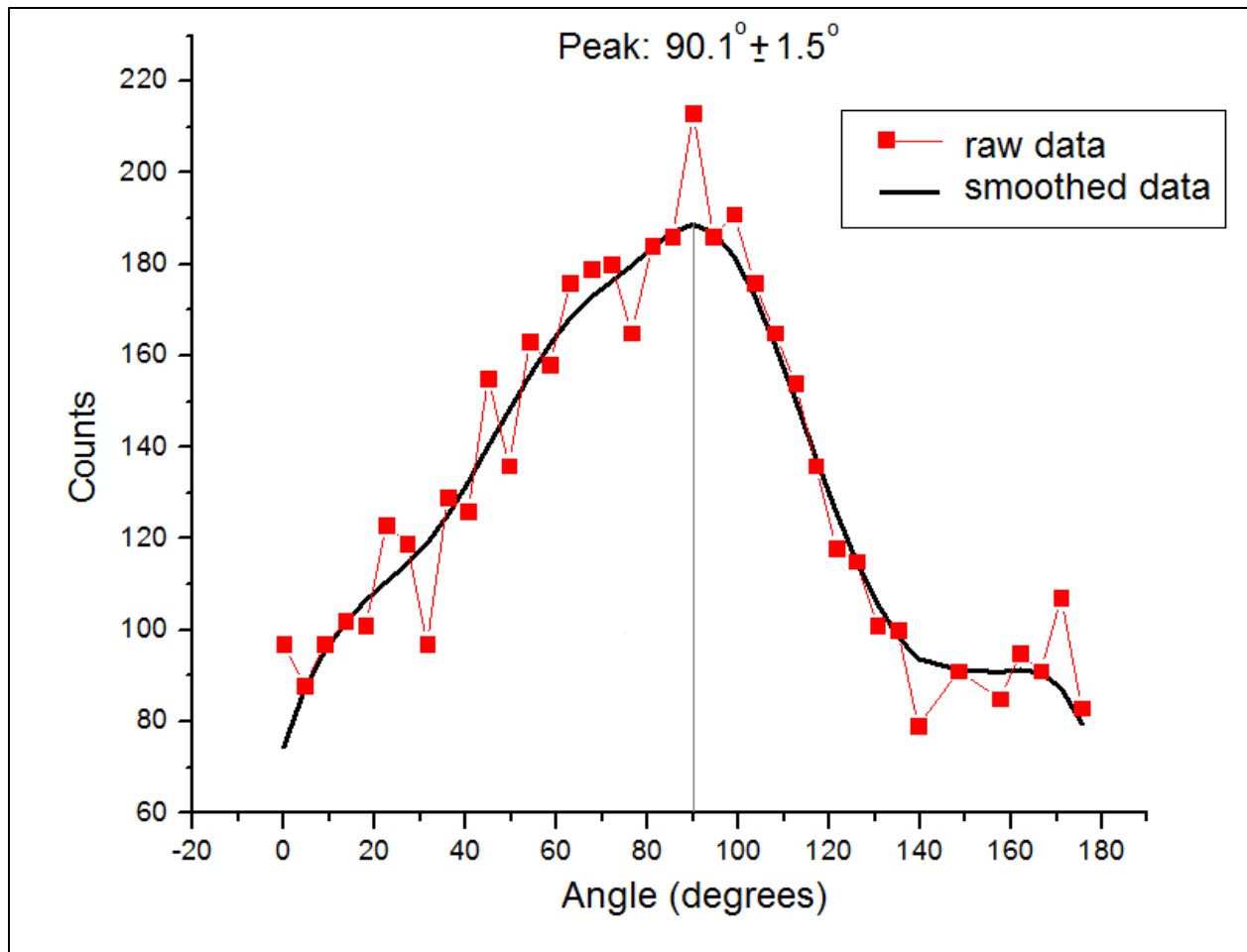


Figure 72: ^{137}Cs gamma ray directional profile raw data and smoothed data.

It is apparent that this smoothed curve represents the peaked shape of the data. The smoothed data was analysed with the Origin Pro 8 software package, which has a peak finding algorithm. The software uses a Gaussian best fit algorithm to estimate peak locations and produce estimated peak errors. The software determined the peak to be in the 90.1° direction and gave an estimated peak direction standard error of $\pm 1.5^\circ$. The smoothed gamma ray directional profile data for the two ^{60}Co energies was also added to the Origin Pro software and the peak finding function was used. The peak of the 1.17 MeV gamma ray directional profile was found to be at 48.4° with a standard error of $\pm 1.8^\circ$. The peak of the 1.33 MeV gamma ray directional profile was found to

be at 47.9° with a standard error of $\pm 2.1^\circ$. This error is comparable to the error determined from the sweep scan data with count rate measurements when best fit Gaussian functions were used.

The peak finding function from Origin Pro was also performed for the smoothed 356 keV gamma ray directional profile data from Figure 55 (experiment from Sections 2.8.4 and 3.3.1).

The peak was determined to be 75.2° with an estimated standard error of $\pm 1.6^\circ$. The peak finding function was also used for the smoothed 1.17 MeV and 1.33 MeV gamma ray directional profile data from Figure 59 (experiment from Sections 2.8.4 and 3.3.2). The peaks were determined to be 82.6° with a standard error of $\pm 1.5^\circ$ and 79.6° with a standard error of $\pm 1.0^\circ$ respectively.

3.6.3 Uncertainty in Point Source Triangulation

The equation for standard error (uncertainty) produced when using the tan function to find the slope of a line from an angle is given by:

$$\Delta m = \Delta \theta (\sec \theta)^2 \quad (21)$$

Where m is the slope of the line determined by $\tan(\theta)$, Δm is the uncertainty in the slope of the line, θ is the angle, and $\Delta \theta$ is the uncertainty in the angle. Equation (21) was used to estimate the uncertainty of the slopes calculated in the point source triangulation experiment (from Sections 2.8.5 and 3.4) based on the measured source angles, θ_s . The uncertainty in the source angles was estimated to be approximately $\pm 4.5^\circ$. After the uncertainty of the slopes was determined, error propagation was used to calculate the error of the coordinate system y-intercepts given by equation (13).

The uncertainty for the y-intercepts is given by:

$$\Delta b = \Delta y_{robot} + \left(\frac{\Delta m}{|m|} + \frac{\Delta x_{robot}}{x_{robot}} \right) \cdot |mx_{robot}| \quad (22)$$

Where b is the y-intercept, Δb is the y-intercept uncertainty, x_{robot} and y_{robot} are the robot's position, Δx_{robot} and Δy_{robot} are the uncertainty in the robot's position (± 0.5 cm for both x and y). Absolute values were used to produce the magnitude of the y-intercept uncertainty. Equations (21) and (22) were used to determine the errors for the slopes and y-intercepts presented in matrix from equation (20). The uncertainties were added into the matrix shown in equation (23).

$$\begin{bmatrix} -1.00 \pm 0.1571 & 1 \\ -3.07 \pm 0.8825 & 1 \\ 6.31 \pm 3.2094 & 1 \\ 1.17 \pm 0.1862 & 1 \end{bmatrix} \begin{bmatrix} x \\ y \end{bmatrix} = \begin{bmatrix} 0 \pm 0.500 \\ -92.33 \pm 26.7 \\ 378.82 \pm 192.2 \\ 105.37 \pm 17.8 \end{bmatrix} \quad (23)$$

The estimated source position using the sum of least squares solution from equation (19) was (50.4 cm, 54.9 cm). A multitude of possible estimated source positions were calculated with combinations of the minimum and maximum estimated slopes and y-intercepts taken from the uncertainties in the matrix from equation (23). This produced 512 expected source positions which represented different amounts of error based on the calculated uncertainties. The average estimated source position from these 512 possible positions was (48.8 cm, 50.9 cm) and the standard deviation of the estimated x and y positions were 8.8 cm and 17.9 cm respectively. This provided an estimate on the uncertainty of our estimated source position. Thus, the source position was estimated to be $(50.5 \pm 8.8 \text{ cm}, 54.9 \pm 17.9 \text{ cm})$. The uncertainty of the estimated source position represents a rectangular region that is slightly larger, but still comparable to the 90% confidence interval region determined by the Monte Carlo Method presented in Figure 64.

Conclusion

We have developed a method for measuring the direction of gamma rays using a lead sheathed, high resolution scintillator detector mounted on a remotely controlled mobile platform. A prototype has been constructed and tested in several experiments with different gamma radiation sources in different operating modes.

Performing a 180° sweep scan with the prototype produced a gamma ray directional profile where a point source of radiation was indicated by a measurable peak of the count rate registered by the detection system. Overlaying a graph of detector response versus angle on top of a visual panorama clearly indicated the direction of a point source.

A data acquisition system consisting of multichannel analyser has been added to the system for measuring the radiation spectra of single as well as multiple sources at each position. The spectral analysis allows for the identification of the radioactive isotopes present in the scanned area as well as their directions.

The prototype constructed has been successful in identifying point sources of gamma rays using the three modes presented in this thesis and conveying the information visually in a way that is easily interpreted by a human operator.

The prototype has also been successful in triangulating the position of a point source using known measurement positions and gamma ray direction measurements. The source seek mode developed has been consistently and successfully able to locate nearby gamma ray point sources.

The most severe limitation of the work done in this thesis is the constriction of all measurements to a plane parallel to the detector. Sources significantly above or below the height of the detector cannot be properly located using these methods. The 180° rotation limit of the detector on the prototype also restricted the gamma ray directional profiles and visual data overlays to the forward direction of the robot. The second most limiting aspect of the prototype was an inability to construct gamma ray directional profiles and visual panorama overlays in real time due to the limited capabilities of the control system.

Future Work

Future work for this thesis would involve the addition of a more robust control system using a fully functional computer rather than a simple microcontroller. A wide angle lens or array of lenses could be used for capturing visual panoramas in a single image. 360° panoramas could allow for a survey of the entire local area rather than limiting a survey to the forward direction of the robot. Software could be made that would place gamma ray directional profiles on top of visual panoramas as soon as a sweep measurements are complete. 2D spectral and directional count frequency histograms could be constructed in real time and peaks could be immediately identified using an algorithm we are currently developing. A database library of common gamma ray energies from known gamma ray emitting isotopes is under development and will be added to the software as well. This would allow for instantaneous identification of the direction and isotope of multiple gamma ray sources around the robot.

In addition our future focus is to develop a 4π directional system in order to assemble a more complete directional gamma ray profile that could identify the horizontal angle and azimuthal angle of incoming gamma rays.

References

- [1] B. Milbrath, J. E. Fast, W. K. Hensley, and J. E. Schweppe, "Comparison of LaBr₃:Ce and NaI(Tl) Scintillators for Radio-Isotope Identification Devices (Revision 0)," Springfield, VA, 2006.
- [2] R. Redus, M. Squillante, and J. Gordon, "A combined video and gamma ray imaging system for robots in nuclear environments," *Nucl. Instruments Methods Phys. Res.*, vol. 353, pp. 324–327, 1994.
- [3] O. P. Ivanov, "New approach to the development of a portable gamma-ray camera with the maximum angle-of-view," *At. Energy*, vol. 108, no. 1, pp. 64–69, Apr. 2010.
- [4] J. Watts, K. Hosier, and S. Williams, "COMPUTER-CONTROLLED GAMMA CAMERA Jeff Watts," *IEEE Trans. Nucl. Sci.*, vol. NS-27, no. 1, pp. 533–536, 1980.
- [5] T. A. Devol, D. K. Wehe, and G. F. Knoll, "Gamma-ray spectral imaging using a single-shutter radiation camera," *Nucl. Instruments Methods Phys. Res.*, vol. 299, pp. 495–500, 1990.
- [6] S. Ebstein, "Transportable megapixel gamma camera," in *SPIE*, 2001, vol. 4507, no. 2001, pp. 119–124.
- [7] K. Qian, A. Song, J. Bao, and H. Zhang, "Small Teleoperated Robot for Nuclear Radiation and Chemical Leak Detection," *Int. J. Adv. Robot. Syst.*, vol. 9, no. 70, pp. 1–9, 2012.
- [8] J. Baczyński and M. Baczyński, "Simple Teleoperator System for Gamma Radiation Decontamination," *Proc. ISIE*, pp. 1517–1520, 2005.
- [9] R. Gould, J. E. Tarpinian, and E. S. Kenney, "An automated system for gamma radiation field mapping," *Nucl. Instruments Methods Phys. Res.*, vol. 299, pp. 538–543, 1990.
- [10] T. Kobayashi, M. Nakahara, K. Morisato, T. Takashina, and H. Kanematsu, "Remote Sensing of Radiation Dose Rate by Customizing an Autonomous Robot," *J. Phys. Conf. Ser.*, vol. 352, p. 012033, Mar. 2012.
- [11] G. Chaudhary, "Detecting a Target Location Using a Mobile Robot With Range Only Measurement," in *Industrial Electronics and Applications (ICIEA)*, 2011, pp. 28–33.
- [12] F. Von Frankenberg, R. Mcdougall, S. Nokleby, and E. Waller, "A Mobile Robotic Platform for Generating Radiation Maps," in *Intelligent Robotics and Applications*, 2012, pp. 407–416.

- [13] R.A. Cortez and H.G. Tanner, "Radiation Mapping Using Multiple Robots," *Trans. Am. Nucl. Soc.*, vol. 99, pp. 157–159, 2008.
- [14] J. Han, Y. Xu, L. Di, and Y. Chen, "Low-cost Multi-UAV Technologies for Contour Mapping of Nuclear Radiation Field," *J. Intell. Robot. Syst.*, vol. 70, no. 1–4, pp. 401–410, Aug. 2012.
- [15] K. N. Krishnanand, P. Amruth, M. H. Guruprasad, S. V Bidargaddi, and D. Ghose, "Glowworm-inspired robot swarm for simultaneous taxis towards multiple radiation sources," *Proc. 2006 IEEE Int. Conf. Robot. Autom. 2006 ICRA 2006*, no. May, pp. 958–963, 2006.
- [16] G. Tuna, K. Gulez, T. V. Mumcu, and V. C. Gungor, "Mobile Robot Aided Self-Deploying Wireless Sensor Networks for Radiation Leak Detection," in *International Conference on New Technologies, Mobility and Security*, 2012, pp. 1–5.
- [17] M. Fred, *Medical Effects of Ionizing Radiation*. Philadelphia, PA: Saunders/Elsevier, 2008.
- [18] G. E. Knoll and J. Wiley, *Radiation Detectibn and Measurement Third Edition*, Third. Danvers, MA: John Wiley & Sons, Inc., 2002.
- [19] A. D. and T. Ferbel, *Introduciton to Nuclear and Particle Physics*, Second. River Edge, NJ: World Scientific, 2003.
- [20] C. Leroy and P.-G. Rancoita, *Principles of Radiation Interaction in Matter and Detection*, Third. New Jersey: World Scientific, 2012, pp. 168–237.
- [21] N. Cook, *Models of the Atomic Nucleus*. Berlin, NY: Springer, 2006.
- [22] I. Transactions and O. N. Nuclear, "Gamma Ray Spectroscopy With a LaBr scintillator," *IEEE Trans. Nucl. Sci.*, vol. 51, no. 3, pp. 1289–1296, 2004.
- [23] R. T. Klamm, Q. Lou, and C. L. Fink, "Angular Response Functions for Sodium Iodide Detectors," *2006 IEEE Nucl. Sci. Symp. Conf. Rec.*, no. 1, pp. 1224–1228, 2006.
- [24] G. Strang, *Introduction to Linear Algebra*. Wellesley, MA: Wellesle-Cambridge Press, 2009, pp. 218–244.
- [25] A. Oberstedt, R. Billnert, and S. Oberstedt, "Neutron measurements with lanthanum–bromide scintillation detectors—A first approach," *Nucl. Instruments Methods Phys. Res. Sect. A Accel. Spectrometers, Detect. Assoc. Equip.*, vol. 708, pp. 7–14, Apr. 2013.
- [26] Lynxmotion, "A4WD1 Tutorial for Autonomous Behavior v1.0," 2011. [Online]. Available: www.lynxmotion.com.

- [27] Spectrum Techniques, "SPECTECH Disc & Laminate Sources," [Online]. Available: http://www.spectrumtechniques.com/disc&laminated_sources.htm.
- [28] P. G. Spectrometry and E. Gordon, *Practical Gamma Ray Spectrometry*, Second. Hoboken, NJ: John Wiley & Sons, Inc., 2008, pp. 322–364.
- [29] J. Muralikrishnan, Balasubramanian and Raja, "Gaussian Filter 5.1," in *Computational Surface and Roundness Metrology*, 2009, pp. 33–38.
- [30] ORTEC, "Lanthanum(III) bromide," 15-Dec-2006. [Online]. Available: www.ortec-online.com. [Accessed: 01-Mar-2014].

Appendix

Appendix A: Properties of LaBr₃

Table 2: Comparison of LaBr₃, NaI and HPGe [30]

Comparison of Critical Parameter for Lanthanum Bromide				
Detector Type	Resolution @662 keV (%)	Density (g/cc)	Photoelectron Yield Relative to NaI	Primary Decay Time (μsec)
LaBr ₃ (Ce)	2.8–4.0	5.29	130	0.026
NaI(Tl)	7	3.7	100	0.230
HPGe	0.2 (1.3 keV)	5.35	N/A	N/A

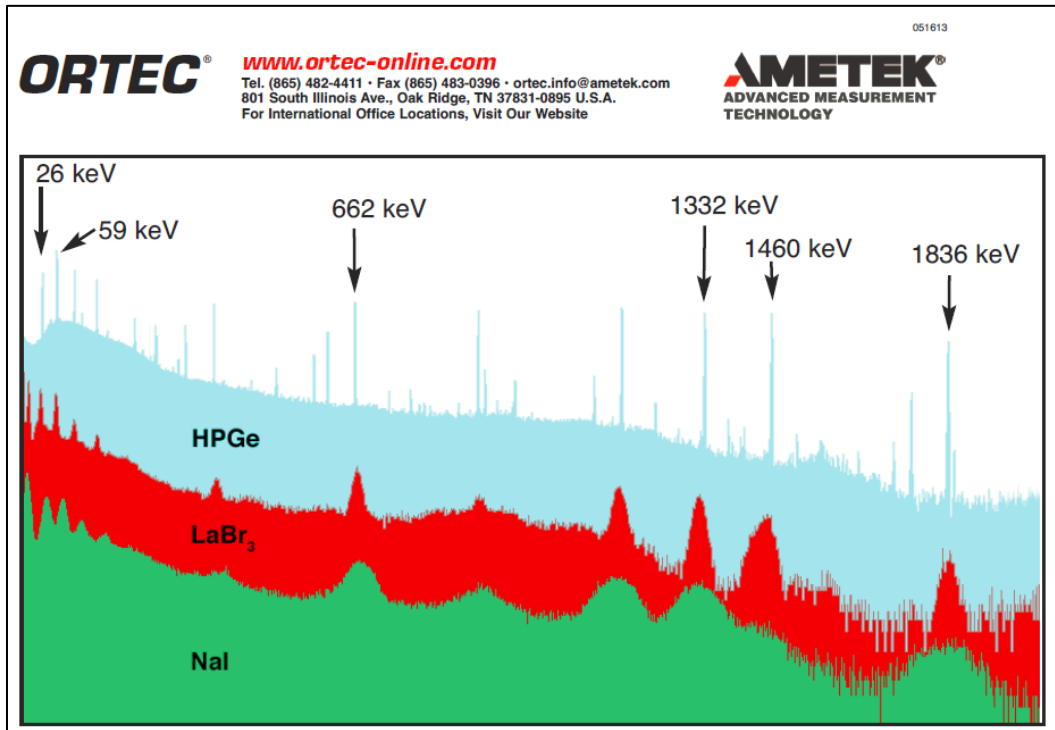


Figure A1: Comparison Spectra for NaI, LaBr₃ and HPGE [30]

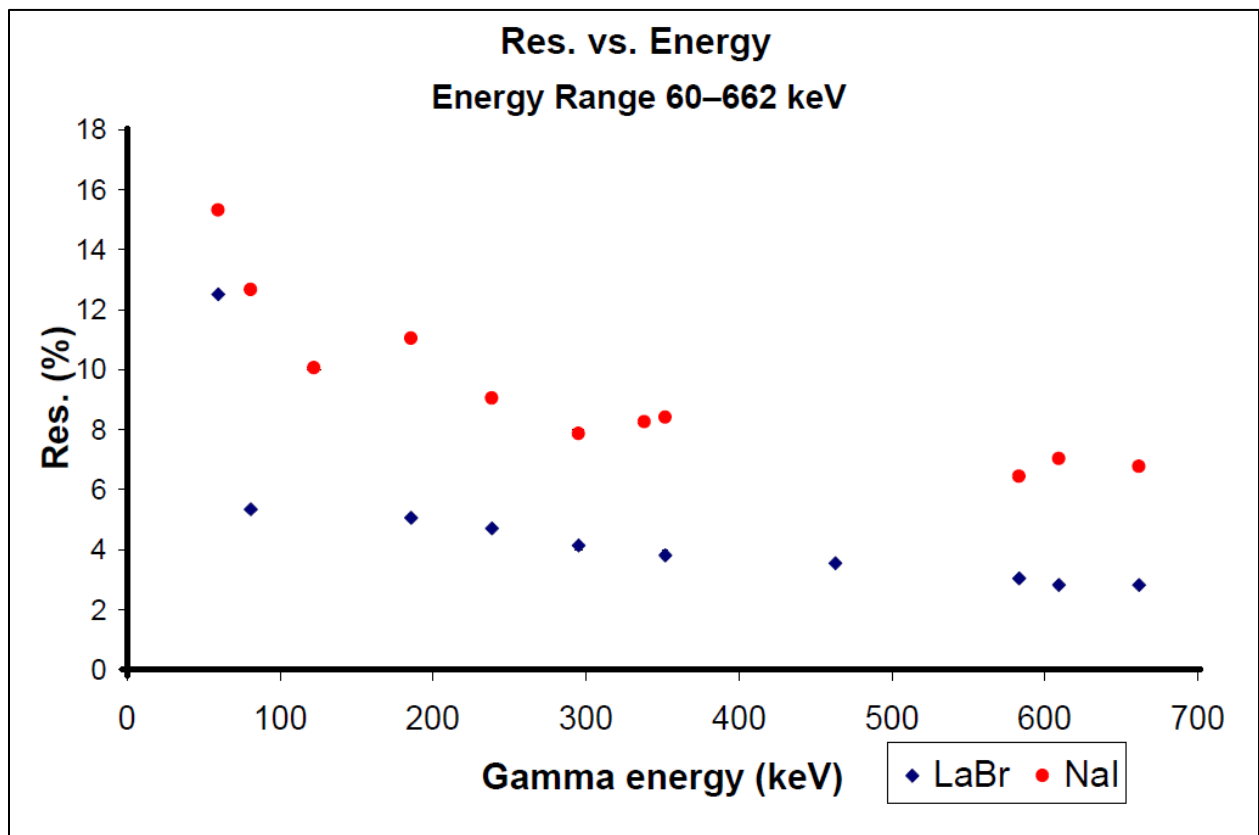


Figure A2: Resolution comparison for NaI and LaBr₃ [1]

Appendix B: Background Radiation

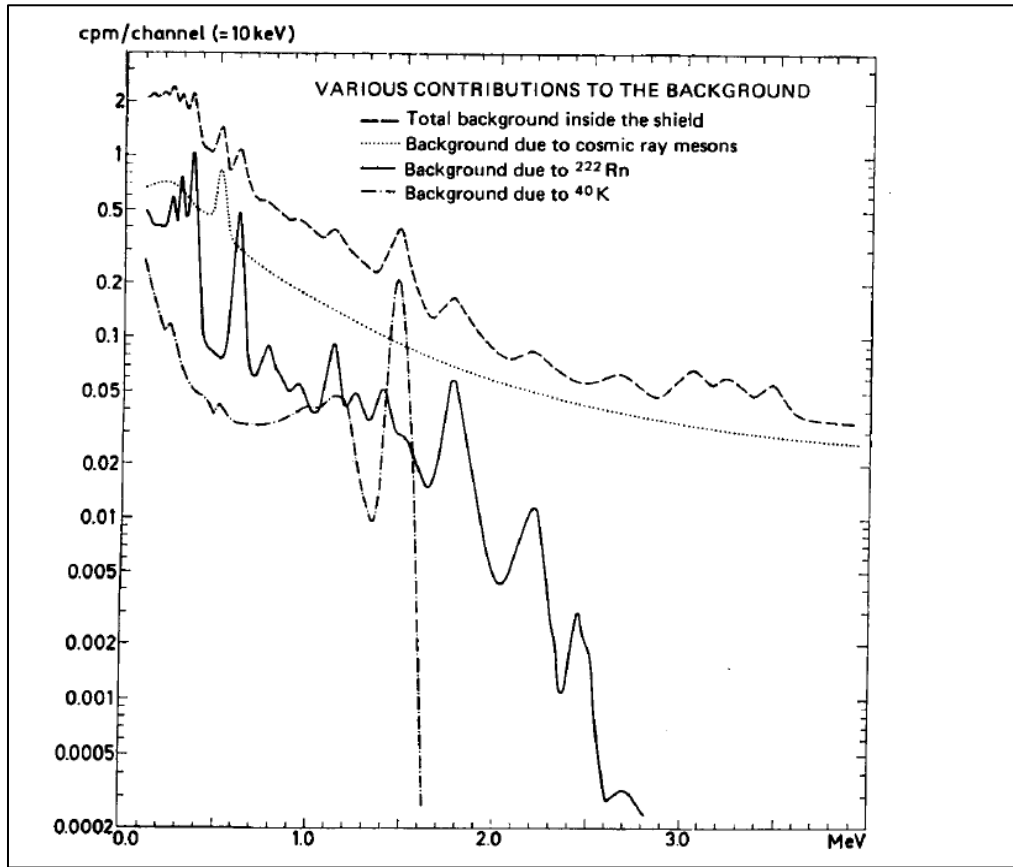


Figure A3: Background Radiation Spectrum for NaI in massive lead shield [18]

Appendix C: Supplementary Data

Table 3: Radiation Source Activities

Source	Activity of Each Button Source at Date of Experiment
RSS-5 kit sources	
RSS-5 ^{137}Cs	4.095 μCi (151530 Bq)
RSS-5 ^{60}Co	0.320 μCi (11834 Bq)
RSS-5 ^{210}Po	0.106 μCi (5947 Bq)
RSS-5 ^{204}Tl	0.204 μCi (755 Bq)
RSS-5 ^{90}Sr	0.081 μCi (3003 Bq)
RSS-8 kit sources	
RSS-8 ^{137}Cs	0.866 μCi (32042 Bq)
RSS-8 ^{60}Co	0.440 μCi (16262 Bq)
RSS-8 ^{57}Co	0.003 μCi (107 Bq)
RSS-8 ^{135}Ba	0.667 μCi (24681 Bq)
RSS-8 ^{54}Mn	0.006 μCi (233 Bq)
RSS-8 ^{22}Na	0.189 μCi (6992 Bq)
RSS-8 ^{109}Ca	0.031 μCi (1128 Bq)
RSS-8 ^{137}Cs and ^{65}Zn (labeled as “unknown”)	0.435 μCi (16029 Bq)

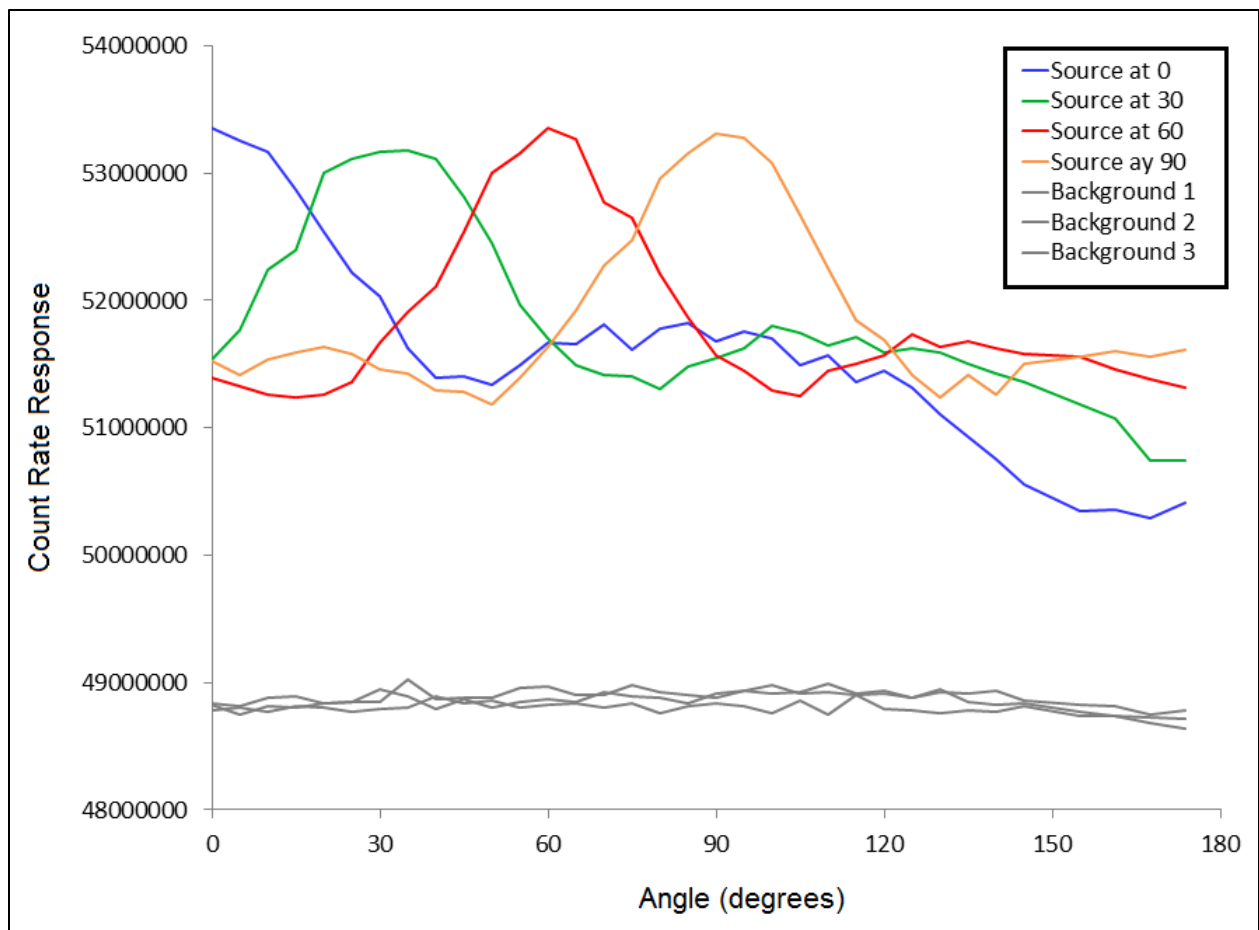


Figure A4: Gamma ray directional profile results with 1 mCi ^{137}Cs at 0° , 30° , 60° , and 90° and three background profiles measured with no sources present

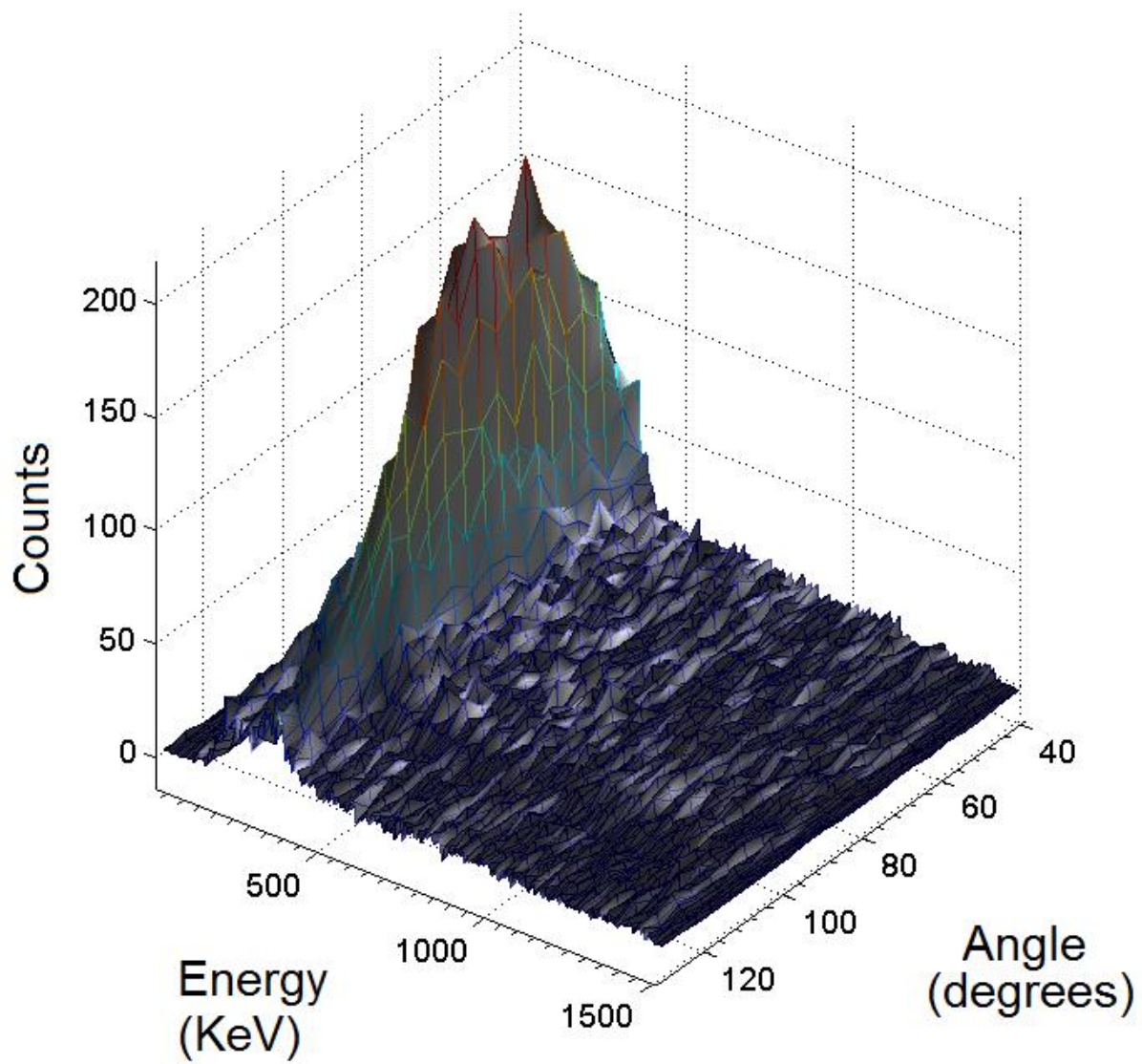


Figure A5: Raw frequency data for ^{133}Ba rapid scan gamma ray profile

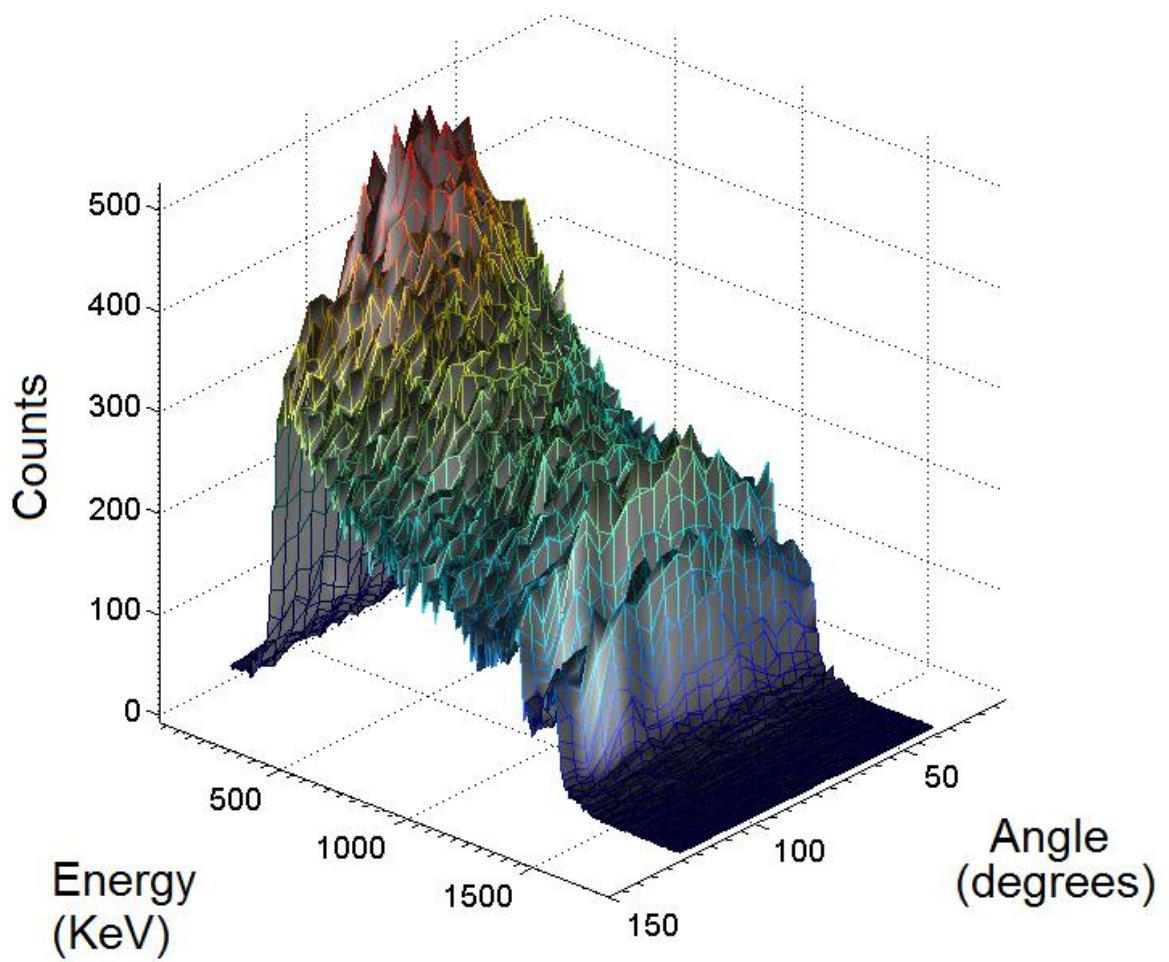


Figure A6: Raw frequency data ^{60}Co rapid scan gamma ray profile